Polarization Imaging for Pathological Diagnosis

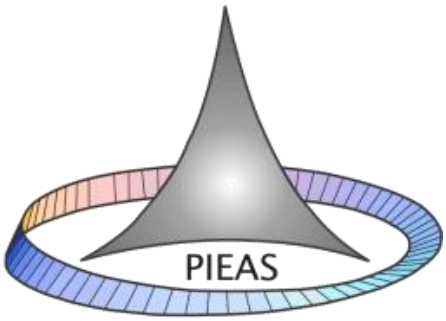

Iftikhar Ahmad

2016

Department of Physics and Applied Mathematics
Pakistan Institute of Engineering and Applied Sciences
Nilore, Islamabad, Pakistan
2016

This page intentionally left blank.

Thesis Submission Approval

This is to certify that the work contained in this thesis entitled **Polarization Imaging for Pathological Diagnosis**, was carried out by **Iftikhar Ahmad**, and in my opinion, it is fully adequate, in scope and quality, for the degree of **Ph.D.** Furthermore, it is hereby approved for submission for review and thesis defense.

Supervisor: _____
Dr Masroor Ikram
Date: 25 July, 2016
Place: PIEAS, Islamabad.

Head, Department of Physics and Applied Mathematics: _____
Name: **Dr. Shahid Qamar**
Date: 25 July, 2016
Place: PIEAS, Islamabad.

Polarization Imaging for Pathological Diagnosis

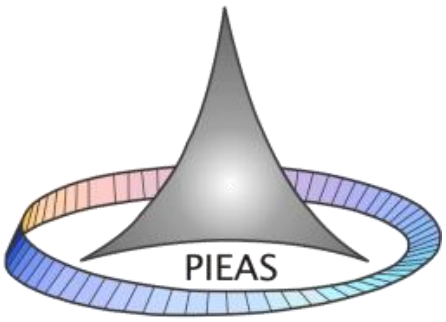

Iftikhar Ahmad

Submitted in partial fulfillment of the requirements
for the degree of Ph.D.
2016

Department of Physics and Applied Mathematics
Pakistan Institute of Engineering and Applied Sciences
Nilore, Islamabad, Pakistan

Dedications

My Parents,

Wife

and sweet kid

Muhammad Dawood

Declaration of Originality

I hereby declare that the work contained in this thesis and the intellectual content of this thesis are the product of my own work. This thesis has not been previously published in any form nor does it contain any verbatim of the published resources which could be treated as infringement of the international copyright law. I also declare that I do understand the terms ‘copyright’ and ‘plagiarism,’ and that in case of any copyright violation or plagiarism found in this work, I will be held fully responsible of the consequences of any such violation.

_____

(Iftikhar Ahmad)
July 25, 2016
PIEAS, Islamabad.

Copyrights Statement

The entire contents of this thesis entitled **Polarization Imaging for Pathological Diagnosis** by **Iftikhar Ahmad** are an intellectual property of Pakistan Institute of Engineering & Applied Sciences (PIEAS). No portion of the thesis should be reproduced without obtaining explicit permission from PIEAS.

Table of Contents

List of Figures

List of Tables

Abstract

We present the application of optical polarimetry to characterize healthy and pathological tissues including cancerous human skin and radiofrequency ablated (RFA) porcine myocardial tissues.

Optical polarimetry of thin (4 μm) *ex vivo* tissue samples from human skin revealed that depolarization and retardance were significantly higher ($p<0.0001$) for normal as compared to basal cell carcinoma (BCC) group. Histopathology indicated that these differences partially arise from BCC-related characteristic changes in tissue morphology. Wilks lambda statistics was used to optimize the number of polarimetric parameters for subsequent computer aided classification. Based on the observed differences in polarization metrics for the two groups, partial least square classification categorized the samples with high degree of sensitivity, specificity and accuracy.

The second pathology assessed through optical polarimetry was RFA lesion that typically consists of a core (coagulative necrosis) surrounded by a rim of mixed viable and non-viable cells. Polarization signatures of ten *ex vivo* samples from untreated (n=5) and RF ablated porcine hearts (n=5) were explored in backscattered geometry through optical polarimetry, enabling the measurement and quantification of the changes in depolarization and linear retardance associated with structural damage due to myocardial RF ablation. Significantly decreased depolarization ($p < 0.01$) and linear retardance ($p < 0.05$) magnitudes were observed in the core of the RFA lesion, with partial recovery in the rim region. Linear retardance orientation results were also quantified but were more difficult to interpret. Histology was used to investigate the underlying morphological changes caused by RFA and to help interpret the polarimetry signals.

The observed differences in total depolarization image for the aforementioned three regions (RFA core, rim and healthy) of RFA tissue were exploited for multi-region segmentation of image using local fuzzy thresholding algorithm. The ground truth segmentation was obtained from the expert manual demarcation of RFA core and rim regions on the histology image. The quantitative comparison of computer-aided segmentation was performed with the evaluation metrics such as dice similarity coefficient (DSC ~0.76 and 0.82), sensitivity (S_n ~0.98 and 0.96), specificity (S_p ~ 0.83 and 0.64) and accuracy (Acc ~ 0.86 and 0.80) for RFA core and rim region, respectively indicating good agreement between the automated and ground truth segmentations.

List of Publications

1. **I Ahmad**, A Gribble, M Ikram, M Pop, A Vitkin, “Polarimetric assessment of healthy and radiofrequency ablated porcine myocardial tissue” J Biophotonics, 1-10, 2015.
2. **I Ahmad**, A. Rehman, JA Khan, A Khurshid, H Nisar, SSZ Zaidi, M Ikram, “Effects of varying local temperature on the optical properties of cells in-vitro," J Photodiagnosis and Photodynamic therapy, 12, 459-465, 2015.
3. **I Ahmad,** M Ahmad, K Khan, S Ashraf, S Ahmad, M Ikram;"Ex vivo characterization of normal and adenocarcinoma colon samples by Mueller matrix polarimetry," J. Biomedical Optics, 20(5), 056012, 2015.
4. **I Ahmad**, Manzoor Ahmad, Karim Khan, Masroor Ikram, “Polarimetry Based Partial Least Square Classification of Ex Vivo Healthy and Basal Cell Carcinoma Human Skin Tissues” J Photodiagnosis and Photodynamic therapy, 14, 134-141, 2016.
5. A. Rehman, **I Ahmad**, K. Rehman, S. Anwar, S. Firdous, and M. Nawaz, “Optical properties measurement of highly diffusive tissue phantoms for biomedical applications,” Laser Physics, 25(2), 025605, 2015.
6. **I Ahmad**, A Gribble, I Murtza, M Ikram, M Pop, A Vitkin, “Polarization Image Segmentation of Radiofrequency Ablated Porcine Myocardial Tissue” submitted to PLoS One.

Acknowledgements

First and foremost, I am heartedly thankful to Almighty Allah (ﷻ) for His countless blessings including the opportunity of this research work and its completion. I offer my sincere gratitude to the Holy Prophet (ﷺ), the sole pride of mankind and icon of mercy.

I would like to pay heartfelt gratitude to my supervisor Dr. Masroor Ikram. Unequivocally, his dedication and devotion to work has been a source of immense inspiration for me. I must appreciate his guidance, cooperation and generosity for study and research related issues and beyond.

I would like to thank Dr. I. Alex Vitkin (University of Toronto, Canada) for his kind supervision and guidance in manuscript preparation. Most importantly, I am cordially thankful to my parents who always work hard and scarified to flourish my career. I also appreciate the exceptionally supporting role of my wife and siblings during my studies.

I would like to thank Prof. Anwar Ali for providing biological samples and expert histology opinion. I am also very grateful to Mr. Junaid Ahmed Khan, Mr. Rafi Muhammad, Dr. Shakeel Ahmad and Dr. Manzoor Ahmad for their guidance, advices, and invaluable suggestions and comments. I am also thankful to my friends, particularly, Mr. Karim Khan, Dr. Attaullah Shah, Dr. Zia-ur-Rahman, Mr. Banat Gul, Mr. Safdar Ali, Mr. Zaheer Uddin, Miss Sumaira Ashraf and Mr. Adam Gribble for their cooperation during my research work.

Finally, financial support from IT & EF, PIEAS throughout the PhD and Higher Education Commission of Pakistan for IRSIP program is highly acknowledged.

1 Introduction

1.1 Introduction

Light is a type of electromagnetic waves- comprised of oscillations of electric and magnetic fields. Visible light have inherently identical nature to other electromagnetic waves with the only exception that the human eye can sensitively detect visible waves. Among other important properties, the polarization of electromagnetic waves (and light) stems from its transverse nature. Specifically, polarization is related to the electric field of the electromagnetic waves and can be define as the pattern traced by the electric field vector in space as a function of time. Restricting the oscillations of electric field vector to a single plane result in linearly polarized light; when the tip of electric field vector describes a circle, the light is named as circularly polarized light; when the oscillations of the electric field vector follow an ellipse, it is called elliptically polarized light. It is noteworthy that linear and circular polarization can be considered as special cases of the most general form- the elliptical polarization.

Light polarization needs to be described in such a way that all the important features should be elaborated and reflected. Two types of representation (i.e. graphical and mathematical) for polarized light have been reported. Specifically, Poincare sphere is a graphical visualization method while Jones vector and Stokes vector are mathematical tools for representation of polarized light. Poincare sphere is a comprehensive illustration for any type of polarization of light including linear, circular and elliptical states. Further, it can account for partial and unpolarized light. Jones vector, based on amplitude and phase of the electric field, is a simple and compact mathematical formalism for polarized light description. However, it is unable to properly handle partial and unpolarized light [1]. Stokes vector methodology is equally suitable in dealing with totally, partially and unpolarized polarized light. Moreover, it can be argued that it conveniently attempt in terms of physically measureable quantities (i.e. intensity) rather than a pure mathematical

approach, as the case for Jones vector [2]. In addition, polarization ellipse representation involves both mathematical and graphical descriptions. Specifically, polarization of light is described the equation of ellipse with four parameters including semi-major and semi-minor axes, azimuth and ellipticity. Further, graphical representation of the given polarization state can also be simultaneously provided on the polarization ellipse.

The detection of light after interaction with matter is a radically powerful tool for exploring and understanding the universe around us. Analysis of probing light after interaction with matter can potentially reveal many inherent features and properties of the probed matter. Generally, one can appreciate that such analysis facilitated the study of processes that occur at diminutive scale like atomic level and biological cell as well as at immensely large systems like stars and galaxies. The findings of such investigations have been translated into daily applications that revolutionized society through medicine, entertainment, communications, etc. In particular, the biomedical research arena has progressively witnessed an expanded spectrum of *light* applications towards improved pathological diagnosis and treatment.

Polarization is a remarkable property of light which has been also exploited towards many applications unequivocally. Light polarization have been used to study three dimensional structural characteristics of chemical bonds [3], elucidating various nondestructive evaluation methods [4], exploring the chiral nature of biological molecules [5], quantifying sugar concentrations in industrial solutions and processes [6], determining protein properties [7], establishing advanced concepts like polarization entropy [8], contributing towards sensitive radars for remote sensing in astronomy and meteorology [9], [10], assessment of pathological states of biological tissues [11], etc. The following section has been devoted to a comprehensive review of exploiting light polarization towards applications in biomedical optics.

1.2 Polarized Light Applications in Biomedical Research

Optical polarimetry deals with the measurement of changes in light polarization states after interaction with the given sample, which are subsequently correlated with the structure, composition and micro-architecture of the probed sample. The sample under

polarimetric investigation can be categorized either optically clear (where only absorption of probing beam take place) or turbid (where both absorption and scattering of probing occurs). It is noteworthy that polarimetry is a well-established optical technique for assessment of optically clear samples. However, multiple scattering in the turbid media like biological (such as myocardial) tissues offers many challenges in the measurements of polarization properties. Specifically, the dominant multiple scattering in turbid media cause extensive depolarization of probing light beam and significantly limits the sampling depth. Consequently, optical polarimetry is effectively applicable to only thin tissue samples (~ 3 mm) for measurements in transmission mode. For reflection mode measurements, polarization information is retained by the probed light beam from shallow depths only. Further, the subsequent analyses of polarization properties are essentially made more complicated by the strong multiple scattering caused by turbid media. However, notwithstanding these complications, optical polarimetry still finds large number of useful applications in various fields, particularly in biomedical optics [12].

Light polarization can be effectively used for assessment of pathological state of biological tissues. The important polarization metrics for such assessment include depolarization, linear retardance, diattenuation and optical activity. The interaction of probe beam with the given sample gives rise to depolarization. Specifically, multiple scattering cause randomization (of direction and phase) of the probe beam. The scattering properties of the tissues are influenced by the scatterer (cells, nuclei, mitochondria, etc.) size, shape, density, and spatial variations of refractive index in the tissue [13]. Consequently, depolarization conveys rich morphological and structural information of the probed biological tissues enabling optical polarimetry as a diagnostic tool. Likewise, tissue structural/ anatomic anisotropy in turn gives rise to directional variations of refractive index, which is known as linear retardance (closely related to birefringence). This polarization property is particularly important for characterization of striated tissue such as smooth and cardiac muscles via optical polarimetry. In addition, other parameter of interest in tissue polarimetry is optical activity; the rotation of polarization vector of the light beam resulting from interaction with chiral molecules such as glucose. One particularly interesting biomedical application of optical activity measurement is the

noninvasive quantification of glucose in both clear and turbid media [14]. These few polarization metrics along with others (discussed later) provide a framework for the assessment of pathological state of biological tissues. Indeed, the significant amount of available research work in various fields confirms the emerging role of polarized light in biomedical optics.

Due to the complex nature of strong multiple scattering in biological tissues and subsequent simultaneous polarization effects, the preliminary understanding of polarized light propagation and interaction is gained from theoretical (simulation) and phantom-based studies where the experimental parameters are easily tunable contrary to biological tissues [15], [16]. Various tissue phantoms for optical measurements can be fabricated with significant ease using intralipid and polystyrene microsphere suspensions as scatterer and Indian ink as absorber. Further, such phantoms with controlled polarimetric properties also play essential role in calibration of experimental setups and validation of different techniques of polarization measurements [15].

It is worth mentioning that fabrication of phantoms that mimic specific tissues in terms of bulk optical properties such as scattering coefficient, absorption coefficient, anisotropy coefficient, etc. does not necessarily ensure identical polarimetric behavior, demanding that particular attention must be devoted for preparation of polarimetric phantoms [17]. Indeed, the different mechanisms of depolarization for each individual polarization state and its correlation with the spatial variations of refractive index in the probing medium essentially stage more complications for fabrication of such phantoms [18]–[20]. Furthermore, previous studies targeting this confounding issue have reported considerable differences in the behavior of interaction of different polarization states with biological tissues and corresponding phantoms with identical optical properties. For instance, linear and circular incident polarization states has been demonstrated significantly greater depolarization in thin tissue slabs as compared to phantoms having identical optical properties in transmission geometry, presumably due to the scattering-dependent nature of individual polarization state [21]–[23]. Furthermore, it has been observed that circular polarization states decay faster as compared to linear polarization states in various biological tissues, except blood [22], [24].

Polarization imaging of biological tissues facilitates to study useful and in-depth metrics including measurements of depolarization, linear retardance (birefringence) and optical rotation that can be correlated to the pathological state of the given tissue, as has been recently investigated in a variety of biomedical fields and scenarios. For example, depolarization measurements have allowed differentiation of healthy and cancerous tissue in the colon [13], [25] and cervix [26]. *Ex vivo* healthy and cancerous gastric samples were assessed and classified using differences in linear depolarization and retardance [27]. Shukla et al. showed that depolarization power is sensitive to identify morphological changes in normal and dysplastic states of cervical epithelial tissue [28].

Although depolarization of light in biological tissues has been successfully exploited in many biomedical applications of optical polarimetry, nevertheless depolarization is presumably the major limitation for other equally important applications where it perplexes the situation for the utilization of polarized light. It may be noted that polarization information are almost entirely lost in highly scattered light medium which result in exhaustion of any polarization measurement. The issue has been addressed by developing various methodologies for separating the highly scattered light from the weakly or un-scattered light; an approach known as polarization gating [29], [30]. Polarization gating has been effectively used to differentiate between photons propagating through short and long distances in scattering medium [19]. It has been previously shown that polarization gating enables selecting photons primarily scattered from very short tissue depths, i.e. only a few mean free paths below tissue surface. It may be noted that the few mean free path is a function of scattering coefficient, absorption coefficient and anisotropy factor of the given tissue. Nevertheless, the penetration depth has not been quantified [31]. In addition, polarized light temporal gating has been proposed to quantify ballistic photons in turbid medium. The results indicate that the degree of polarization was preserved only for photons registered within 100 Pico-seconds after input light signal [32]. One clinically important application of polarized light gating has been the selective polarization imaging of superficial skin layers. Suppressing the highly scattered photons that are effectively generated from the deeper skin layers via polarization gating method result in significant image quality enhancement in terms of resolution [33]. To this end, a handheld and portable polarization camera has been

developed and successfully demonstrated in guiding the surgical margins of various skin pathologies such as precancerous, benign and cancerous tissues [30], [34], [35]. Furthermore, polarization gating has been utilized for the depth selectivity in bioengineered connective tissues [36].

In addition to exploiting tissue depolarization for various biomedical applications, linear retardance also carries important information and can be effectively employed as a useful metric for probing tissue architecture. Many biological tissues such as heart, muscle (soft tissue), cartilage, tendons, etc. display inherent birefringence due to their structural asymmetry, providing ground for assessment of their biological state (healthy vs. pathological) using polarized light. Linear retardance measurements have been investigated for monitoring stem cell regenerative treatments in myocardium following infarct [37]. Linear retardance has been suggested as a potential metric to identify the position of obstruction in distending bladder based on the underlying structural changes. Not surprisingly, the study claim higher sensitivity of linear retardance for such pathologies than existing imaging modalities [38]. The low level laser therapy (LLLT) has the potential to improve wound healing in skin and subsequently reduce inflammation, swelling and pain [39]. The progress in skin healing and/or repairing can be correlated to the recovery of birefringence towards higher healthy values resulting from the re-organization of collagen fibers which could be monitored with the help of polarized light [40]. Likewise, the inherent birefringence of cardiac muscle was exploited to characterize cardiac thermal injury [41].

Polarization sensitive optical coherence tomography (PS-OCT) is another clinically relevant optical imaging modality that capitalizes on polarized light for biomedical applications. It is primarily based on tissue birefringence (like optical polarimetry) with superior image resolution and greater depth of sampling. Studies have reported that reduction in tissue birefringence due to collagen denaturation in porcine tendon and skin samples resulting from thermal damage can be imaged and evaluated with the help of PS-OCT [42]. Further, spectral domain PS-OCT system has been investigated for early glaucoma detection based on the retardation, birefringence, and thickness measurement of retinal nerve fiber layer [43].

Another interesting biomedical application of polarized light is the size measurement of the scattering centers in biological tissues. Specifically, Mie theory in the single scattering framework can be used for investigating the scattering properties (such as size, shape, density, scattering coefficient, refractive index, etc.) of scattering centers. For instance, polarized light scattering-spectroscopy provided information about the refractive index of epithelial cell and the size distribution of their nuclei which can be potentially correlated to pathological (precancerous) changes for early detection in human tissues [44]. Similarly, size distribution of various scattering centers inside mammalian cells can be determined with polarized light spectroscopy [45]. Further, elastic scattering spectroscopy with polarized light revealed information about size and density of scattering centers in turbid medium [46].

In conclusion, all these studies provide support for the wide spread biomedical application and research with optical polarization, engaging both theoretical and experimental fields actively and productively. Depolarization and birefringence are the two important tissue related polarization metrics that can be effectively exploited for assessment and characterization of pathological state of biological tissues as supported by both *ex vivo* and *in vivo* studies.

1.3 Optical Polarimetry for Pathological Assessment

In this dissertation, two types of pathologies were studied through optical polarimetry; basal cell carcinoma (BCC) of skin and myocardial tissues. A brief overview of these pathologies and their assessment with polarized light has been given below.

1.3.1 Optical Polarimetry and Basal Cell Carcinoma

Human body consists of trillions of cells that grow and divide under a controlled mechanism in such a way that old and/or damaged cells are replaced by new cells. However, there are certain pathological conditions where this well-organized controlled process breaks down and the old or damaged cells keeps on continuous division without stopping resulting in the growth of extra tissue, usually called tumor. Generally, the cell

division without stopping and its subsequent spread into surrounding tissues is called cancer.

Cancer can originate in any type of cell or organ of the human body and is named accordingly. For instance, the cancer that starts in epithelial cells, muscle cells or blood forming tissue is called carcinoma, sarcoma and leukemia, respectively. It is noteworthy that about 85% of all cancers are carcinomas which may not be surprising as the epithelial cells (which form the protective linings of inside and outside body surfaces) are the most abundant cells in the human body. Further, there are several types of carcinoma; squamous cell carcinoma (SCC) arises from the squamous cells, which line many organs such as skin, stomach, lungs, intestines, bladder, and kidneys. Adenocarcinoma is the cancer of epithelial cells that produce fluids. Such cells are frequently found in the breast, colon, and prostate. Basal cell carcinoma (BCC) is another type of skin cancer that is formed in the lower (basal) layer of the epidermis.

BCC is one of the most common human malignancies, characterized by local invasiveness and low metastatic potential. Exposure to ultraviolet radiation is believed as the main risk factor for BCC incidence. Histologically, the common types of BCC are: Undifferentiated BCC includes pigmented, superficial, sclerosing, and infiltrative subtypes and differentiated BCC includes keratotic, sebaceous, adenoid, and nodular subtypes. Typically, biopsy followed by histology of the suspicious skin lesion is suggested to diagnose BCC and determine its histologic subtype. Surgery is the standard treatment for BCC, in addition to photodynamic therapy (PDT) and radiotherapy. Generally, BCC has a good prognosis [47].

Clinically, a variety of different tools for assessment and diagnosis of any suspicious lesion are available. However, histopathology being considered as the gold standard is essentially required for the final evaluation. For instance, biopsy of suspicious lesion followed by histopathology is the current standard procedure for BCC diagnosis. However, biopsy may not be practical in cases with multiple lesions such as in the case of Xeroderma Pigmentosa where the extensive number of skin lesions often make biopsy of each individual lesion very challenging while sampling only few lesions based on clinical suspicion alone may lead to a misdiagnosis or a delay in diagnosis of the invasive BCC.

Consequently, non-invasive approaches for investigating skin lesions with minimal procedural times have attracted growing interests [48]–[52]. To this end, techniques exploiting polarized light measurements are particularly important as these have the potential to explore information about the micro-architecture and biochemical composition of the skin [53], [54].

Mueller matrix polarimetry provides the complete polarization signature (depolarization, retardance, diattenuation) of the probed biological tissue. Skin tissue would be a particularly suitable model for optical polarimetric investigations owing to the highly anisotropic nature of the dense collagen and elastin fiber networks present in the skin extracellular matrix. This anisotropy gives rise to retardance which can be sensitively measured with optical polarimetry. Indeed, the loss of collagen fiber structure and integrity (and consequently linear retardance) has been associated with skin pathologies including cancer and thermal injury [55]. Further, a clinically important camera based on polarized light has been developed and successfully demonstrated in guiding the surgical margins of various skin pathologies such as precancerous, benign and cancerous tissues [30], [34], [35]. Additionally, suppression of highly scattered photons that are effectively generated from the deeper skin layers has been utilized for the depth selectivity in bioengineered connective tissues [36], [40]. This approach called polarization gating also significantly improved the image quality in terms of resolution [30], [34].

Despite characterizing various skin pathologies using optical polarimetry with significant contrast, effective statistical tools for automatic tissue classification are relatively unexplored. Appropriate classification tools that automatically discriminate tissue's pathological state based on polarimetric variables would be the ultimate goal of such studies. If successful, this goal would greatly benefit and facilitate the clinicians, particularly those who are overburden. To this end, we investigated the differences in polarization properties (depolarization, retardance, and diattenuation) for *ex vivo* normal healthy and BCC tissue samples from human skin using Mueller matrix polarimetry over the spectral region 460-800 nm. Significant differences in polarization properties of the two tissue groups have been experimentally observed. Partial least square (PLS) and

Wilks lambda statistics were employed to evaluate the potential of measured polarization properties for classification of normal and BCC tissue samples. It is noteworthy that the novelty of this work lies in investigating a powerful statistical tool for computer assisted discrimination of normal and pathological state (BCC) of tissues based on polarimetric signatures.

1.3.2 Cardiovascular Diseases

Cardiovascular diseases are a group of heart related disorders such as myocardial infarction (commonly known as heart attack), strokes, coronary heart disease, etc. that constitute one of the leading cause of death worldwide. In 2012, approximately 17.5 million deaths occurred globally due to cardiovascular diseases, which are representing about 31% of all deaths. Myocardial infarction (MI) is the major cause of heart related deaths, accounting for about 7.5 million deaths annually [56]. These statistics motivate basic science as well as clinical research for non-invasive diagnostic (in the first phase) and treatment techniques for better management of patients with cardiac diseases. Ideally, the research should focus on the development of novel non-invasive tools with the goal of personalized diagnostic and treatment of patients with cardiac disorders.

MI being the major cardiac event, the survivors may develop abnormal heart rhythms, which are typically caused by remodeling of the cardiac muscle [57]. Specifically, the electric signaling system of the heart develops malfunctions due to structural alterations of the myocardium tissue [58]. The spatial extent, position, and degree of severity of the anatomical remodeling of cardiac tissue will define the impairment in coordination of the heart electrical activity and subsequent cardiac rhythms. Such abnormal heart rhythms are called cardiac arrhythmias.

Radiofrequency ablation (RFA) is an effective treatment for focal arrhythmias [59]. During the RFA procedure, radiofrequency (RF) energy is delivered via an intra-cardiac catheter to specific spots to destroy arrhythmogenic circuits. The ablated tissue typically consists of a lesion core (i.e., coagulative necrotic area due to denaturation of proteins during the thermal treatment) surrounded by a rim of both viable and non-viable cells [60], [61]. The extent of the lesion and complete tissue destruction within the

targeted boundaries (and consequently, RFA treatment success) is difficult to assess with current techniques available in clinical electrophysiology. Parameters like catheter tip temperature, delivered power, heating time, and impedance change during RFA are monitored and used as indicators of lesion extent and quality assessment. However, failure to produce an RFA lesion that closely conforms to the target site and lesion contiguity remains a major setback to successful RF catheter ablation treatment of ventricular arrhythmias [62].

RF ablated cardiac tissue is assessed with the help of different medical imaging techniques for the assessment of possible subsequent effects on the heart function (both electrical and mechanical). Typical imaging modalities used for this purpose are magnetic resonance imaging (MRI), echocardiography (ECG), computed tomography (CT), Ultrasound (US), etc. However, each of these imaging tools has its specific advantages / shortcomings for evaluation of structural damage to cardiac tissue [63]–[65]. Therefore, basic researchers are keen to establish novel imaging modalities for better visualization of the RFA lesion and to help understanding the relationship between cardiac electrical activity and structural remodeling towards an effort for improved clinical assessment of RFA procedure and to predict the treatment outcomes.

1.3.3 Cardiac Structure and Electrical Function

The heart is responsible for sustaining blood circulation with adequate oxygen levels throughout the body. During expansion/relaxation of the right side chambers of the heart, deoxygenated blood is received from the body and then pumped to lungs during contraction. During next relaxation, oxygenated blood is drained from lung into the left side heart chambers and finally it is pumped to the body on next contraction. This cycle keeps on repeating throughout the life time. The heart contraction-relaxation cycles are controlled by spontaneously generated electrical signals in heart tissue.

The principal component of heart conduction system is the sino-atrial (SA) node - a group of natural pacemaker cells which is located in the upper part of right atrium as shown in Figure 1-1. For healthy heart, the electrical impulse initiates at the SA node and propagates radially across atria, arrives at the atrio-ventricular (AV) node- a cluster of

specialized cardiac fibers located at the floor of right atrium and finally reaches the Purkinje fibers, which are splitted into the right and left branches and extends till the end of ventricular myocardium. The electrical impulse from the terminals of the Purkinje

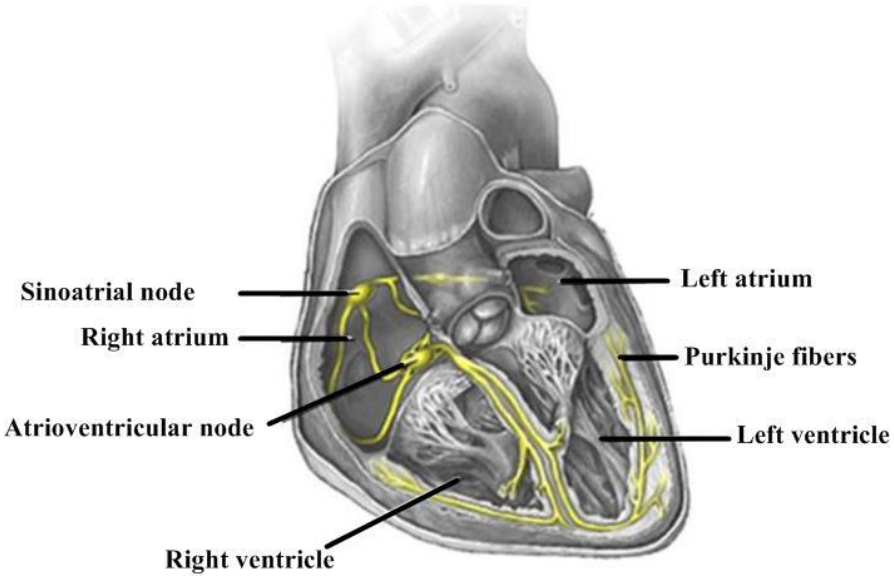

Figure 1-1 Schematic of the electrical conduction system of the heart (modified from source: https://www.nlm.nih.gov/medlineplus/ency/article/000183.htm).

fibers travels to the excitable cardiomyocytes (cardiac muscle cells), resulting in a coordinated contraction. The electric signaling pathways of the heart are shown yellow in Figure 1-1. It may be noted that the electrical signal travels down at the same speed in both the left and right cardiac branches so that both ventricles contract synchronously in healthy hearts [66].

Since cardiac muscle contraction is triggered by electrical impulses, their timing and pattern determine heart rhythm. It is noteworthy that normal rhythm is about 70-80 beats per min. For the cardiac pathological state of arrhythmias (slow, fast and/or irregular rhythms), the disordered heart rhythms can impair the capability of the heart to efficiently contract and subsequently pump adequate amount of blood to meet body's requirements resulting in severe and (occasionally) deadly cardiac events.

Cardiac arrhythmias are classified by heart's rhythm (Tachycardia: the heart beat faster than normal, and Bradycardia: the heart beat slower than normal) and by their

anatomical origin in the heart tissue (atria or ventricles). Arrhythmias arise from disturbances in cardiac electrical system such as blocked, slowed and/or extra electric signals. In addition, the arrhythmia may also evolve from the propagation of electric signals through other than normal pathways. One particular type of interest is the focal arrhythmia which arises from a discrete anatomical site in cardiac tissue. Although located at specific spots, focal arrhythmia typically triggers early cardiac activation. At times, short repetitive bursts are fired in that override/ interfere with normal heart beat [67].

Electrophysiology (EP) tests are commonly conducted to assess the function, mechanism, and performance of the electrical impulses of heart and subsequently assess the nature of arrhythmia. EP basically maps the voltage (or impedance) and its propagation through the heart substrate (endocardium and/or epicardium) via intra-cardiac catheter. This procedure facilitates to identify regions of healthy myocardium, scar (dead) tissue, and pathological zones which are believed as potential arrhythmogenic sites. The clinically defined typical cut-off voltage V thresholds are; $V > 1.5mV$ represent the healthy cardiac tissue while $V < 0.5mV$ describe the dense scar tissue. The intermediate values between these limits define the pathological zone, where the electrical impulse propagates slower leading to a potentially suspicious arrhythmogenic circuit [67].

1.4 Radiofrequency Ablation of Arrhythmogenic Myocardial Tissue

Radiofrequency ablation (RFA) offers an effective curative therapy for many symptomatic cardiac arrhythmias such as focal and monomorphic ventricular arrhythmias. During the RFA treatment, radiofrequency (RF) energy is delivered to selectively destroy arrhythmic circuits [68]. The procedure starts with the RF probe placement in the targeted volume. Subsequently, high frequency current (350–550 kHz) is supplied through the electrode into the targeted tissues. The mechanism of electromagnetic energy conversion into heat is resistive heating. Specifically, the RF electrode heats a narrow surrounding rim of tissue (< 1 mm) which is in direct physical

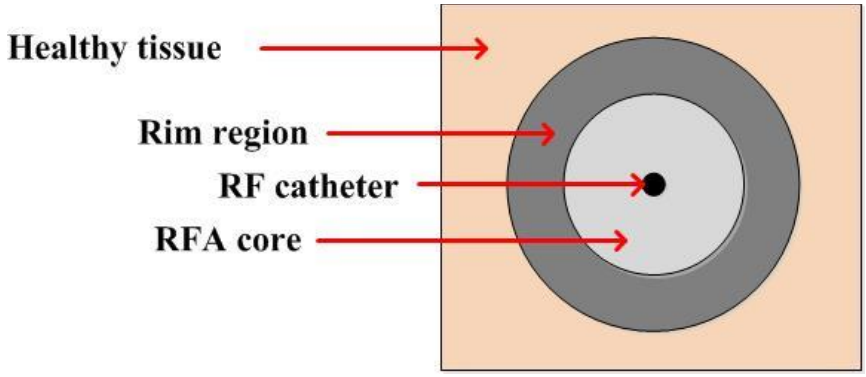

Figure 1-2 Schematic representation of radiofrequency ablation (RFA) lesion illustrating the three zones with varying degree of thermal damage; RFA core, rim and healthy tissue.

contact with the electrode. However, temperature of deeper tissue also increases due to heat conduction. Coagulative necrosis occurs at tissue temperatures above 50 ^{o}C due to denaturation of proteins during the thermal treatment and irreversible myocardial injury. This region defines the RFA core. Tissue temperatures above 100 ^{o}C will result in burning the tissue adjacent to the catheter tip, which will abruptly increase the impedance and automatically stop the RF generator from delivering more energy. This aspect is of particular importance when performing RF ablation of *ex vivo* unperfused tissue, where high temperatures at the catheter tip are reached quickly (as used in this dissertation). The temperature profile falls rapidly with the radial distance from the RF catheter where the tissue receives relatively small thermal insult [69]. Consequently, the remote tissue contains both viable and non-viable cells. This zone determines the rim region of the RF ablation lesion. In summary, ablated tissue consists of a lesion core (i.e., coagulative necrotic area) surrounded by a rim region (with viable and non-viable cells) [60], [61]. Figure 1-2 shows the schematic of a typical RFA lesion.

The current density profiles in the cardiac tissue and the subsequent RFA lesion dimensions are primarily determined by size and geometry of RF electrode, electrode-tissue contact and tissue properties such as specific heat, electric resistivity (or conductivity), etc. RFA lesion size is also proportional to duration of RF current delivery and applied power. The RF power regime used most frequently in clinic is 20-40 W.

1.4.1 Assessment of Radiofrequency Ablated Tissue with Conventional Imaging

The palpable zone defined by the RFA lesion and complete tissue destruction within the targeted boundaries are indicators of the RFA treatment efficacy. However, the spatial extent of RFA lesion is difficult to assess with current evaluation techniques available in clinical electrophysiology. Consequently, the assessment of lesion size and extent is accomplished indirectly. Specifically, parameters like RF catheter tip temperature, delivered energy, heating time, and impedance change during RFA are monitored and correlated to the lesion extent. However, the major challenge for successful RFA treatment is the complication to deliver an RFA lesion that closely mimic to the target site [62].

The dimensions and spatial extent of RF ablation lesion are directly correlated to the efficacy of clinical outcome of the RFA treatment. Therefore, proper characterization of RFA lesion to assess the elimination of the targeted arrhythmic circuit, predict treatment success and identify possible reasons for treatment failure is essentially required. To this end, the clinically available medical imaging techniques include ultrasound (US), computed tomography (CT) and magnetic resonance (MR); each have its specific advantages / shortcomings for both RFA guidance and post-RFA evaluation, as discussed below.

Several studies have demonstrated the capability of US to monitor thermal lesions *in vitro.* Specifically, intra-cardiac echocardiography has been shown to assess the RF catheter-tissue contact, heating efficiency during RF energy application, and lesion creation [63], [64]. However, the ability of this technique to accurately quantify the spatial extent of thermal damage is hindered by its relatively poor spatial resolution. CT being based on the differences in attenuation coefficients of the investigated tissue has poor soft tissue contrast and consequently provides limited information about the spatial extent of RFA lesion. The delineation of the lesion rim area with CT imaging is particularly prone to ambiguities [65]. MR is a more promising imaging modality for visualization and monitoring of the RF lesion [61]. However, it demands highly

sophisticated and expensive technology with time consuming imaging algorithms. Specifically, high-quality MR images are assured for perfectly motionless patients during the long procedural times (typical scan times are about 30-45 minutes). The constant cardiac motion creates challenges in obtaining sharp images essentially required for proper pathology delineation. More importantly, irregular heartbeats (arrhythmia) may cause significant artifacts in cardiac MR images. Consequently, there is a need for better and/or more affordable imaging methods to assess RFA lesion extent.

1.4.2 Assessment of Radiofrequency Ablated Tissue with Optical Imaging

Optical imaging modalities may offer insights into microstructural characteristics of myocardial tissue and has been suggested for the assessment of RFA induced thermal damage of myocardium [70]–[73]. For instance, optical coherence tomography (OCT) has been shown to identify RFA lesion extent based on observed changes in birefringence and scattering coefficient [70]–[72]. It is noteworthy that OCT has superior resolution (both axially and laterally) in scattering media like cardiac tissue, provides depth-resolved images thru the mechanism of coherence gating. However, it offers reduced field of view and shallower sampling / penetration depth compared to other optical imaging techniques [74]. Further, the relatively complicated optics required for cardiac OCT also hinders its frequent clinical applications.

Photoacoustic imaging (PI) provokes another important avenue for RFA lesion characterization. PI can generate optical absorption maps based on endogenous chromophore concentrations (such as deoxy-hemoglobin [Hb]), and has been utilized for assessment of RFA lesions [73]. This emerging optical imaging approach benefits from a large penetration depth (~1 cm in the cardiac tissue) [73] and depth-resolved images. However, the PI probe requires physical contact with the investigated tissue via acoustic coupling and again relatively complex instrumentation and signal processing. Further, photoacoustic RFA studies have been unable to demonstrate reliable measurements past 3 mm in depth. Moreover, photoacoustic comparison with histological RFA margins

showed only 69% and 36% agreement with lesion size in the lateral and axial directions, respectively [73].

Polarization sensitive OCT (PS-OCT) is the advance version of conventional OCT; it additionally measures tissue birefringence (a tissue inherent characteristic that arises from its anisotropic nature) by exploiting polarized light [75]. More specifically, difference in refractive indices for two orthogonal propagation directions in the given tissue manifest as direction-dependent optical properties. Cardiac tissue is primarily composed of highly asymmetric cardiomyocytes and collagen fibers resulting in tissue birefringence which can be effectively quantified with PS-OCT. Further, loss or decrease of tissue birefringence may result from structural alterations (such as RF ablation) in healthy tissue. Indeed, significant contrast in tissue birefringence between healthy and thermally damaged (induced by laser) has been observed previously [76]. Further, the size of ablated region was determined with the help of phase image thresholding and comparison with histopathological sections [42]. These studies indicate that it would be particularly interesting to use optical polarization measurements alone (polarimetry) for the assessment RFA lesion.

In summary, polarized light could offer rich information content about myocardial tissue architecture and morphology [37], which could potentially be exploited for non-invasive RFA assessment. Although polarized light has been used in many important areas of biomedical research (as discussed below), however characterization of cardiac RFA lesion with polarized light measurement is relatively unexplored.

1.4.3 Assessment of Radiofrequency Ablated Tissue with Polarization Imaging

Cardiac tissue is a particularly suitable site for polarimetric investigations owing to the highly anisotropic nature of its constituent tissues (e.g. cardiomyocytes, collagen fibers), as shown in Figure 1-3. This anisotropy gives rise to linear retardance (closely related to the property of optical birefringence), the magnitude and direction of which can be sensitively measured with optical polarimetry. Previously, polarization imaging has been employed for analysis of myocardial infarction (MI). This study demonstrated elevated

linear retardance at the infarct scar regions, indicating increased collagen content which was consistent with picrosirius red histology staining [77]. The findings of the study were further supported by the results of non-linear (second harmonic generation) microscopy.

In addition, structural alterations associated with myocardial infarction and treatment-induced remodeling has been studied using polarized light measurements. This work revealed decreased linear retardance in infarcted regions presumably due to the disruption of cardiomyocytes alignment [37]. Polarization imaging further explored the partial recovery of linear retardance toward the higher healthy values after stem cells regenerative treatment of the infarcted myocardium [37]. Collectively, these studies illustrate the capability of optical polarimetry for distinguishing between healthy and structurally altered (such as RF-ablated) regions of myocardial tissue.

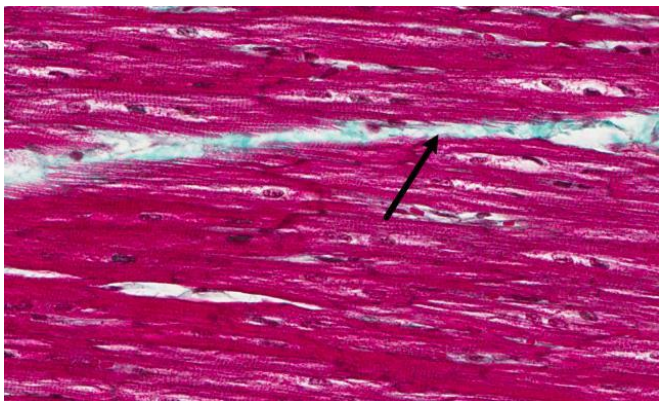

Figure 1-3 Histology of myocardium tissue with Masson's trichrome staining where the cytoplasm appears pink, nuclei are dark red, and collagen is stained blue, as pointed by the black arrow.

1.5 Thesis Aims and Objectives

Polarization imaging could provide rich information about the architecture of given biological tissue as polarization metrics such as depolarization, retardance, and diattenuation are sensitive to the underlying tissue morphology. Specifically, the pathological state of tissue (healthy vs. structurally altered) could be diagnosed and visualized with superior image quality by using polarized light, as indicated by previous studies [30], [35], [37], [78]. For example, polarization imaging has been used efficiently

for the assessment of healthy vs. infarcted cardiac tissue and monitoring of stem cells regenerated treatment after myocardial infarction [37], [79]. Further, various degrees of structural alteration could be delineated in the corresponding polarized light image due to the higher image contrast. For instance, polarization imaging has demonstrated contrast in various skin pathologies such as precancerous, benign and cancerous tissues [30], [34], [35]. Based on these studies, we hypothesize that necrosis of thermally damaged (RF ablated) myocardial tissue leads to a loss of structural anisotropy resulting in lower linear retardance and depolarization which could be potentially mapped by polarization imaging. Further, differences in polarization metrics at various zones of the structurally altered myocardial tissue could be correlated to the degree of thermal damage, enabling demarcation of polarization images into corresponding segments. That said, the specific aims and objectives of this thesis are:

1) To explore the capability of optical polarimetry to characterize normal (healthy) and BCC human skin tissue followed by statistical tools that might help for computer-assisted classification of the two tissue groups
2) To explore the capability of optical polarimetry to visualize a typical myocardial RFA lesion including the necrotic core and the rim regions. In particular, to investigate the contrast in depolarization and linear retardance images (both magnitude and orientation) for normal and RF-ablated tissues in *ex-vivo* healthy porcine hearts, using Mueller matrix polarimetry
3) To quantitatively segment the polarization image of RFA lesion in three zones (RFA core, rim and healthy regions) based on the observed differences in total depolarization for the aforementioned three regions, with quantitative comparison and/or validation from histopathology images

1.6 Thesis Outline

This thesis is mainly focused on the assessment of pathological states of biological tissues with the help of Mueller matrix polarimetry. Specifically, optical polarimetry is utilized for differentiation of *ex vivo* normal and BCC tissue samples followed by

proposed statistical tools for computer aided classification of the two tissue groups. Further, analysis of a typical myocardial RFA lesion with polarization imaging is presented. RFA lesions were generated at different locations of porcine heart using a range on RF parameters and subsequently analyzed by Mueller matrix polarimetry along with polar decomposition method. The polarization images of the ablated tissue were compared and validated with histology. Afterwards, an automated algorithm was developed and utilized to segment the polarization images in three zones of RFA core, rim and healthy regions.

Chapter 2 provides a comprehensive overview of the interaction of polarized light with matter. We discuss electromagnetic wave equation and polarization ellipse along with their salient features, followed by the basic types of mathematical formalism for polarized light such as Stokes and Jones vector formalism and coherency matrix. Further, Mueller matrix calculus for the description of polarized light interaction with matter and its detailed decomposition algorithm (polar decomposition) to extract individual polarization parameters are provided.

Chapter 3 provides the details of experimental methodology. Extraction and preparation of normal and BCC human skin samples for polarimetric and histologic studies are discussed. Instrumentation for radiofrequency ablation generation procedure, Mueller matrix point and imaging setup followed by the composition of Mueller matrix from the raw images is presented. We conclude with cardiac samples preparation methodology for ablation, polarimetry and histopathology, followed by the description of some important statistical tools used in this work.

Chapter 4, 5 and 6 presents the experimental results along with their discussion. Specifically, results from the polarized light measurements for *ex vivo* normal and BCC tissue samples from human skin are presented in chapter 4. The observed differences in polarization properties of the two tissue groups have been analyzed for computer-aided classification with help of statistical tools such as partial least square (PLS) and Wilks lambda statistics. Afterwards, results of characterization of RFA lesion in the myocardial tissue by optical polarimetry, their comparison and validation from histopathology, followed by a comprehensive discussion are shown in chapter 5. Exploiting the observed

contrast in polarization images for their segmentation in the RFA core, rim and healthy regions along with quantitative validation from corresponding ground truth (histology) images is demonstrated in chapter 6. The thesis is concluded in chapter 7; guidelines and future directions for extension of the current study are also provided.

2 Formalism for Polarization of Light

2.1 Introduction

Polarization is a property of all electromagnetic waves including light that arises from its transverse nature and is related to the locus of electric field ($E\,(z,t)$) in space as a function of time (t). Specifically, the $E\,(z,t)$ vector remains in a single plan with temporal evolution for linear polarization; it traces an ellipse for elliptical polarization and circle for circular polarization. Finally, random positions of $E\,(z,t)$ vector in space at various time points signifies towards unpolarized light [12].

The first important mathematical formalism of polarized light was surfaced by Sir George Gabriel Stokes in 1852. The proposed methodology was based on the physically measurable light parameter (i.e. intensity) of different polarization states. These intensities were named Stokes parameters. The approach was versatile in describing total, partial and unpolarized light states and robust for frequent use even today. Nevertheless, subsequent mathematical descriptions of polarized light followed [2]. For instance, Jones formalism represented polarized light as a matrix in the framework of electromagnetic theory. This technique offered great simplicity in dealing totally polarized light but was not properly suited for partially polarized states [1], [80]–[83]. Coherency matrix formalism was staged in attempt to account for the description of partial polarization states [84]. Importantly, the elements of coherency matrix were directly correlated to Stocks parameters [85].

Jones formalism for polarized light expresses the limitations that it can't handle the incident beam depolarization resulting from light tissue interactions. Stocks-Mueller calculus is perhaps the most frequently used tool for handling such problems as indicated by the accumulated experimental work [17], [37], [86]–[92]. Mueller matrix provides a comprehensive representation of the changes in the probing light polarization state by the

investigated sample. Consequently we used Stocks-Mueller formalism throughout this thesis to account for the complete set of polarization properties of biological tissues.

It is noteworthy that Mueller matrix merely provides a starting point to elucidate the complete polarimetric fingerprint of a given sample and does not directly permit for quantitative analysis of individual polarimetric properties. Instead subsequent decomposition of Mueller matrix is essential for visualizing the individual polarization metrics quantitatively. Different algorithms have been proposed for decoding Mueller matrix [93]–[96]. Nevertheless, the most widely used polar decomposition stage a convincing technique in tissue polarimetry. Briefly, Mueller matrix is splitted into three elementary polarization matrices; a diattenuator matrix, followed by retarder matrix, and then followed by depolarizer matrix [94]. These elementary matrices are further decomposed to segregate the individual polarization properties for subsequent analyses. We employed polar decomposition method for extraction of polarization characteristics from Mueller matrix throughout this thesis.

Investigating polarized light interaction with turbid media like biological tissues is attracting growing interest. Such media favor multiple scattering of the polarized light and the subsequent scrambling of coherence essentially attests depolarization. The direction and phase randomization of the incident polarization beam depends on multiple parameters of both interacting beam and the probed medium. These metrics include the relative refractive index, size, shape and density of the scattering centers of the medium and the incident polarization state. Various scattering realms such as Rayleigh-Gans scattering, Mie scattering, and Rayleigh scattering are discriminated on the basis of these parameters and are discussed in detail in literature [12], [97].

2.2 Polarization of Light

Classically, polarization of light refers to the pattern followed by $E\ (z,t)$ vector in space and time. Light is said to be linearly polarized if the oscillations of its $E\ (z,t)$ vector are confined to a single plan in time [98]. If the tip of $E\ (z,t)$ vector traces an ellipse (circle) in space as a function of time, light is said to be elliptical (circular) polarized.

Suppose that $E\ (z,t)$ is the electric field vector of light propagating in z-direction at time t. The two components of $E\ (z,t)$ oscillating in the xz- and yz-plane can be given as

$$E_x(z,t) = E_{0x}\, cos(kz - \omega t + \delta_x) \qquad (2\text{-}1)$$

$$E_y(z,t) = E_{0y}\, cos(kz - \omega t + \delta_y) \qquad (2\text{-}2)$$

where $E_x(z,t)$ and $E_y(z,t)$ are the x- and y- components of E (z, t) respectively, E_{0x} and E_{0y} are the corresponding amplitudes, δ_x and δ_y are the phases corresponding to these components, $k = 2\pi/\lambda$ is the wave vector, λ is the wavelength, and ω is the angular frequency of electromagnetic wave. It is clear that the sinusoidal oscillation of $E_x(z,t)$ and $E_y(z,t)$ are described by their amplitudes and relative phase. These components can be written in a more compact form as

$$E_x(z,t) = E_{0x} e^{i(kz-\omega t+\delta_x)} \qquad (2\text{-}3)$$

$$E_y(z,t) = E_{0y} e^{i(kz-\omega t+\delta y)} \qquad (2\text{-}4)$$

$$E(z) = \begin{bmatrix} E_x \\ E_y \end{bmatrix} = \begin{bmatrix} E_{0x} e^{i(\delta_x)} \\ E_{0y} e^{i(\delta_y)} \end{bmatrix} \qquad (2\text{-}5)$$

where $\delta = \delta_y - \delta_x$ is the phase difference between the two components of $E\ (z,t)$ vector. Also we have assumed that the phase difference in the electric field vectors is constant at all points in space so that the space-time propagation factor $kz - \omega t$ from Equation (2-3) and (2-4) can be dropped, then

$$E = \begin{bmatrix} E_{0x} \\ E_{0y} e^{i\delta} \end{bmatrix} \qquad (2\text{-}6)$$

This is the Jones vector representation of electric field propagation. Jones formalism represents polarized light as a matrix in the framework of electromagnetic theory and offer great simplicity in dealing totally polarized light, nevertheless it is not suited for dealing with partially polarized light states [1], [80]–[83].

2.3 Polarization Ellipse

It is interesting to note that the tip of $E\ (z,t)$ vector of a polarized wave traces a well-define pattern along its propagation direction. The geometric shape subtended by the tip of $E\ (z,t)$ vector can be described by manipulating Equation (2-1) and (2-2). After simple algebra, the resulting equation is

$$\left[\frac{E_x}{E_{0x}}\right]^2 + \left[\frac{E_y}{E_{0y}}\right]^2 - 2\frac{E_x E_y}{E_{0x}E_{0y}}\cos\delta = \sin^2\delta \qquad (2\text{-}7)$$

Equation (2-7) represents an ellipse. Since Equation (2-7) is particularly true for polarized light, the ellipse is accordingly called polarization ellipse. The major and minor axes of the polarization ellipse are represented by the components E_x and E_y of $E\ (z,t)$ vector, respectively. Equation (2-7) mathematically describes the most general shape traced by the $E\ (z,t)$ vector, the ellipse. Consequently any polarization state of light such as any circular and/or linear state can be derived from Equation (2-7) using suitable combinations of phase and amplitudes, as discussed below.

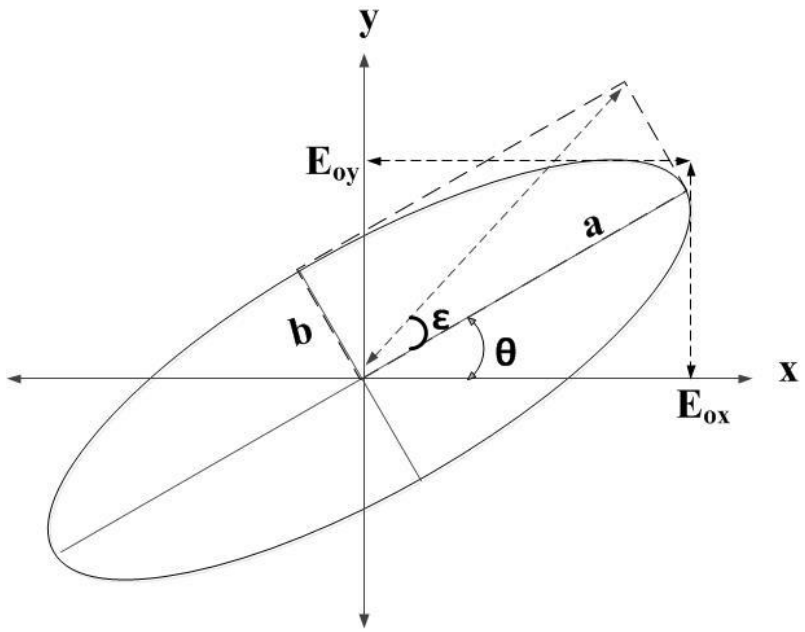

Figure 2-1 Polarization ellipse illustrating different elliptical parameters; a and b are the semi -major and -minor axes, respectively, ε is the ellipticity, θ is the azimuthal angle.

In Equation (2-7), the cross term $E_x E_y$ indicates that the polarization ellipse is rotated with respect to x-axis. It may be noted that this rotation of the ellipse is defined by the orientation of the $E\,(z,t)$ vector in space and is quantified by an angle called azimuth, which is quantified as the angle subtended by major-axis of the polarization ellipse with the x-axis as shown in Figure 2-1. Mathematically

$$\tan\theta = \frac{E_{0y}}{E_{0x}} \qquad (2\text{-}8)$$

where θ is the azimuth angle with limits [0, π/2].

The nature of a particular polarization state can be probed from the polarization ellipse. Specifically, it provides a measure of the circular, elliptical or linear character of polarization state. This goal is established by the parameter called ellipticity which is defined as

$$\tan\varepsilon = \pm\frac{b}{a} \qquad (2\text{-}9)$$

where ε is the ellipticity angle with limit [-π/4, π/4], a and b are the semi major and semi minor axes of the ellipse. Plus sign indicates right-handed while minus sign indicates left handed polarizations. For zero semi minor axis ($b = 0$), the ellipticity will also be zero which represent linear polarization state. For equal semi major and semi minor axes($a = b$), the ellipticity will be equal to one which indicates circular polarization state. Any other combination of a and b will correspond to elliptical polarization states. Table 2-1 illustrates the polarization states and their required criteria for presentation on the polarization ellipse.

Another important parameter for describing the shape of the ellipse is the eccentricity which is essentially related to ellipticity by the following relation

$$\chi = \sqrt{1-\varepsilon^2} \qquad (2\text{-}10)$$

where χ is the eccentricity with limits [0, 1]. The shape of the ellipse is completely circular for $\chi = 0$, ellipse for $\chi > 0$ (which becomes progressively thinner as χ increases) and $\chi = 1$ for a line.

Table 2.1 Various polarization states and their criteria for representation on polarization ellipse

Polarization state	Symbol	Criteria
Linear horizontal	↔	$E_{0y} = 0$
Linear vertical	↕	$E_{0x} = 0$
Linear $+45^0$	⤢	$E_{0x} = E_{0y}$ & $\delta = 0$
Linear -45^0	⤡	$E_{0x} = E_{0y}$ & $\delta = \pi$
Right circular	↻	$E_{0x} = E_{0y}$ & $\delta = \pi/2$
Left circular	↺	$E_{0x} = E_{0y}$ & $\delta = -\pi/2$

It is noteworthy that the polarization ellipse holds great promise for illustrating all polarization states for totally polarized light. However, it faces challenges for representing unpolarized or partially polarized light. Further, rotation and ellipticity angle, the two important parameters of polarization ellipse, are not directly measureable. Moreover, measurement of instantaneous polarization state represented by the ellipse remains elusive due to high optical frequencies ($\approx 10^{15}$ Hz).

2.4 Stokes Formalism of Light Polarization

Sir George Gabriel Stokes proposed the first promising formalism of polarized light in 1852. The approach is of particular interest as it is based on physical quantities and describes total, partial and unpolarized light states [2]. Stokes formalism also sidesteps the instantaneous changes in the polarization ellipse, as mentioned above.

For the mathematical description of Stoke formalism, we start by taking the time average of the polarized field measurable, i.e. Equation (2-7)

$$\left[\frac{< E_x(t) >}{E_{0x}}\right]^2 + \left[\frac{< E_y(t) >}{E_{0y}}\right]^2 - 2\frac{< E_x(t)E_y(t) >}{E_{0x}E_{0y}}\cos\delta = \sin^2\delta \quad (2\text{-}11)$$

where the symbol < > indicates the time average while $\delta = \delta_y(t) - \delta_x(t)$ is the relative phase shift. Simple mathematical manipulation of Equation (2-11) leads to the following

$$(E_{0x}^2 + E_{0y}^2)^2 - (E_{0x}^2 - E_{0y}^2)^2 - (2E_{0x}E_{0y}\cos\delta)^2 = (2E_{0x}E_{0y}\sin\delta)^2 \quad (2\text{-}12)$$

$$S_0^2 = S_1^2 + S_2^2 + S_3^2 \quad (2\text{-}13)$$

where S_0, S_1, S_2, and S_3 are the observable of the polarization field (in the units of watts per steradian) and are called Stoke parameters, defined as

$$S_0 = E_{0x}^2 + E_{0y}^2 \quad (2\text{-}14)$$

$$S_1 = E_{0x}^2 - E_{0y}^2 \quad (2\text{-}15)$$

$$S_2 = 2E_{0x}E_{0y}\cos\delta \quad (2\text{-}16)$$

$$S_3 = 2E_{0x}E_{0y}\sin\delta \quad (2\text{-}17)$$

Stokes parameters are typically presented in a more compact form, called the Stoke vector, as

$$S = \begin{bmatrix} S_0 \\ S_1 \\ S_2 \\ S_3 \end{bmatrix} = \begin{bmatrix} E_{0x}^2 + E_{0y}^2 \\ E_{0x}^2 - E_{0y}^2 \\ 2E_{0x}E_{0y}\cos\delta \\ 2E_{0x}E_{0y}\sin\delta \end{bmatrix} \quad (2\text{-}18)$$

Physically, the first Stoke parameter S_0 describes the total intensity of light beam. The second Stoke parameter S_1 illustrate the linear horizontal or vertical polarization, S_2 indicates linear +45^o or -45^o and S_3 represents right or left circular polarization.

The azimuth and ellipticity angles of the polarization ellipse can be redefine in terms of Stokes parameters as

$$\tan\theta = \frac{1}{2}\left(\frac{S_2}{S_1}\right) \qquad (2\text{-}19)$$

$$\sin\varepsilon = \frac{1}{2}\left(\frac{S_3}{S_0}\right) \qquad (2\text{-}20)$$

It is interesting to incorporate the case of partial or unpolarized light in the Stokes formalism by defining a new parameter, called the degree of depolarization (DOP) as

$$DOP = \frac{\sqrt{S_1^2 + S_2^2 + S_3^2}}{S_0} = \frac{I_{pol}}{I_{tot}}\ , 0 \le DOP \le 1 \qquad (2\text{-}21)$$

where I_{pol} and I_{tot} represents the polarized and total light intensity, respectively. Obviously, $DOP = 1$ indicates totally polarized light while $DOP = 0$ stands for unpolarized light. Intermediate values between these two extremes describe partially polarized light.

Likewise, relations for the degree of linear polarization ($DOLP$) and the degree of circular polarization ($DOCP$) can be given as

$$DOLP = \frac{\sqrt{S_1^2 + S_2^2}}{S_0}\ , 0 \le DOLP \le 1 \qquad (2\text{-}22)$$

$$DOCP = \frac{S_3}{S_0}\ , 0 \le DOCP \le 1 \qquad (2\text{-}23)$$

2.5 Coherency Matrix Formalism

Coherency matrix formalism is essentially an elegant and fascinating representation of the partially polarized light beam by a 2 x 2 matrix [84]. It is intriguing to note that totally polarized and completely unpolarized light can be treated as special cases of partially polarized light. The inherent description of second order statistical properties and direct correlation with Stokes parameters shows the extraordinary richness of the compact coherency matrix formalism.

The coherency matrix is defined as

$$O_2 = \begin{bmatrix} O_{xx} & O_{xy} \\ O_{yx} & O_{yy} \end{bmatrix} = \begin{bmatrix} < E_x E_x^* > & < E_x E_y^* > \\ < E_y E_x^* > & < E_y E_y^* > \end{bmatrix} \quad (2\text{-}24)$$

where * represents the complex conjugate and the subscript shows the dimension of coherency matrix.

To establish correlation between the coherency matrix and Stokes parameters, we revisit Equations (2-18) which can be written as

$$S_0 = < E_x E_x^* > + < E_y E_y^* > \quad (2\text{-}25)$$

$$S_1 = < E_x E_x^* > - < E_y E_y^* > \quad (2\text{-}26)$$

$$S_2 = < E_x E_y^* > + < E_y E_x^* > \quad (2\text{-}27)$$

$$S_3 = i(< E_x E_y^* > - < E_y E_x^* >) \quad (2\text{-}28)$$

These equations can also be written as

$$S_0 = O_{xx} + O_{yy} \quad (2\text{-}29)$$

$$S_1 = O_{xx} - O_{yy} \quad (2\text{-}30)$$

$$S_2 = O_{xy} + O_{yx} \quad (2\text{-}31)$$

$$S_3 = i(O_{xy} - O_{yx}) \quad (2\text{-}32)$$

The trace of the coherency matrix $tr(O_2)$ gives total light intensity, the off diagonal elements indicates correlation between the orthogonal components of electric field vector (E_x & E_y). The determinant $det(O_2)$ of coherency matrix can be correlated to the DOP such that for $det(O_2) = 0$ the light is completely polarized while $det(O_2) > 0$ corresponds to partially polarized light. Furthermore, details of coherency matrices for various polarization states and the relationship of coherency matrix with Pauli spin matrices can be found in literature [85], [99], [100].

2.6 Poincare Sphere Representation

Poincare sphere is a versatile graphical representation tool for any polarization state in 3D space. It addresses the shortcomings of the polarization ellipse, discussed above. Further, it conveniently describes the polarization transformation generated in the probing beam resulting from the interaction with any optical device or media.

Poincare sphere is a sphere of unit radius centered on rectangular coordinate system. Any point on or within the unit sphere uniquely represent a polarization state. The coordinates of a point on the sphere are the three normalized Stokes parameters of the represented polarization state. The distance of a point from the center of the sphere (origin) is related to the degree of polarization. Specifically, the origin shows unpolarized light, points on the surface of the sphere represent completely polarized states while points located within the sphere describe partially polarized states.

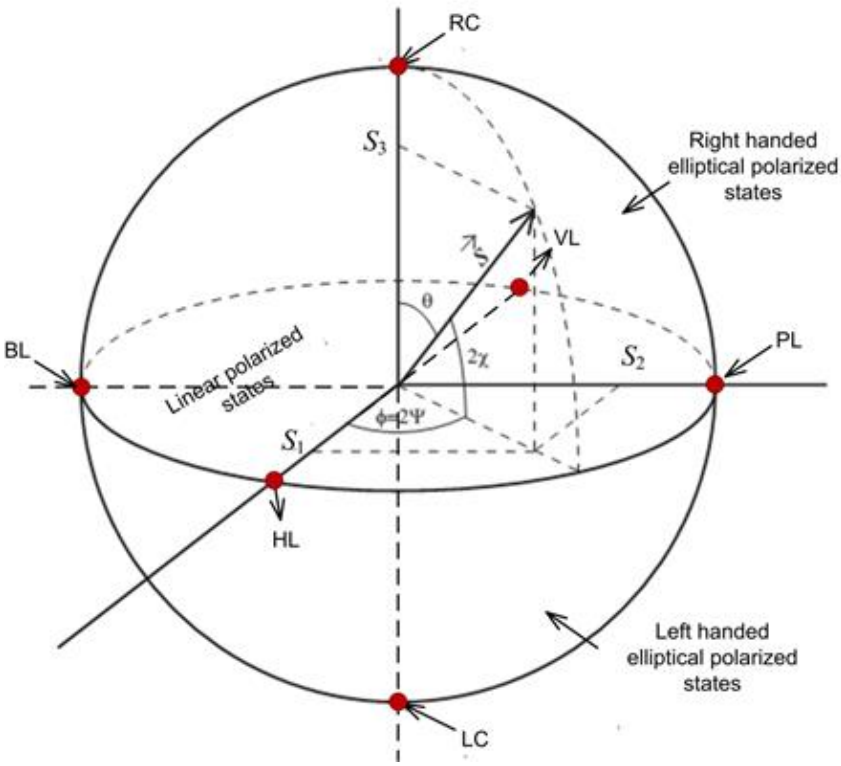

Figure 2-2 Schematic of Poincare sphere representing the positions of various polarizations states.

Figure 2-2 illustrates the schematic of a typical Poincare sphere with the positions of various polarization states shown by red solid dots. All linear polarization states are located on the equator while right and left circular states at the north and south poles of the Poincare sphere, respectively. The locations of various polarization states on the Poincare sphere are: Linear horizontal polarization HL (0^o, 0^o), linear +45 polarization PL (90^o, 0^o), linear vertical polarization VL (180^o, 0^o), linear -45 polarization BL (270^o, 0^o), right circular polarization RC (0^o, $+90^o$), left circular polarization LC (0^o, -90^o).

Elliptical polarization lies at intermediate space between poles and equator of the sphere. Northern hemisphere is occupied by right-handed elliptical states while southern hemisphere is occupied by left-handed elliptical states.

2.7 Polarized Light Propagation in Turbid Medium

Medium like biological tissues that exhibits both absorption and scattering properties is called turbid medium. Polarized light propagating through such a medium is strongly influenced by both absorption and scattering properties of the medium. Subsequently, these optical properties provide the first intimation to the polarimetric signature of the medium. Conversely, polarization properties can be associated with the biochemical and morphological parameters of the tissue. For instance, scattering and consequently the rate of depolarization of incident polarized light depends on tissue parameters like density, size, shape and refractive index of the scattering centers present in the medium. Tissue biopolymers like collagen, elastin, and myosin show intrinsic linear retardance. In addition, asymmetric (chiral) structure of glucose provoke phase shift between right and left circularly polarized light and subsequently cause optical rotation. Optical rotation measurement of light scattered from tissue therefore opens potential applications in non-invasive quantification of *in vivo* glucose levels.

Interaction of the polarized light with turbid medium (tissue) causes alteration in most polarization properties of the incident beam simultaneously. This polarization transfer function of the medium is comprehensively described by Mueller matrix $\boldsymbol{M}$ which provides the complete finger print of the medium. In the following section we

introduce the fundamentals of Mueller matrix calculus with special emphasis on tissue polarimetry.

2.8 Stokes-Mueller Polarimetry

The polarization state of light can be completely described by a four-element vector, called a Stokes vector, $\boldsymbol{S}$ = [I Q U V]^T, as discussed above. The elements I, Q, U, and V represent the total intensity, intensity difference between horizontal and vertical linear polarization, intensity difference between linear polarization at ± 45 degrees, and intensity difference between right and left circular polarization, respectively. The complete set of polarization properties of the investigated sample are described by its 4x4 Mueller matrix, **M**. In this Stokes-Mueller formalism, the interaction of a light beam of input polarization state $\boldsymbol{S_i}$ with a given sample of Mueller matrix **M** can be represented as

$$\boldsymbol{S_o} = \mathbf{M} \bullet \boldsymbol{S}_i \qquad (2\text{-}33)$$

where $\boldsymbol{S_o}$ is the output Stokes vector after interaction with the sample. The Mueller matrix **M** is a 4 x 4 matrix, given as

$$M = \begin{bmatrix} m_{00} & m_{01} & m_{02} & m_{03} \\ m_{10} & m_{11} & m_{12} & m_{13} \\ m_{20} & m_{21} & m_{22} & m_{23} \\ m_{30} & m_{31} & m_{32} & m_{33} \end{bmatrix} \qquad (2\text{-}34)$$

All 16 elements of the **M** are real and dimensionless. Further, **M** is typically the function of wavelength and the propagation vector of the incident polarized light. Generally, the elements of the **M** are not physically interpreted individually; however they can be correlated to certain polarimetric properties of the medium.

The experimentally-measured tissue Mueller matrix **M** is a complete description of all simultaneously occurring polarimetric processes. That is, all the polarimetric effects of the sample are reflected in the 16 elements of the Mueller matrix **M** in a 'lumped', complex format. For biological tissues, the dominant polarization effects are depolarization, linear retardance (birefringence) and diattenuation. Extraction of these individual polarimetry metrics from the all-encompassing **M** necessitates further decomposition of the Mueller matrix, as outlined below.

2.9 Mueller Matrix Decomposition

The Mueller matrix $\boldsymbol{M}$, is the polarization transfer function of the biological tissues and contains the complete set of polarimetric tissue properties in its 16 elements. However, $\boldsymbol{M}$ represents the simultaneous effect of all sample polarization properties, and must be analyzed further to isolate the polarization properties of interest (i.e., depolarization, linear retardance, diattenuation, etc.). Mathematical decomposition of $\boldsymbol{M}$ into constituent "basis" matrices to extract these individual polarization properties is one way to "decode" the information contained in the Mueller matrix. A variety of different decompositions have been proposed and compared [94], [95], [101]. For example, comparisons between polar and differential decompositions have shown agreement in derived linear retardance and depolarization [101]. Taking this agreement into account, and the fact that previous polarimetry studies of the biological tissues have used Lu-Chipman polar decomposition, we present mathematical details of this algorithm.

Polar decomposition is described in length elsewhere [94]. Briefly, the Mueller matrix $\boldsymbol{M}$ of the sample is expressed as the product of three component matrices, written as the product of diattenuator followed by a retarder followed by the depolarizer matrix, as given below

$$\boldsymbol{M} = \boldsymbol{M_{\Delta}} \bullet \boldsymbol{M_{R}} \bullet \boldsymbol{M_{D}} \qquad (2\text{-}35)$$

where $\boldsymbol{M_{\Delta}}$, $\boldsymbol{M_{R}}$, and $\boldsymbol{M_{D}}$ are the component "basis" matrices associated with depolarization, retardance, and diattenuation, respectively. Each of these matrices describes a basic polarization property of the probed tissue. It may be noted that these effects occur simultaneously in tissue due to its turbid and heterogeneous nature, whereas each basis matrix quantifies these effects individually. Mathematical and physical consistencies and interpretations of the polar decomposition approach have been discussed at length elsewhere [94]. However, we briefly discuss the decomposition algorithm along with some necessary interpretation of the terms involved in polar decomposition scheme.

Before discussing the polar decomposition of Mueller matrix $\boldsymbol{M}$, it is noteworthy to mention that $\boldsymbol{M}$ can be classified into two different categories based on the polarimetric properties of the medium in question. First, if the degree of polarization (Equation (2-21)) of probing light beam is preserved after passing through the medium, the medium is called non-depolarizing; the diattenuation and retardance are the two prominent effects of non-depolarizing medium. For such medium, the basis depolarization matrix $\boldsymbol{M_\Delta}$ in the decomposition algorithm (Equation (2-35)) is essentially zero and need not to be considered for subsequent analysis. For second category of the medium, the depolarizing medium, the degree of polarization (Equation (2-21)) of probing light beam is not preserved after interaction with such medium. In this case, the basis depolarization matrix $\boldsymbol{M_\Delta}$ in the decomposition algorithm (Equation (2-35)) is essentially non-zero which significantly increases the complexity of subsequent decomposition analysis.

2.9.1 Diattenuator

We start with the detail algorithm of the polar decomposition by considering an arbitrary Mueller matrix $\boldsymbol{M}$, given as

$$\boldsymbol{M} = \begin{bmatrix} m_{00} & m_{01} & m_{02} & m_{03} \\ m_{10} & m_{11} & m_{12} & m_{13} \\ m_{20} & m_{21} & m_{22} & m_{23} \\ m_{30} & m_{31} & m_{32} & m_{33} \end{bmatrix} \tag{2-36}$$

where m represent the element of $\boldsymbol{M}$ in general. The first and second letter of subscript shows the row and column number of the corresponding element, respectively.

The diattenuation information of the medium are 'encoded' in the first row of $\boldsymbol{M}$. Specifically omitting the first element m_{00}, the first row of $\boldsymbol{M}$ describes the diattenuation vector completely. Another related polarimetric parameter of the medium is polarizance; the property of the medium through which it converts unpolarized light to polarized light. The polarizance details are 'encoded' in the first column of $\boldsymbol{M}$. With the help of these two polarimetric parameters, the $\boldsymbol{M}$ can be written in a more compact form as

$$\boldsymbol{M} = \begin{bmatrix} m_{00} & \vec{\boldsymbol{D}}^{\boldsymbol{T}} \\ \vec{\boldsymbol{P}} & \boldsymbol{m} \end{bmatrix} \tag{2-37}$$

where the superscript 'T' shows the transpose. $\vec{\boldsymbol{D}}$, $\vec{\boldsymbol{P}}$ and $\boldsymbol{m}$ represent the diattenuator vector, polarizance vector, and a 3 x3 sub-matrix of $\boldsymbol{M}$ obtained by neglecting the first row and first column of $\boldsymbol{M}$. The minimum and maximum transmittances T_{min} and T_{max} of the diattenuator are important for finding the diattenuator axis and can be given as

$$T_{min}^{max} = m_{00} \pm \sqrt{m_{01}^2 + m_{02}^2 + m_{03}^2} \tag{2-38}$$

where the negative and positive signs correspond to the minimum and maximum transmittance of the diattenuator, respectively.

The diattenuation vector can be expressed as

$$\vec{\boldsymbol{D}} = \frac{1}{m_{00}} \begin{bmatrix} m_{01} \\ m_{02} \\ m_{03} \end{bmatrix} \tag{2-39}$$

Further, the magnitude of diattenuation vector can be mathematically given as

$$D = \frac{T_{max} - T_{min}}{T_{max} + T_{min}} = \frac{1}{m_{00}} \sqrt{m_{01}^2 + m_{02}^2 + m_{03}^2} \tag{2-40}$$

The total, linear and circular diattenuation are defined respectively as

$$D_T = \frac{1}{m_{00}} \sqrt{m_{01}^2 + m_{02}^2 + m_{03}^2} \tag{2-41}$$

$$D_L = \frac{1}{m_{00}} \sqrt{m_{01}^2 + m_{02}^2} \tag{2-42}$$

$$D_C = \frac{m_{03}}{m_{00}} \tag{2-43}$$

Generally, the diattenuator Mueller matrix $\boldsymbol{M_D}$ can be represented in the following symmetric form

$$\boldsymbol{M_D} = \begin{bmatrix} 1 & \vec{\boldsymbol{D}}^{\boldsymbol{T}} \\ \vec{\boldsymbol{D}} & \boldsymbol{m_D} \end{bmatrix} \tag{2-44}$$

where $\boldsymbol{m_D}$ is a 3x3 sub-matrix that can be determined from the diattenuation vector $\vec{\boldsymbol{D}}$ (Equation (2-39)) as

$$\boldsymbol{m_D} = \sqrt{1 - D^2}I + \left(1 - \sqrt{1 - D^2}\right)\hat{D}\hat{D}^T \tag{2-45}$$

where $\hat{\boldsymbol{D}}$ is the unit vector of $\vec{\boldsymbol{D}}$ and $\boldsymbol{I}$ is the identity matrix.

Similar to diattenuator, the polarizance vector $\vec{\boldsymbol{P}}$ can be defined from the first column of the $\boldsymbol{M}$, as given

$$\vec{\boldsymbol{P}} = \frac{1}{m_{00}} \begin{bmatrix} m_{10} \\ m_{20} \\ m_{30} \end{bmatrix} \tag{2-46}$$

The total, linear and circular polarizance are defined respectively as

$$P_T = \frac{1}{m_{00}} \sqrt{m_{10}^2 + m_{20}^2 + m_{30}^2} \tag{2-47}$$

$$P_L = \frac{1}{m_{00}} \sqrt{m_{10}^2 + m_{20}^2} \tag{2-48}$$

$$P_C = \frac{m_{30}}{m_{00}} \tag{2-49}$$

2.9.2 Retardance

Retardance, the second non-depolarizing polarization metric is defined as the phase shift between the two orthogonal components of $\boldsymbol{E}\,(\boldsymbol{z}, \boldsymbol{t})$ vector resulting from interaction of the electromagnetic waves with the medium. Typically, the Mueller matrix of a retarder can be written as

$$\boldsymbol{M_R} = \begin{bmatrix} 1 & \vec{\boldsymbol{0}}^T \\ \vec{\boldsymbol{0}} & \boldsymbol{m_R} \end{bmatrix} \tag{2-50}$$

where $\boldsymbol{m_R}$ is a 3 x 3 sub-matrix of $\boldsymbol{M_R}$ obtained by omitting the first row and first column of $\boldsymbol{M_R}$and $\vec{\mathbf{0}}$ is a 3x1 null vector. It may be noted that the elements of $\boldsymbol{m_R}$ can be found using the following relation

$$(m_R)_{ij} = \delta_{ij} \cos R + a_i a_j (1 - \cos R) + \sum_{k=1}^{3} \epsilon_{ijk} \sin R \; ; \; i,j = 1,2,3 \qquad (2\text{-}51)$$

From the Mueller matrix of retarder $\boldsymbol{M_R}$ (Equation (2-50)), the magnitude of retardance vector $\vec{\boldsymbol{R}}$ and the direction of its fast axis can be given as

$$R = \cos^{-1}\left[\frac{tr(M_R)}{2} - 1\right] \qquad (2\text{-}52)$$

$$a_i = \frac{1}{2 \sin R} \sum_{j,k=1}^{3} \epsilon_{ijk} (m_R)_{jk} \qquad (2\text{-}53)$$

where ϵ_{ijk} represent the Levi-Civita tensor.

2.10 Decomposition of Non-depolarizing Mueller Matrices

The step by step decomposition of Mueller matrix **M** for non-depolarizing medium ($\boldsymbol{M_\Delta} = 0$) can be described as;

- Decompose the Mueller matrix **M** as the product of the diattenuator matrix $\boldsymbol{M_D}$ followed by the retarder matrix $\boldsymbol{M_R}$ as given below

$$\boldsymbol{M} = \boldsymbol{M_D M_R} \qquad (2\text{-}54)$$

- Find the diattenuation vector $\vec{\mathbf{D}}$ directly from Mueller matrix **M** with the help of Equation (2-39).
- Find the Mueller matrix of diattenuator $\boldsymbol{M_D}$ with the help of Equations (2-39) and (2-45). Further, the singularity of diattenuator Mueller matrix (i.e. $det(\boldsymbol{M_D}) = 0$) should be determined.
- For non-singular $\boldsymbol{M_D}$ (i.e. $det(\boldsymbol{M_D}) \neq 0$), the Mueller matrix of retarder $\boldsymbol{M_R}$ can be determined as

$$\boldsymbol{M_R} = \boldsymbol{M_D^{-1}M} \tag{2-55}$$

- For singular $\boldsymbol{M_D}$, the possible solutions for the Mueller matrix of retarder $\boldsymbol{M_R}$ are infinite and the minimum retardance principle is applicable so that the solution with minimum retardance value is selected.

2.11 Decomposition of Depolarizing Mueller Matrices

For a depolarizing medium, the third basis matrix (i.e. $\boldsymbol{M_\Delta}$) is non-zero and has to be considered in the decomposition algorithm. For a medium with no diattenuation and retardance, the only polarimetric parameter would be the depolarization which can be expressed by the following depolarizer Mueller matrix $\boldsymbol{M}_\Delta$

$$\boldsymbol{M}_\Delta = \begin{bmatrix} 1 & 0 & 0 & 0 \\ 0 & a & 0 & 0 \\ 0 & 0 & b & 0 \\ 0 & 0 & 0 & c \end{bmatrix} \tag{2-56}$$

where a, b and c are the diagonal elements of the $\boldsymbol{M}_\Delta$ and are correlated to the principal depolarization factors by the following relations

$$\Delta_1 = 1 - |a| \tag{2-57}$$

$$\Delta_2 = 1 - |b| \tag{2-58}$$

$$\Delta_3 = 1 - |c| \tag{2-59}$$

where Δ_1, Δ_2 and Δ_3 are the principal depolarization factors that describe the depolarization effects along the principal axes of the depolarizer. Further, the overall depolarization power Δ of depolarizer is expressed as

$$\Delta = \frac{\Delta_1 + \Delta_2 + \Delta_3}{3} = 1 - \frac{|a| + |b| + |c|}{3} \tag{2-60}$$

It may be noted that a depolarizer may exhibit the polarizance; such situations are not properly descried by the depolarizer diagonal matrix $\boldsymbol{M}_\Delta$ (Equation (2-56)). Since the polarizance details are encoded in the first column of the Mueller matrix, therefore, the depolarizer matrix with polarizance can be given as

$$\boldsymbol{M}_{\Delta} = \begin{bmatrix} 1 & \vec{\boldsymbol{0}}^{\boldsymbol{T}} \\ \vec{\boldsymbol{P}}_{\Delta} & \boldsymbol{m}_{\Delta} \end{bmatrix} \tag{2-61}$$

where $\boldsymbol{m}_{\Delta}$ is the 3x3 symmetric matrix (from Equation (2-56)) and $\vec{\boldsymbol{P}}_{\Delta}$ is the polarizance vector that can be given as

$$\vec{\boldsymbol{P}}_{\Delta} = \frac{\vec{\boldsymbol{P}} - m\,\vec{\boldsymbol{D}}}{1 - D^2} \tag{2-62}$$

where $\boldsymbol{m}$ is the 3x3 matrix from Equation (2-37).

Now considering the depolarizing medium, the Mueller matrix $\boldsymbol{M}$ of the sample is expressed as the product of three component matrices, as given by Equation (2-35). The decomposition is started by extracting the diattenuation matrix $\boldsymbol{M_D}$ from the full Mueller matrix $\boldsymbol{M}$ such that

$$\boldsymbol{M}' = \boldsymbol{M}\boldsymbol{M}_{\boldsymbol{D}}^{-\boldsymbol{1}} \tag{2-63}$$

where the intermediate Mueller matrix $\boldsymbol{M}'$ is free from diattenuation effects and contains only the retardance and depolarization effects. It may be noted that we have assumed that the diattenuator matrix $\boldsymbol{M_D}$ is non-singular (i.e. $det(\boldsymbol{M_D}) \neq 0$).

We can further decompose the matrix $\boldsymbol{M}'$ into a retarder matrix $\boldsymbol{M_R}$ followed by a depolarizer matrix $\boldsymbol{M}_{\Delta}$ as follows

$$\boldsymbol{M}' = \boldsymbol{M}_{\Delta}\boldsymbol{M_R} = \begin{bmatrix} 1 & \vec{\boldsymbol{0}}^{\boldsymbol{T}} \\ \vec{\boldsymbol{P}}_{\Delta} & \boldsymbol{m}_{\Delta} \end{bmatrix} \begin{bmatrix} 1 & \vec{\boldsymbol{0}}^{\boldsymbol{T}} \\ \vec{\boldsymbol{0}} & \boldsymbol{m_R} \end{bmatrix} = \begin{bmatrix} 1 & \vec{\boldsymbol{0}}^{\boldsymbol{T}} \\ \vec{\boldsymbol{P}}_{\Delta} & \boldsymbol{m}_{\Delta}\boldsymbol{m_R} \end{bmatrix} = \begin{bmatrix} 1 & \vec{\boldsymbol{0}}^{\boldsymbol{T}} \\ \vec{\boldsymbol{P}}_{\Delta} & \boldsymbol{m}' \end{bmatrix} \tag{2-64}$$

where the sub-matrix $\boldsymbol{m}'$ of the intermediate matrix $\boldsymbol{M}'$ can be written as

$$\boldsymbol{m}' = \boldsymbol{m}_{\Delta}\boldsymbol{m_R} \tag{2-65}$$

It may be noted that $\boldsymbol{m}_{\Delta}$ can be found as

$$\begin{aligned} \boldsymbol{m}_{\Delta} = \kappa\big[m'(m')^T + \big(\sqrt{\lambda_1\lambda_2} + \sqrt{\lambda_2\lambda_3} + \sqrt{\lambda_3\lambda_1}\big)\boldsymbol{I}\big]^{-1} \\ \times \big[\big(\sqrt{\lambda_1} + \sqrt{\lambda_2} + \sqrt{\lambda_3}\big)m'(m')^T + \sqrt{\lambda_1\lambda_2\lambda_3}\;\boldsymbol{I}\big] \end{aligned} \tag{2-66}$$

where λ_1 , λ_2 and λ_3 are the eigen values of the matrix $\boldsymbol{m'(m')^T}$, $\boldsymbol{I}$ is a 3x3 identity matrix and κ=$\pm$1; for $det(\boldsymbol{m'}) = -ve$, then $\kappa = -1$ and vice versa.

With $\boldsymbol{m_\Delta}$ in hand, $\boldsymbol{m_R}$ can be found using Equation. (2-65) as

$$\boldsymbol{m_R} = \boldsymbol{m_\Delta}^{-1}\boldsymbol{m'} \tag{2-67}$$

Finally, using Equations (2-50) and (2-61), the retardance matrix $\boldsymbol{M_R}$ and the depolarizer matrix $\boldsymbol{M_\Delta}$ can be found, respectively.

For the situation where the Mueller matrix of diattenuator is singular (i.e. $det(\boldsymbol{M_D})$ = 0), the sub-matrix $\boldsymbol{m'}$ will also be singular. For this case, singular value decomposition is applied to $\boldsymbol{m'}$ as follows

$$\boldsymbol{m'} = \boldsymbol{V\mathcal{D}U^T} \tag{2-68}$$

where $\boldsymbol{V}$ represent a unitary matrix, the diagonal matrix $\boldsymbol{\mathcal{D}}$ have non-negative real numbers, and $\boldsymbol{U^T}$ is the conjugate transpose of $\boldsymbol{V}$. Equation (2-68) can also be written as

$$\boldsymbol{m'} = (\hat{v}_1\ \hat{v}_2\ \hat{v}_3)\ diag\left(\sqrt{\lambda_1}, \sqrt{\lambda_2}, \sqrt{\lambda_3}\right)(\hat{u}_1\ \hat{u}_2\ \hat{u}_3) \tag{2-69}$$

where $\hat{v}_i$ and $\hat{u}_i$ with $i = 1,2,3$ denotes columns of $\boldsymbol{V}$ and $\boldsymbol{U}$, respectively.

From Equation (2-69), it can be shown that

$$\boldsymbol{m_\Delta} = \pm\left(\sqrt{\lambda_1}\hat{v}_1\hat{v}_1^T + \sqrt{\lambda_2}\hat{v}_2\hat{v}_2^T + \sqrt{\lambda_3}\hat{v}_3\hat{v}_3^T\right) \tag{2-70}$$

$$\boldsymbol{m_R} = \pm\left(\hat{v}_1\hat{u}_1^T + \hat{v}_2\hat{u}_2^T + \hat{v}_3\hat{u}_3^T\right) \tag{2-71}$$

The following three cases are considered for singular $\boldsymbol{m'}$;

a. If all eigen values of $\boldsymbol{m'}$are zero (i.e. $\lambda_1 = \lambda_2 = \lambda_3 = 0$), the depolarizer matrix $\boldsymbol{M_\Delta}$ and retarder matrix $\boldsymbol{M_R}$simply becomes

$$\boldsymbol{M_\Delta} = \begin{bmatrix} 1 & \vec{\boldsymbol{0}}^{\boldsymbol{T}} \\ \vec{\boldsymbol{P}}_\Delta & 0 \end{bmatrix} \ and\ \ \boldsymbol{M_R} = \boldsymbol{I} \tag{2-72}$$

b. For $\lambda_1 \neq 0$ and $\lambda_2 = \lambda_3 = 0$, $\boldsymbol{m'}$can be given as

$$\boldsymbol{m}' = \sqrt{\lambda_1}\hat{v}\,\hat{u}^T = \left(\sqrt{\lambda_1}\hat{v}\,\hat{v}^T\right)\boldsymbol{m_R} \tag{2-73}$$

Such that

$$\boldsymbol{m}_\Delta = \sqrt{\lambda_1}\hat{v}\,\hat{v}^T = \frac{\boldsymbol{m}'\,(\boldsymbol{m}')^T}{\sqrt{tr\{\boldsymbol{m}'\,(\boldsymbol{m}')^T\}}} \tag{2-74}$$

In this case minimum value of retardance magnitude is given as

$$R = \cos^{-1}\left[\frac{\boldsymbol{m}'\,(\boldsymbol{m}')^T}{\sqrt{tr\{\boldsymbol{m}'\,(\boldsymbol{m}')^T\}}}\right] \tag{2-75}$$

c. Finally consider the case in which $\lambda_3 = 0$ and other eigen values are non-zero, then

$$\boldsymbol{m}_\Delta = \left(\sqrt{\lambda_1} + \sqrt{\lambda_2}\right)\left[\boldsymbol{m}'(\boldsymbol{m}')^T + \sqrt{\lambda_1\lambda_2}\,\boldsymbol{I}\right]^{-1}\boldsymbol{m}'(\boldsymbol{m}')^T \tag{2-76}$$

also

$$\boldsymbol{m_R} = \hat{v}_1\hat{u}_1^T + \hat{v}_2\hat{u}_2^T + \frac{\hat{v}_1 \times \hat{v}_1}{|\hat{v}_1 \times \hat{v}_1|} + \frac{(\hat{u}_1 \times \hat{u}_2)^T}{|\hat{u}_1 \times \hat{u}_2|} \tag{2-77}$$

2.12 Physical Polarimetric Properties

The polar decomposition of Mueller matrix $\boldsymbol{M}$ enables to study the 16 polarimetric properties of the interrogated sample individually. These properties that provide the fingerprint of the probed sample are discussed below;

2.12.1 Diattenuation

The Mueller matrix of diattenuator $\boldsymbol{M_D}$ contains four different polarimetric properties and is said to have four degrees of freedom, which are given as

- Unpolarized total transmittance is directly extracted from the first element m_{00} of the Mueller matrix $\boldsymbol{M}$.
- The magnitude of diattenuation D can be obtained by using Equation (2-40).
- The diattenuation ellipticity is obtained by using the following relation

$$\varepsilon_D = \frac{1}{2}\sin^{-1}\left[\frac{S_{D3}}{S_{D1}}\right] \quad (2\text{-}78)$$

- The diattenuation azimuth is obtained as

$$\varphi_D = \tan^{-1}\left[\frac{S_{D3}}{S_{D2}}\right] \quad (2\text{-}79)$$

where the subscript D indicates diattenuation, and $S_{D1}. S_{D2}$ and S_{D3} are the Stoke vectors related to the diattenuation vector D_1, D_2 and D_3, respectively.

2.12.2 Retardance

The Mueller matrix of retarder $\boldsymbol{M_R}$ contains three different polarimetric properties and is said to have three degrees of freedom, which are given as

- The magnitude of retardance of the probed sample can be determined using Equation (2-52).
- The retardance ellipticity can be determined as

$$\varepsilon_R = \frac{1}{2}\sin^{-1}\left[\frac{S_{R3}}{S_{R1}}\right] \quad (2\text{-}80)$$

- The retardance azimuth can be found as

$$\varphi_R = \tan^{-1}\left[\frac{S_{R3}}{S_{R2}}\right] \quad (2\text{-}81)$$

where the subscript R indicates retardance and $S_{R1}. S_{R2}$ and S_{R3} are the Stoke vectors related to the retardance vector R_1, R_2 and R_3, respectively.

2.12.3 Depolarization

The Mueller matrix of depolarizer $\boldsymbol{M_\Delta}$ contains nine different polarimetric properties and is said to have nine degrees of freedom. Specifically, three degrees of freedom are related to the polarizance; the magnitude of polarizance P_Δ, the polarizance ellipticity ε_Δ and the

polarizance azimuth φ_{Δ}. The remaining six degrees of freedom are correlated to the three orthogonal axes of depolarization described by ($\overrightarrow{V_1}$, $\overrightarrow{V_2}$, $\overrightarrow{V_3}$) and their associated eigen values (Δ_1 , Δ_2 , Δ_3). Figure 2-3 schematically illustrates the 16 polarimetric parameters extracted with the help of polar decomposition.

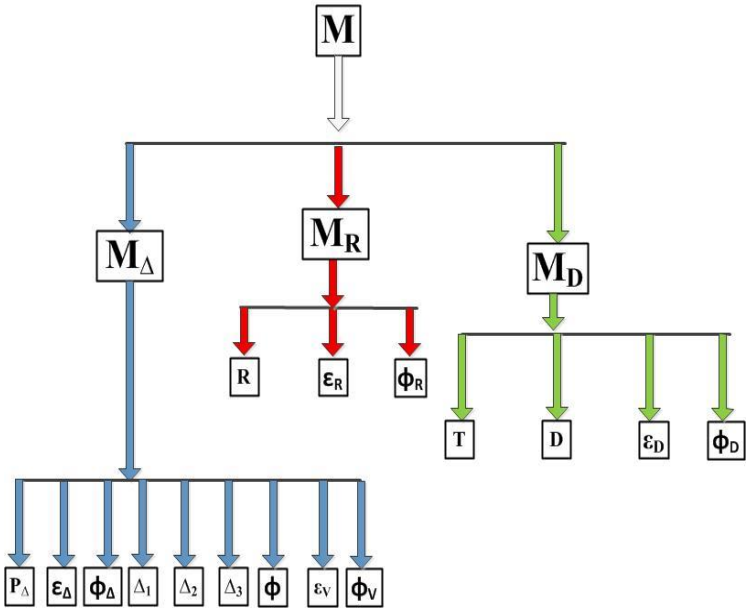

Figure 2-3 Schematic of polar decomposition of Mueller matrix *M* into its basis matrices and the subsequent sixteen polarimetric properties.

2.12.4 Optical Activity

The interaction of polarized light with chiral medium is of great interest in the sense that such medium rotates the plane of polarization of incident light; a phenomenon known as optical activity. It may be noted that chirality is the property of molecules with identical composition and non-superimposable mirror image configuration (handedness). Linear retardance and linear diattenuation also contribute to the inherent optical rotation of the biological tissues. However, the optical activity caused by circular retardance only can be decoupled with the help of polar decomposition.

First, the Mueller matrix of retarder $\boldsymbol{M_R}$ is determined using polar decomposition, as discussed earlier. The matrix $\boldsymbol{M_R}$ is further decomposed as $\boldsymbol{M_R = M_{LR} \bullet M_{\phi}}$ where $\boldsymbol{M_{LR}}$ and $\boldsymbol{M_{\phi}}$ contains the effects of linear and circular retardance, respectively, as given below

$$\boldsymbol{M_R} = \boldsymbol{M_{LR}} \bullet \boldsymbol{M_{\phi}} \tag{2-82}$$

$$\boldsymbol{M_R} = \begin{bmatrix} 1 & 0 & 0 & 0 \\ 0 & cos^2 2\gamma + sin^2 2\gamma\, cos\alpha & sin2\gamma\, cos2\gamma(1-cos\alpha) & -sin2\gamma \sin\alpha \\ 0 & sin2\gamma\, cos2\gamma(1-cos\alpha) & cos^2 2\gamma + sin^2 2\gamma\, cos\alpha & cos2\gamma \sin\alpha \\ 0 & sin\, 2\gamma \sin\alpha & -cos2\gamma \sin\alpha & \cos\alpha \end{bmatrix}$$

$$X \begin{bmatrix} 1 & 0 & 0 & 0 \\ 0 & \cos 2\beta & \sin 2\beta & 0 \\ 0 & -\sin 2\beta & \cos 2\beta & 0 \\ 0 & 0 & 0 & 1 \end{bmatrix} \tag{2-83}$$

where α , β and γ represents the linear retardance, circular retardance and the direction of the fast axis, respectively. After simple algebra, the trace tr of retardance Mueller matrix $\boldsymbol{M_R}$ (from Equation ((2-80)) can be expressed as

$$tr(\boldsymbol{M_R}) = 1 + \cos 2\beta(1 + \cos\alpha) + \cos\delta \tag{2-84}$$

The total retardance magnitude R can be determined by putting Equation (2-84) in Equation (2-52) and then using basic trigonometric identities. The resultant relation is

$$R = \cos^{-1}[2\cos^2\beta\cos^2(\alpha/2)] \tag{2-85}$$

Putting Equation (2-85) in Equation (2-53) and then simplifying for a_3 gives

$$a_3 = \sqrt{\frac{\sin^2\beta\cos^2(\alpha/2)}{1-\cos^2\beta\cos^2(\alpha/2)}} \tag{2-86}$$

Solving Equation (2-84) and (2-86) for linear retardance α and optical rotation β gives the following relations

$$\alpha = 2\cos^{-1}\left\{\sqrt{a_3^2(1-\cos^2(R/2)) + \cos^2(R/2)}\right\} \tag{2-87}$$

$$\beta = \cos^{-1}\left\{\frac{\cos(R/2)}{\cos(\alpha/2)}\right\} \tag{2-88}$$

2.13 Summary

This chapter has been devoted to an overview of silent features of polarized light followed by its interaction with turbid medium. Basic mathematical formalism for light polarization such as Stokes vector, coherency matrix and Jones vector are presented. Detailed discussion focused on the interaction of polarized light with biological tissues with special emphasis on Stokes-Mueller formalism is provided, enabling a better understanding of the presented experimental results in the following sections. Extraction of individual polarimetric properties from the experimentally measured Mueller matrix is also discussed. Specifically, detailed outline of polar decomposition is provided.

3 Experimental Techniques

3.1 Introduction

Experimental techniques employed for the polarimetric characterization of samples are discussed in this chapter. Specifically, the point measurement procedure of Mueller matrix polarimeter which is capable of scanning the biological tissues over the complete visible spectral range, its calibration and methodology for biological tissue characterization has been described. Subsequently, Mueller matrix imaging polarimeter and its working principle for the experimental measurement of Mueller matrix has been given. Radiofrequency generator for creating ablation lesions in the myocardial tissue is also described. Afterwards, details of sample preparation for both point and imaging measurement setups are presented. Finally, some statistics used in the polarimetric data analyses are given at the end.

3.2 Mueller Matrix Polarimeter for Point Measurements

Computer controlled Mueller matrix polarimeter (Axometrics, Huntsville, USA) was employed for the polarimetric characterization of various biological tissues. This polarimetric system is controlled by the dedicated software "AxoScanTM" and is capable of point measurements over the complete spectral range. The simple schematic of this polarimeter is shown in Figure 3-1. The probing light for exposing the inherent details of sample's polarimetric signatures is provided by a 150 W xenon lamp (400–800 nm) to the polarization state generator (PSG), which sequentially establishes the desired input Stocks vector of the probing light. The light signal from source to PSG is delivered via optic fiber (200 μm diameter). The tissue samples were illuminated in the wavelength range of 460-800 nm (20 nm step) selected with a built-in diffraction grating monochromator. The beam spot size at the sample was 5 mm. Finally, the polarization

state analyzer (PSA) quantifies the polarization state of the probing light after interacting with the sample.

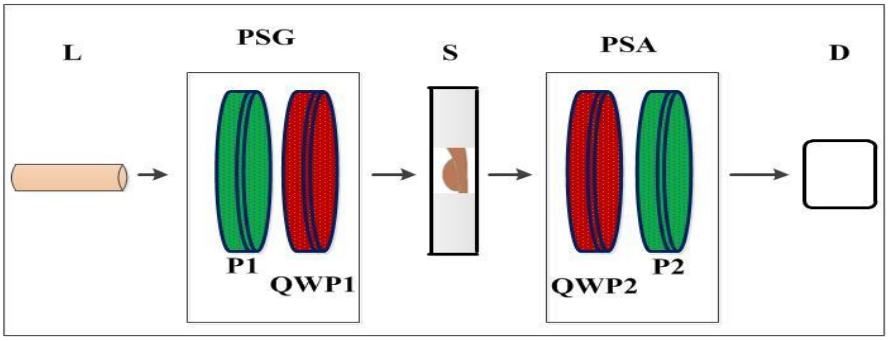

Figure 3-1 Schematic of Mueller matrix polarimeter used for polarimetric investigation of normal and BCC skin tissues. L: light source, PSG: polarization state generator, S: sample, PSA: polarization state analyzer, D: detector.

The heart of the Mueller matrix polarimeter for point measurement is the PSG and PSA, both placed on the adjustment bracket in such a way to guide the probing optical beam on the desired path for sample (tissue) illumination. PSG sequentially generate

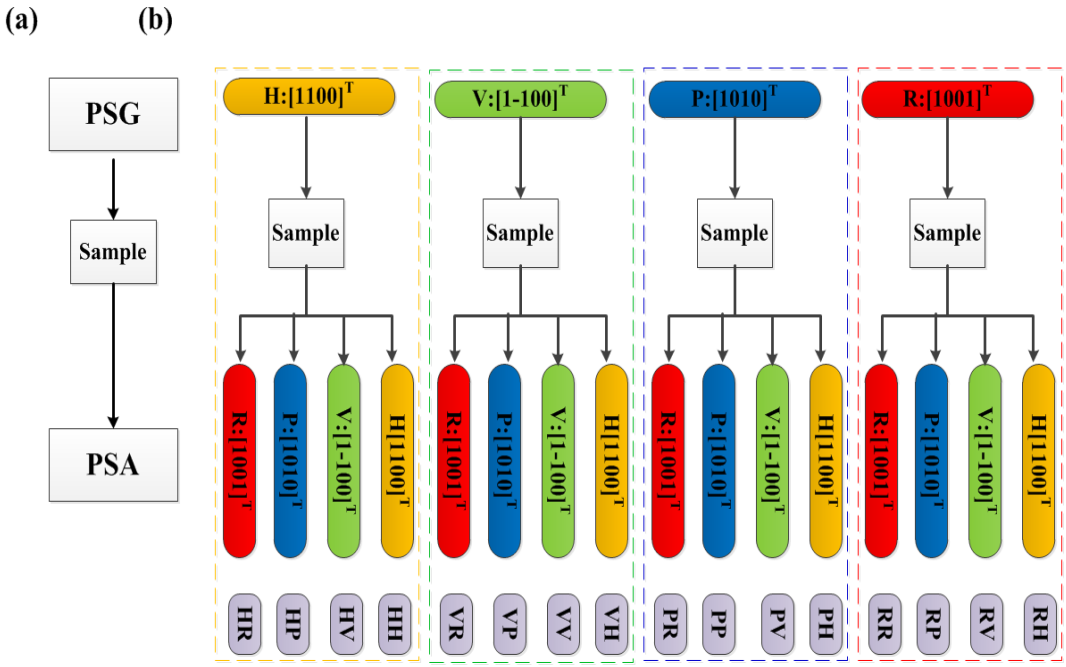

Figure 3-2 (a) experimental layout and (b) sixteen combinations of generated and analyzed polarization states. H: horizontal polarization, V: vertical polarization, P: linear +45^{o} polarization, and R: right circular polarization.

various polarization states which interact with the sample and are subsequently analyzed by PSA. In this study, all tissue samples were illuminated with four different input polarization states (linear horizontal H, linear vertical V, linear +45^o P, and right circular R); each polarization state was analyzed on four different polarization states (same as input states) such that a total of sixteen combinations were obtained as depicted in Figure 3-2. Specifically, the input-output states combinations measured were: HH, HV, HP, HR, VH, VV, VP, VR, PH, PV, PP, PR, RH, RV, RP, and RR. Here the first letter indicates the incident polarization state while the second letter denotes the analyzed output state. For instance "VH" indicates that the incident polarization state on the sample is vertical (V), which is analyzed after interaction onto horizontal (H) polarized state. These 16 intensity measurements were used to construct the Mueller matrix of the probed sample, as given below [97]

$$\boldsymbol{M} = \begin{bmatrix} m_{00} & m_{01} & m_{02} & m_{03} \\ m_{10} & m_{11} & m_{12} & m_{13} \\ m_{20} & m_{21} & m_{22} & m_{23} \\ m_{30} & m_{31} & m_{32} & m_{33} \end{bmatrix} \tag{3-1}$$

$$= \begin{bmatrix} HH+HV+VH+VV & HH+HV-VH-VV & 2(PH+PV)-m_{11} & 2(RH+RV)-m_{11} \\ HH-HV+VH-VV & HH-HV-VH+VV & 2(PH-VP)-m_{11} & 2(RH-RV)-m_{11} \\ 2(HP+VP) & 2(HP-VP) & 2(2PP-PH-PV)-m_{11} & 2(2RP-RH-RV)-m_{11} \\ 2(HR+VR) & 2(HR-VR) & 2(PR-PH-PV)-m_{11} & 2(RR-HR-RV)-m_{11} \end{bmatrix} \tag{3-2}$$

It is noteworthy that the light delivered by optical fiber to PSG is first collimated by an internally implanted collimating lens. The collimated light beam subsequently passes through a polarizer and waveplate, coupled to high speed motors enabling them to rotate at high speed. This feature facilitates different alignment combinations of polarizer and waveplate for generating various input polarization states, which eventually illuminate the sample. After interaction, the output light beam is collected by PSA; a combination of waveplate and polarizer. Finally, the light beam is focused on the computer coupled detector (acceptance angle ~ ± 2°) with the help of a lens. The proper alignment of PSG and PSA is important as any discrepancy would result in reduction of measurement accuracy. Photograph of MMSP along with each component is in shown in Figure 3-3. All operations of the polarimeter such as selection of a particular wavelength

or spectrum, generation of desired polarization state(s), acquisition and analyses of the data are controlled by the control unit with the help of AxoScanTM software package.

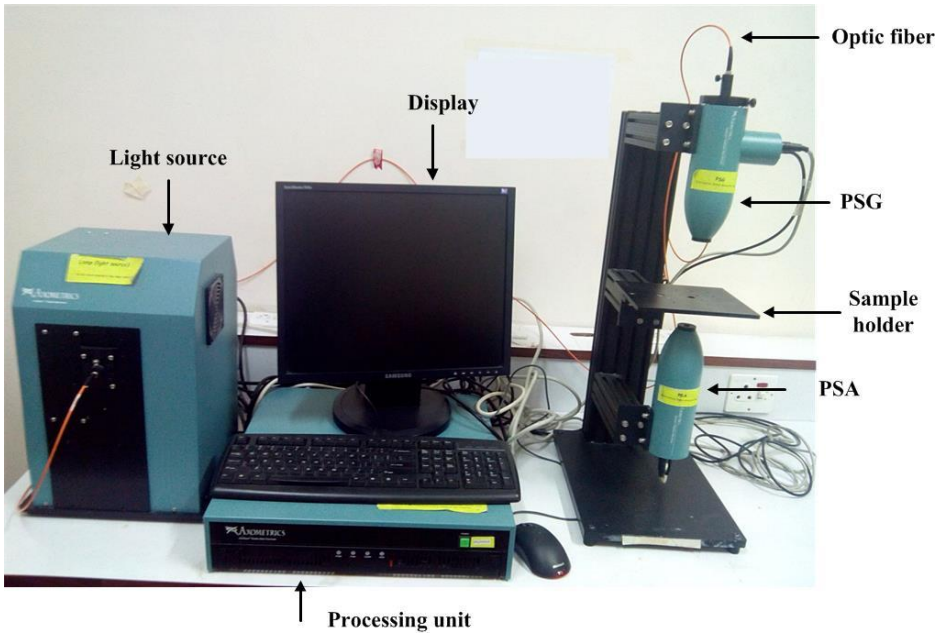

Figure 3-3 White light photograph of Mueller matrix point measurement system.

3.3 Accuracy of the Polarimeter

The accuracy and reproducibility of the Mueller matrix polarimeter for point measurements has been assessed and validated by using the standard optical elements such as linear polarizer and quarter waveplate (for 633nm wavelength) of known polarization properties. These standard optical elements were analyzed over the complete visible spectral range (400-800 nm). It is noteworthy that transmission geometry for the point measurement system has been used to acquire all data presented in this study. Mueller matrix for each standard sample was measured and then decomposed via polar decomposition method to extract the corresponding polarization properties.

Total and linear diattenuation of the linear polarizer studied for the validation of the system is presented in Figure 3-4. Analyses of the data demonstrate that the error in both total and linear diattenuation decreases with wavelength as indicated by the error bars (i.e. one standard deviation). It may also be noted that the error bars for most data

points are smaller than the symbols used in Figure 3-4 and therefore not visible. A maximum 1.1% error exists in the calculation of both total and linear diattenuation. The small error and almost no fluctuations in the standard sample of polarizer validate the excellent performance of the Mueller matrix polarimetric system for point measurement and the decomposition algorithms. From Figure 3-5, it is evident that the total and liner diattenuation for the polarizer is almost unity over entire investigated wavelength. Further, it may be elucidated that the circular diattenuation is nearly zero, as expected.

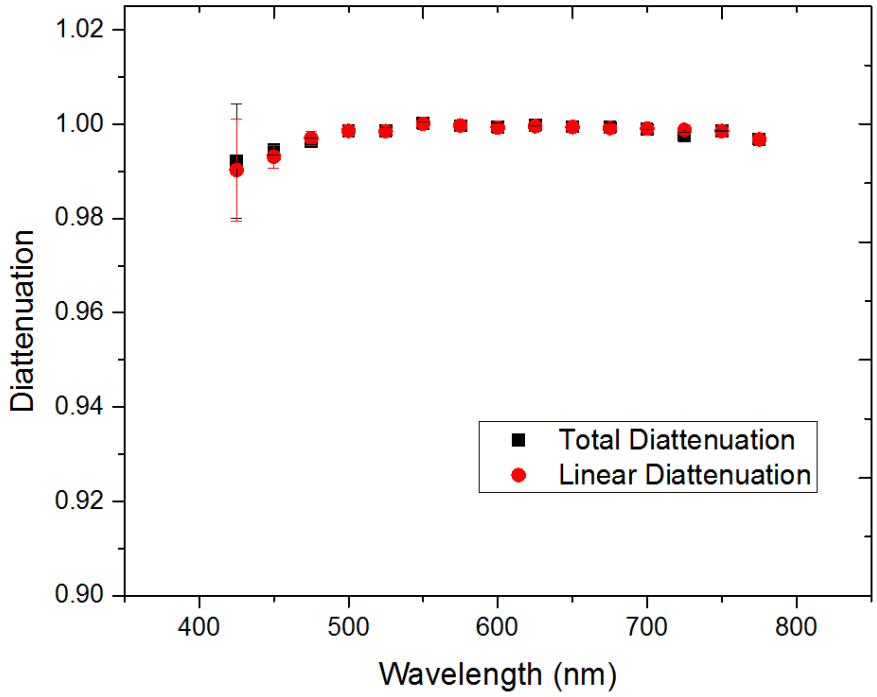

Figure 3-4 Total and linear diattenuation of linear polarizer in the spectral range from 400 to 800 nm.

The second standard optical element used for the validation of the polarimetric point measurement system was a waveplate (commonly known as retarder) which offer phase retardance of 90^{o} at the wavelength of 633 nm. Mueller matrix for the retarder was measured in the transmission mode over the entire visible spectral range (400-800 nm). Polar decomposition was used to decode the experimental Mueller matrix and extract the individual parameters such as total and linear retardance. These results are shown in Figure 3-5. The maximum error noted in the retardance measurement is 1.1 %. Similar to polarizer measurement, the error bars are smaller than the symbols used and consequently

not visible. From Figure 3-5, it may be noted that the waveplate used for the system validation offer 90^{o} phase retardance at the wavelength of 633 nm. These measurements indicate the stability and reproducibility of the Mueller matrix polarimeter.

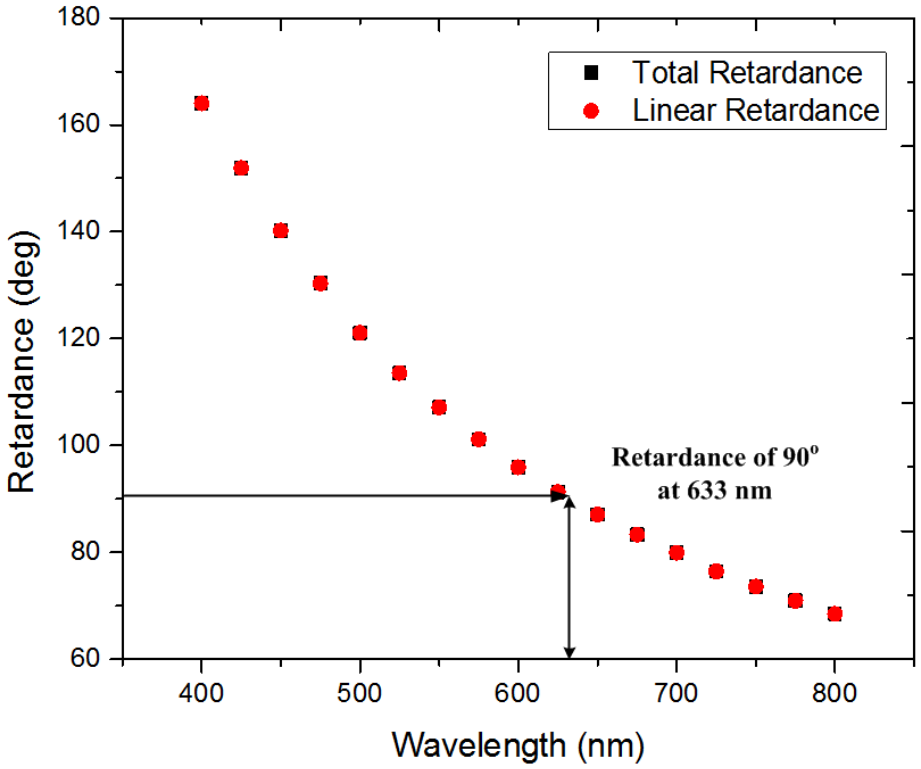

Figure 3-5 Total and linear retardance of retarder plate in the spectral range from 400 to 800 nm. The retarder plate behaves as a quarter wave plate at 633nm.

3.4 Mueller Matrix Imaging Polarimeter

All biological tissues were characterized using polarized light imaging in the backscattered geometry, 25^{o} off the retro-reflection direction. Figure 3-6 illustrate the photograph of the experimental setup and the schematic diagram for the Mueller matrix imaging polarimeter employed in this study. The magnified area shown in the polarimetric imaging setup (left bottom corner, Figure 3-6a) illustrates a myocardial tissue sample with radiofrequency (RF) ablation lesion illuminated in the sample holder. The input polarized light from the PSG is incident on the sample and eventually registered by the detector (i.e. CCD camera) after passing through the PSA setup.

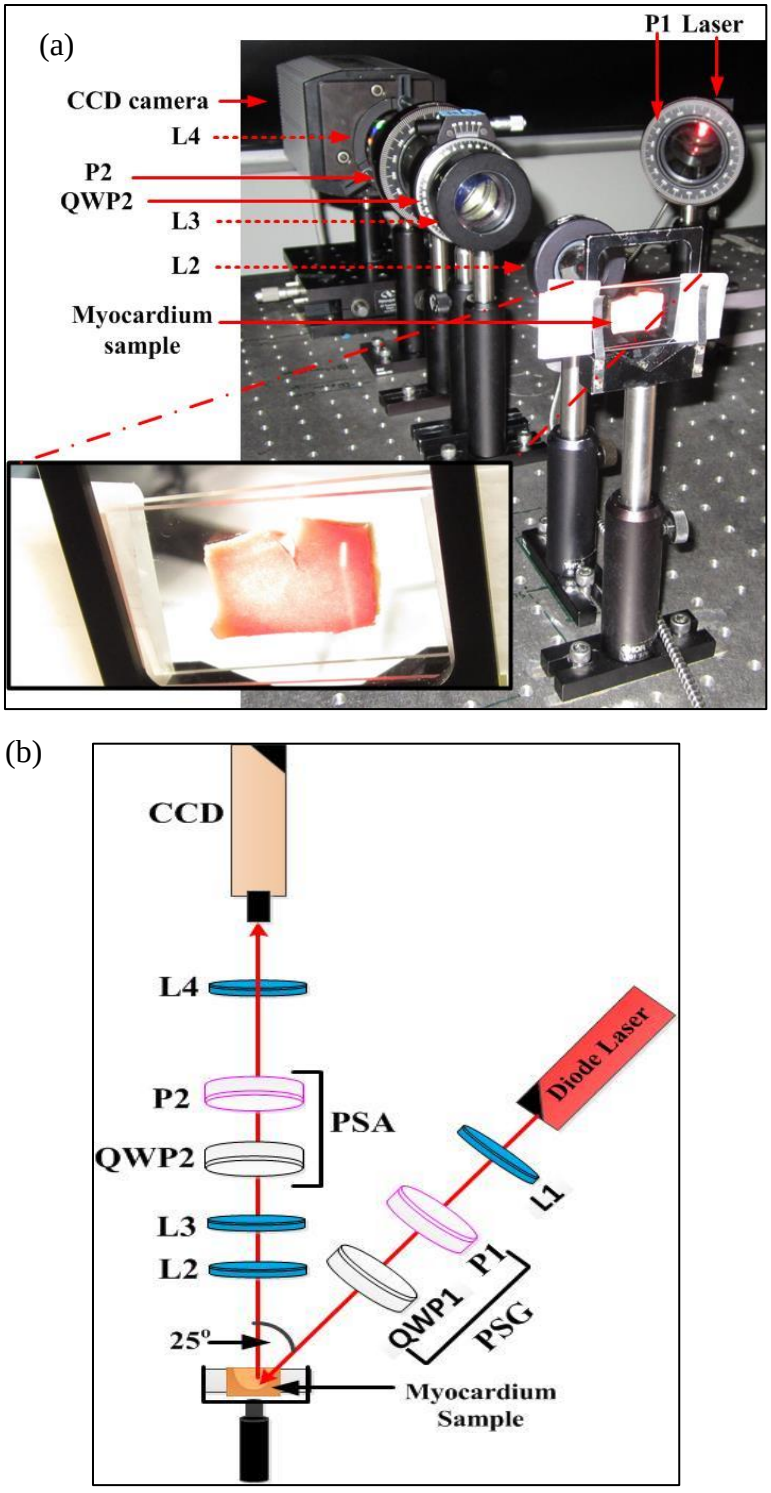

Figure 3-6 (a) White light photo of experimental Mueller matrix imaging setup. The magnified area shows an RF ablation sample illuminated in the sample holder. (b) Schematic of the experiment.

The biological tissue samples were sequentially illuminated by four different input Stokes vectors. These states were generated by passing the light from a 635nm diode laser (Thorlabs) through a polarization state generator (PSG), consisting of a polarizer P1, and quarter wave plate QWP1. The input Stokes vectors used were: linear horizontal H, linear vertical V, linear $+45^{o}$ P, and right circular R. After interaction with the sample, the scattered light passed through the polarization state analyzer (PSA) (quarter wave plate QWP2, followed by polarizer P2) and was detected with a CCD camera (CoolSnap K4, Photomerics). Each input state was analyzed with six different output Stokes vector arrangements in the PSA optics. Specifically, the measured output states were: linear horizontal H, linear vertical V, linear $+45^{o}$ P, linear -45^{o} B, right circular R, and left circular L. These PSG / PSA combinations resulted in 24 measurements which were subsequently used to calculate the tissue Mueller matrix $\boldsymbol{M}$, as shown in below [37].

$$\boldsymbol{M} = \frac{1}{4}\begin{bmatrix} HH+HV+VH+VV & HH+HV-VH-VV & 2(PH+PV)-4m_{11} & 2(RH+RV)-4m_{11} \\ HH-HV+VH-VV & HH-HV-VH+VV & 2(PH-PV)-4m_{21} & 2(RH-RV)-4m_{21} \\ HP-HB+VP-VB & HP-HB-VP+VB & 2(PP-PB)-4m_{31} & 2(RP-RB)-4m_{31} \\ HR-HL+VR-VL & HR-HL-HR+VL & 2(PR-PL)-4m_{41} & 2(RR-RL)-4m_{41} \end{bmatrix} \quad (3\text{-}3)$$

As mentioned earlier for the combination of the two letters, the first letter indicates the incident polarization state while the second letter denotes the analyzed output state. For instance "PH" indicates that the incident polarization state on the sample is linearly polarized at 45^{o} (P), which is analyzed after interaction onto horizontal (H) polarized state.

3.5 Sample Preparation

In this study, biological tissue samples from two different domains were assessed with the help of Mueller matrix polarimetry. Specifically, the Mueller matrix point measurement system was used for the characterization of healthy control vs. cancerous human tissue samples while the Mueller matrix imaging system was used for the evaluation of healthy control vs. radiofrequency ablated porcine myocardial tissue samples. Details of samples preparation for both studies are discussed below individually.

3.5.1 Cancerous Tissue Sample Preparation

To illustrate the possible polarimetric signatures of control healthy compared to basal cell carcinoma (BCC) of human skin, we collected 26 samples in each group from different patients. Both types of tissue samples were extracted from the patients with the help of biopsy. The BCC tissue samples (validated by histology) were collected from various anatomical skin positions such as nose, chest wall, lip, check, etc. of different patients. Clinically, these lesions were typically composed of a central ulcerated thickened skin with a rim of intact skin surrounding it. Those suspicious lesions referred by medical doctors/ dermatologists that turn to be normal on histopathology examination were included in the healthy group for this study. It is noteworthy that care was taken to include the completely uninvolved sections of such normal samples (validated by histology) in the healthy group. Although the subjects in the two groups were different; it was ensured that the corresponding normal and BCC tissue samples were collected from the same anatomical skin positions in both groups. This practice ruled out the difference in collagen type/ content and thickness of epidermis and dermis at various location of the body surface. Consent from all subjects was ensured before their tissue samples were included in the study. These samples were immediately fixed in 10% formalin and subsequently embedded in paraffin. Afterwards, the paraffin blocks were sliced in tissue samples of 4 μm thickness using Leica microtome. These samples were then pasted on glass slides, stained with hematoxylin and eosin (H&E) and covered with glass coverslip. It may be noted that the plastic cover slips were avoided due to their strong intrinsic retardance. These tissue slides were used sequentially for histopathological and polarimetry measurements. Microscopic images of some histological BCC slides are shown in Figure 3-7. The tissue samples were analyzed with the help of Mueller matrix polarimeter for point measurements.

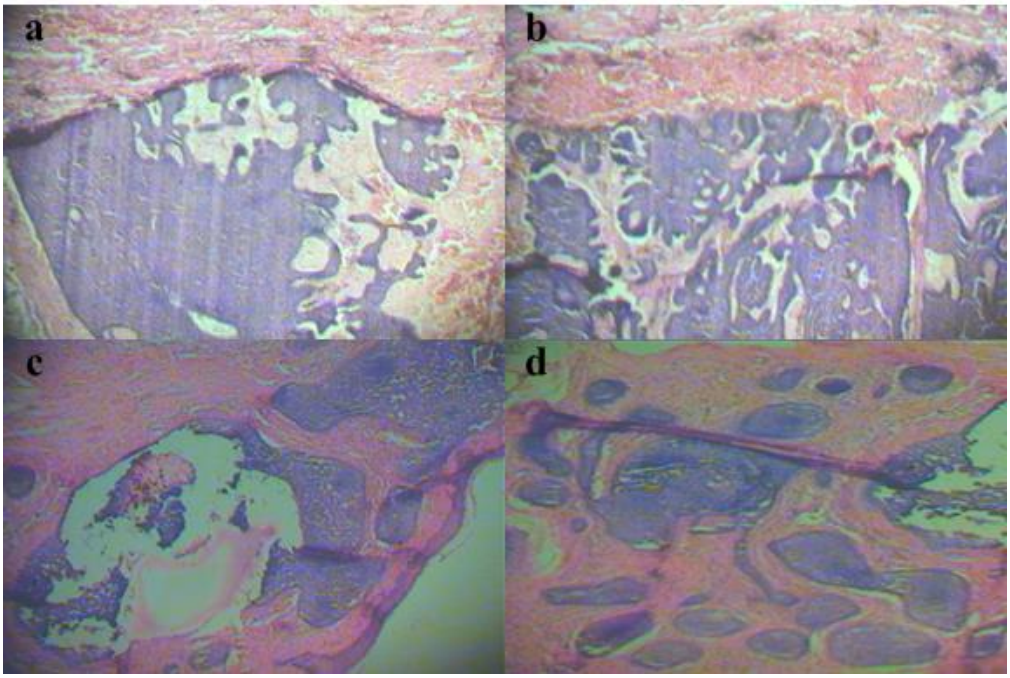

Figure 3-7 White light photo of a representative skin basal cell carcinoma (BCC) tissue sample (20X) with H&E staining for illustrating detail morphology of BCC. The purple islands of BCC can be seen inside the normal stroma (stained pink).

It is important to note that tissue samples of uniform thickness (4 micron) were sliced from the paraffin blocks with great care; however, slight thickness variations can be seen in these samples (Figure 3-7), particularly in the cancerous (BCC) parts of the tissue. Consequently, it is possible that the thickness variations at the location of interaction of the probing beam spots may cause some ambiguity in the polarimetric *point* measurements. To this end, three different spots from each tissue sample were randomly selected; each spot analyzed three times with the help of polarimetric point measurement system. The mean value from these nine measurements generated a single data point corresponding to each tissue sample which was considered for subsequent data analyses. Although we hope that this methodology improved the accuracy and signal to noise ratio (SNR) for the technique, however we suggest future studies to assess the whole tissue sample (more appropriately with imaging setup) in larger sample groups enabling to reach statistically significant and eventually clinically relevant results.

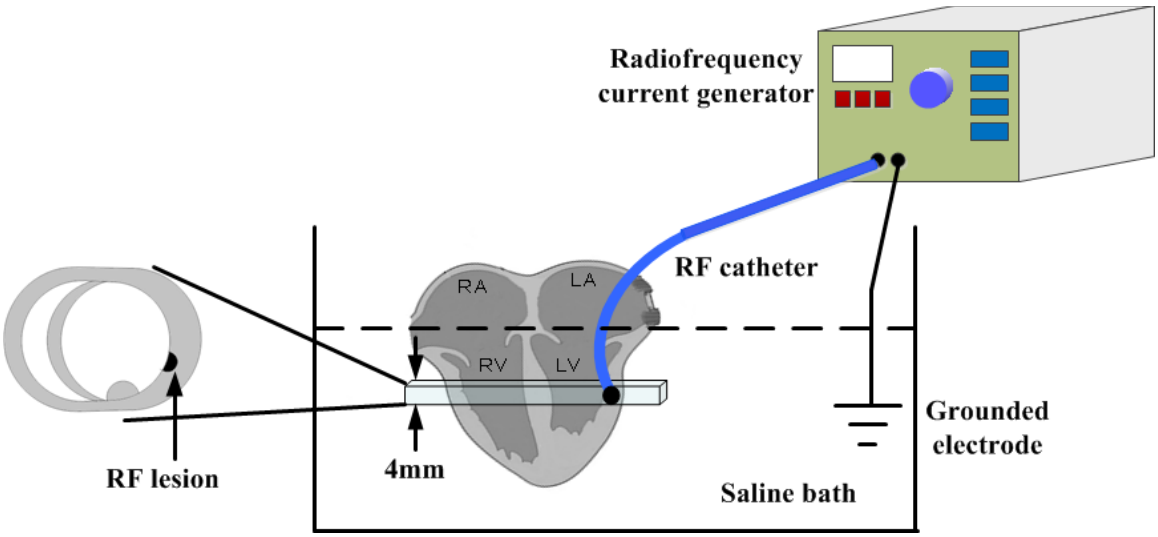

Figure 3-8 Schematic of RF ablation in the porcine heart and the resulting myocardium slice for polarimetric imaging.

3.5.2 Radiofrequency Ablated Myocardial Tissue Samples

All experiments of Mueller matrix imaging system were conducted in *ex vivo* porcine hearts. Ten heart samples (five healthy controls, five with RF ablation lesions) were investigated with Mueller matrix polarimetry. The hearts were harvested from approximately 2-months old slaughterhouse animals weighing about 40 kg. The RF ablation lesions were generated inside the left ventricle (LV) via an intra-cardiac Navistar catheter (Biosense Webster) coupled to a 460 kHz RF generator (Radiotherapeutics, Biosense, Webster). Controlled power setting (applied power of 20-30W) at the tip of the catheter were used for time duration of 40-60 sec. The catheter was positioned onto the endocardium at three different positions; either on the apex, on the septum or on the free wall of LV. The RFA lesion formation was confirmed in the gross pathology through visual inspection. At the completion of the ablation experiment, the hearts were fixed in 10% formalin for several days. After fixation, transverse tissue slices of 4 mm thickness were cut in short-axis view of the heart and subsequently used for optical polarimetric measurements. Figure 3-8 shows a simplified schematic of the RF ablation set-up. Afterwards, histopathological evaluation was performed with the help of hematoxylin and eosin (H&E) and Masson's trichrome staining.

3.6 Local Fuzzy Thresholding Algorithm

For better visual understanding of the obtained polarization images of RF ablated myocardium, differentiation/ segmentation of these images into regions that belong to different underlying pathology is essentially required. Specifically, the depolarization images of the ablated tissue revealed significant contrast in various zones of thermal damage; lower depolarization values in the ablated core compared to the healthy tissue while intermediate values in the rim region. Consequently, this observed contrast was exploited for the segmentation of the depolarization image into the aforesaid three zones. To this end, we used computer-aided methodology to *classify* regions of the total depolarization image belonging to different underlying pathologies, such as RFA core, rim and healthy regions.

Image segmentation has been an integral part of medical image analyses with significantly large number of computer-aided algorithms available towards this target [102]–[104]; however, most of these techniques are rather computationally extensive, application-specific, prone to noise and/or artifacts [105]–[107]. These issues typically arise from the rigid choice of global thresholding. Fortunately, the segmentation algorithm recently developed by Aja-Fernandez *et al.* [108] is computationally efficient and accurate enough to meet the requirements of a clinically acceptable solution for the problem in hand. Specifically, the algorithm is based on a more flexible thresholding approach (local fuzzy thresholding) resulting in efficient and clinically acceptable multi-region (depolarization) image segmentation, as discussed below.

Initially image is smoothed using convolution with Gaussian filter. Then number of segments present in image is predicted (by observing how many different visual regions are present) for the image where, is position vector indicating location of a pixel and is image intensity function. A function called fuzzy membership function is associated to each image segment which is used for calculating association (weights) of each pixel to the given image segment. The maximal association of a pixel to a given fuzzy membership function decides its fate. In our image segmentation technique, fuzzy membership weights (such that) are assigned to each image pixel by minimizing, where and are histogram and probability density function of image segment, respectively.

The probability density function is estimated from histogram by varying parameters space. After selection of initial fuzzy member weights, maximal selection is performed through. This maximal selection yields initial image segments. Unfortunately, the initial image segments do not contain smooth regions, presumably due to image noise. To this end, neighborhood pixel association is performed to refine image segments. Finally, another maximal selection is performed to yield final and refined image segments [108]. These steps are diagrammatically outlined in Figure 3-9.

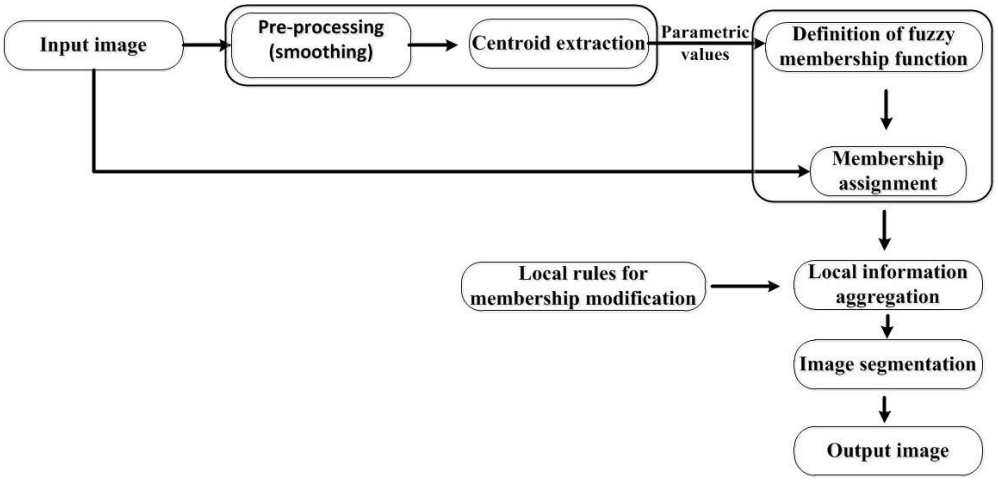

Figure 3-9 Flow chart for local fuzzy thresholding algorithm for multi-region image segmentation.

3.6.1 Ground Truth Segmentation

Manual segmentation was performed by a pathology expert (professor of histopathology) who was blinded to the automated segmentation results. The expert outlined the lesion core and rim boundaries based on the appearance, shape, and size of the cardiomyocytes in the RFA lesion compared to their normal morphology in healthy tissue (changes in microscopic cellular features such as loss of normal elongated structure of cardiomyocytes, cellular desiccation and shrinkage, cytoskeleton damage and increased color intensity (dark-reddish hue)). The digital histology image was magnified twenty-fold to properly assess microscopic features of thermal damage. Closed contours encircling RFA core and rim were drawn, thus separating the tissue into three distinct regions for comparison with the results of the local fuzzy thresholding algorithm.

3.6.2 Performance Evaluation of Local Fuzzy Thresholding Algorithm

Performance and efficiency assessment for establishing new image segmentation algorithms during the design phase is a radically important issue. To this end, various segmentation evaluation criteria have been proposed such as dice similarity coefficient (DSC), Jaccard overlap ratio, Hausdorff distance, etc. However, DSC remains the most widely used assessment metric for the medical image segmentation algorithm [109], [110], which quantitative measure the spatial overlap between two image segmentation schemes; a ground truth segmentation (typically performed manually by an expert) and an automated segmentation (performed by the computer-aided algorithm).

Typically, DSC is defined as the intersection between automated/algorithm (A) based segmentation and the ground truth (GT) segmentation, as given

$$DSC = \frac{2(GT \cap A)}{(GT \cup A)} \tag{3-4}$$

DSC can take values from 0 to 1, which corresponds to the extreme cases of no overlap and perfect congruence between the two image segmentation schemes, respectively. Partial agreement is described by intermediate values (0 < DSC < 1), as shown in Figure 3-10.

In addition to DSC, other metrics studied for the segmentation assessment analysis were *sensitivity* (S_n), the intersection between two similarly labeled regions in ground truth and automated segmentation over the complete extent of GT (Equation (3-5)); *specificity* (S_p), the fraction of the non-target pixels over the non-GT pixels (Equation (3-6)); accuracy *(Acc)*, the fraction of correctly classified pixels over the entire image (Equation (3-7)) [111].

$$S_n = \frac{TP}{TP + FN} \tag{3-5}$$

$$S_p = \frac{TN}{TN + FP} \tag{3-6}$$

$$Acc = \frac{TP + TN}{TP + TN + FP + FN} \qquad (3\text{-}7)$$

These evaluation metrics are shown in the Venn diagram in Figure 3-11.

0

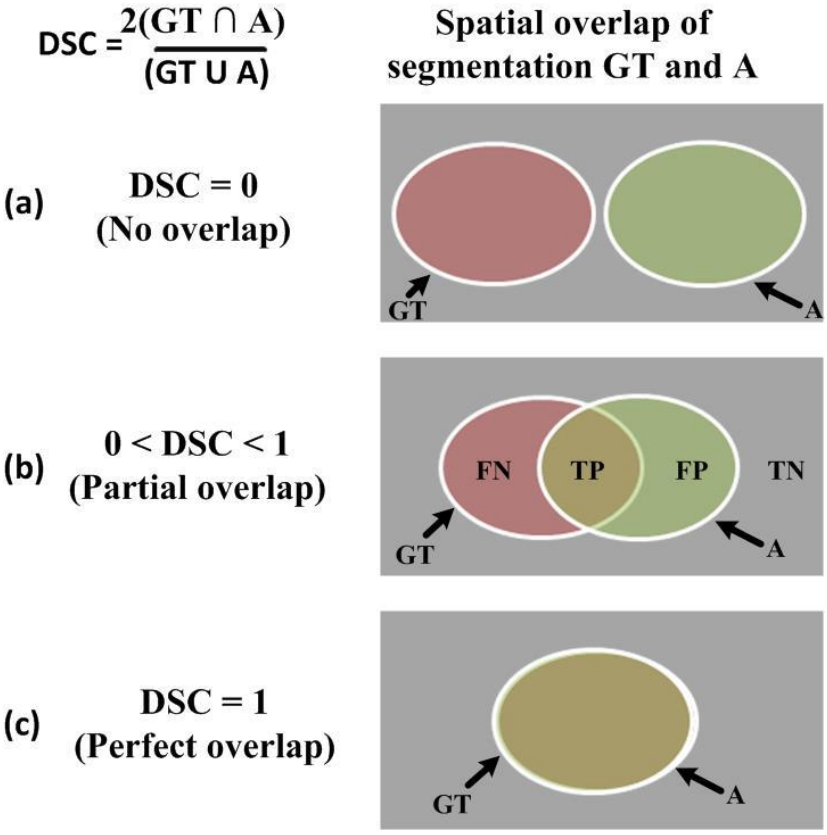

Figure 3-10 Dice similarity coefficient (DSC) representing the spatial overlap of the automated A and ground truth GT segmentation schemes. for (a) no (DSC = 0), (b) partial (0 < DSC < 1), and (c) perfect (DSC = 1) overlap. TP=true positive; TN=true negative; FP=false positive; FN=false negative.

3.7 Statistical Analysis

3.7.1 Wilks Lambda

The Mueller matrix point measurement system was used for the characterization of normal and cancerous tissue samples. Machine learning was used to classify tissue samples in normal and cancerous groups based on differences in their measured polarization properties. For optimization purpose to this end, a statistical tool routinely

employed in classification problems, Wilks lambda was employed for quantitative assessment of discriminative strength of each polarimetric property. Wilks lambda compares the differences between the means of two tissue groups and provides the preliminary screening for classification power of the particular variable. It can take any value between 0 and 1. Values close to 0 indicate that the class means are significantly different and the given variable is a good candidate for classification [112].

3.7.2 Box and Whisker Plot

The box and whisker plot is a comprehensive graphical tool for presenting and visualizing virtually all fine details of large data. The beauty of this plot is that it gives a graphic view as accurate as possible of a population that does not necessarily have a normal distribution [113]. The box lines correspond to the lower quartile (Q_L), median and upper quartile (Q_U) values, respectively. The lines extending from each end of the box (whiskers) indicates the lower and upper extremes of the samples [112]. These five parameters correspond to percentiles P25, P50, P75, P0, and P100 in normal distribution, respectively. The length of the box is the inter-quartile range (IQR) while the length of the whiskers are defined as 1.5 * IQR. Samples with values beyond the ends of the whiskers are outliers and are shown as separated points outside the whiskers. Mild outliers are located between1.5 * IQR and 3 * IQR while extreme outliers are located beyond 3 * IQR from the box edges [114]. In view of these silent features, we analyzed the differences in polarimetric signatures of the two tissue groups through box and whisker plots.

3.7.3 Partial Least Square (PLS) Analysis

Finally partial least square (PLS) analysis was employed to assess the capability of measured optical polarization properties for classification of normal and BCC tissue samples. The confusion matrix obtained from PLS classification was used subsequently to assess the classification efficiency. To this end, quantitative evaluation parameters like sensitivity, specificity, accuracy, and receiver operating characteristic (ROC) curve were calculated. Each individual polarization metric was analyzed on PLS regression for the tissue classification. All data manipulation was done in MATLAB.

4 Polarimetry Based Partial Least Square Classification

4.1 Introduction

Basal cell carcinoma (BCC) accounts for the most commonly occurring human skin malignancy [115]. It is a slow growing epithelial tumor with low malignant potential which is characterized by cells that arise from and resemble basal cells of the epidermis [116], [117]. Clinically such lesions are typically evaluated on ABCDE criteria (asymmetry, border, color, diameter and evolution) and the change in appearance of the mole/pigmented area with time [118]. However, the ABCDE clinical rule being subjective to a large extent, therefore histopathology examination of the suspicious lesion is essentially required for the final assessment.

Biopsy being considered as the gold standard for BCC diagnosis has its own set of advantages and shortcomings. To begin with, it is an invasive procedure which is subjective to operator's (dermatologist and pathologist) skill. Further, biopsy may not be practical in cases with multiple lesions such as in the case of Xeroderma Pigmentosa where the extensive number of skin lesions often make biopsy of each individual lesion very challenging while sampling only few lesions based on clinical experience alone may lead to a misdiagnosis or a delay in diagnosis of the invasive BCC. Consequently, fast and non-invasive approaches for investigating suspicious skin pathologies with minimal procedural times are attracting growing interests [48]–[52]. To this end, optical techniques such as exploiting polarized light measurement are particularly important as these have the potential to explore information about the micro-architecture and biochemical composition of the investigated skin tissue. Specifically, polarized light can be used for exploring tissue parameters closely related to its pathological state such as

density, size, and refractive index of the scattering centers (nuclei, cells, macromolecules, etc.) [53], [54].

Mueller matrix polarimetry provides the complete set of polarization properties of the probed biological tissue. Skin tissue is a particularly suitable site for optical polarimetric investigations owing to its highly fibrous nature. Specifically, the skin extracellular matrix consists of densely packed, highly asymmetric collagen and elastin fiber networks. This anisotropy gives rise to linear retardance which can be sensitively measured with optical polarimetry. Indeed, the loss of collagen fiber structure and integrity (and consequently linear retardance) has been associated with skin pathologies including cancer and thermal injury [55]. Further, a clinically important camera based on polarized light has been developed and successfully demonstrated in guiding the surgical margins of various skin pathologies such as precancerous, benign and cancerous tissues [30], [34], [35]. Additionally, suppression of highly scattered photons that are effectively generated from the deeper skin layers has been utilized for the depth selectivity in bioengineered connective tissues [36], [40]. This approach called polarization gating also significantly improved the image quality in terms of resolution[30], [34].

Despite the fact that various pathological skin lesions have been characterized using optical polarimetry with significant contrast; nevertheless, potential statistical tools for automatic classification of the given tissue pathological state are relatively unexplored. Appropriate classification tool that automatically discriminate tissue's pathological state based on differences in polarimetric variables would be the ultimate goal of such studies. With this aim in mind, we embarked to investigate the differences in polarization properties (depolarization, retardance, and diattenuation) for *ex vivo* normal and BCC tissue samples from human skin using Mueller matrix point polarimetry system over the spectral region 460-800 nm. Significant differences in the polarization properties of the two tissue groups have been observed. Partial least square (PLS) and Wilks lambda statistics were employed to evaluate the potential of measured polarization properties for classification of normal and BCC samples. It is noteworthy that the novelty of this study is to investigate a powerful statistical tool for automatic discrimination of normal and pathological state of tissues based on their polarimetric signatures.

4.2 Results

The experimental setup was validated by measuring the Mueller matrix of air in the spectral range of 400-800 nm prior to its use for tissue samples assessment. Maximum error of 0.7 % was observed. Total- and linear- diattenuation of a linear polarizer were also measured with maximum 1.2% and 1.1% errors, respectively. The setup was also validated by measuring the total- and linear- retardance of a quarter wave plate (QWP) (these results are not shown). The fairly small fluctuations and error in the polarimetric properties of these standard samples validate the excellent performance of the Mueller matrix point polarimetric system.

After validation, the experimental setup was used to measure the polarization metrics of skin tissues. Comparison of total, linear and circular -depolarization for normal and BCC skin tissue samples in the spectral range of 460-800 nm has been depicted in Figure 4-1a, 4-1b, and 4-1c, respectively. It is noteworthy that each numerical value on the graph represents the average value taken over all samples belonging to normal and carcinoma groups. A closer analysis of Figure 4-1 reveals many interesting features: total, linear and circular -depolarization decrease progressively with wavelength. These metrics are significantly higher ($p<0.001$, as determined by unpaired two tail student t-test) for normal tissue samples as compared to BCC samples over the complete investigated spectral range. Further, No overlap in the error bars between normal and BCC samples was observed. The highly significant differences ($p<0.001$) in the depolarization of normal and BCC tissue samples indicate the potential of depolarization as a classification metric for the computer aided pathology categorization. To better demonstrate and analyze the differences in depolarization of the two tissue groups, total-, linear-, and circular-depolarization (Δ_T,Δ_L,Δ_C) at four selected wavelengths (500, 600, 700 and 800 nm) are depicted in Figure 4-2. The significant differences in depolarization for the two tissue groups indicate the possibility to propose a simple approach for tissue pathology classification (diagnosis). It is interesting to note that linear polarization states are better preserved as compared to circular polarization states. This depolarization behavior of the interrogated tissues is entirely fitting in the framework of Rayleigh scattering. We therefore hypothesize that the scattering in the probed tissue samples may be dominated

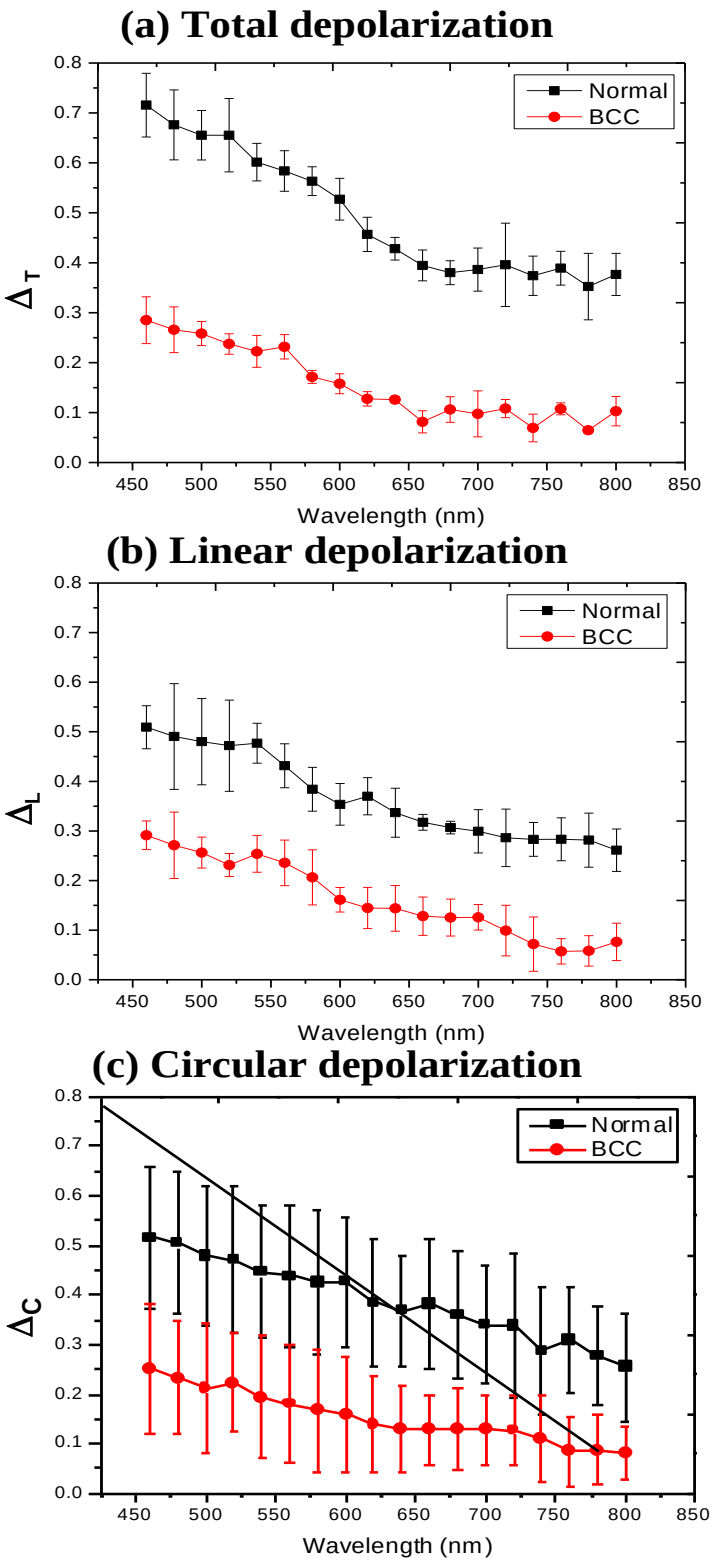

Figure 4-1 (a) total (b) linear and (c) circular depolarization of normal (▪) and BCC (•) skin tissues.

by the Rayleigh-sized subcellular organelles such as tubules of the endoplasmic reticulum, cisternae of Golgi apparatus, etc. However, it may be noted that this depolarization trend appears relatively less obvious 0for BCC tissue samples suggesting that the underlying scattering pattern is perhaps near the Rayleigh-Mie transition regime. For completeness, comparing the results obtained in this study with previous work, it appears that optical scattering by large sized particles of biological tissue such as biological cells falls in the framework of Mie scattering [25].

Experimental results of total and linear -retardance for normal and BCC tissue samples are shown in Figure 4-3. Like depolarization, significant differences ($p<0.001$) were observed in the presented retardance data of normal and BCC skin samples. It is

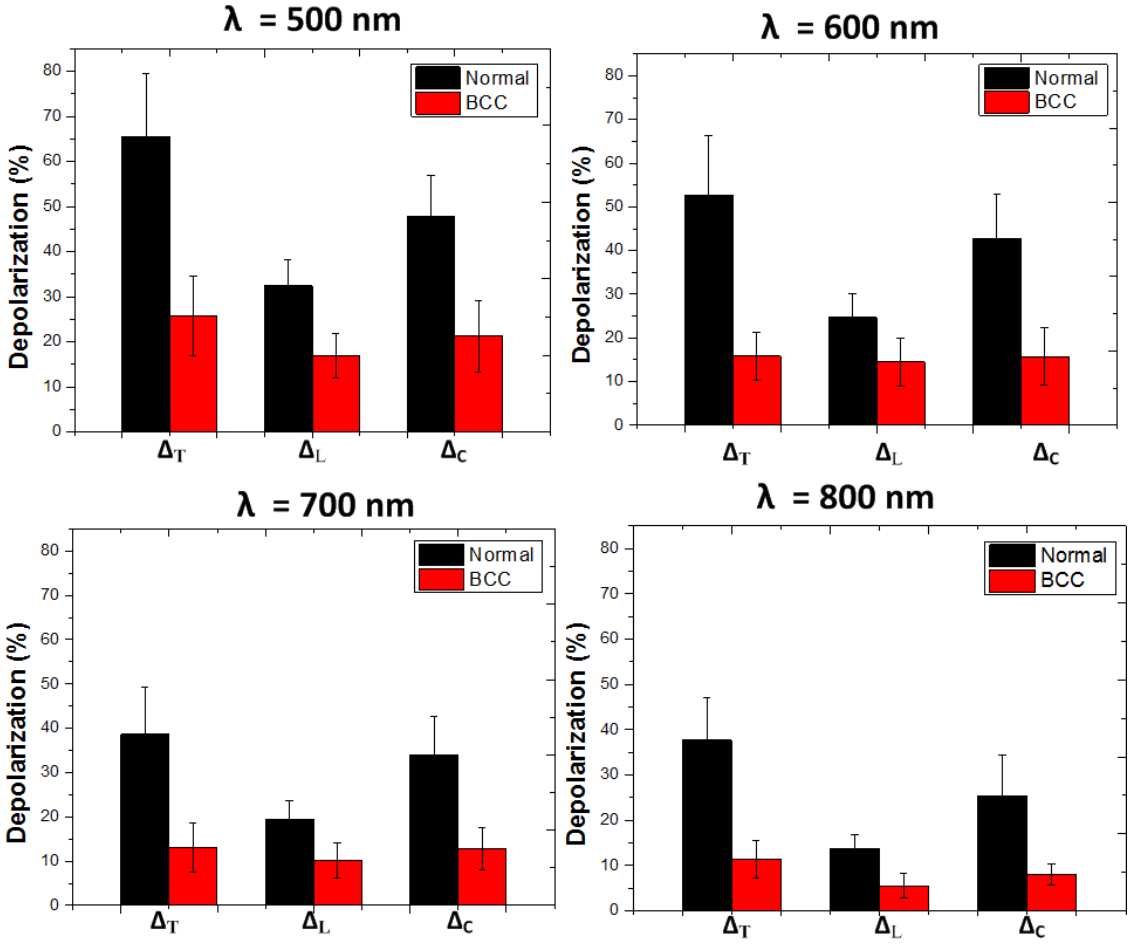

Figure 4-2 Comparison of total, linear, and circular-depolarization for normal and BCC tissue samples at four selected wavelengths.

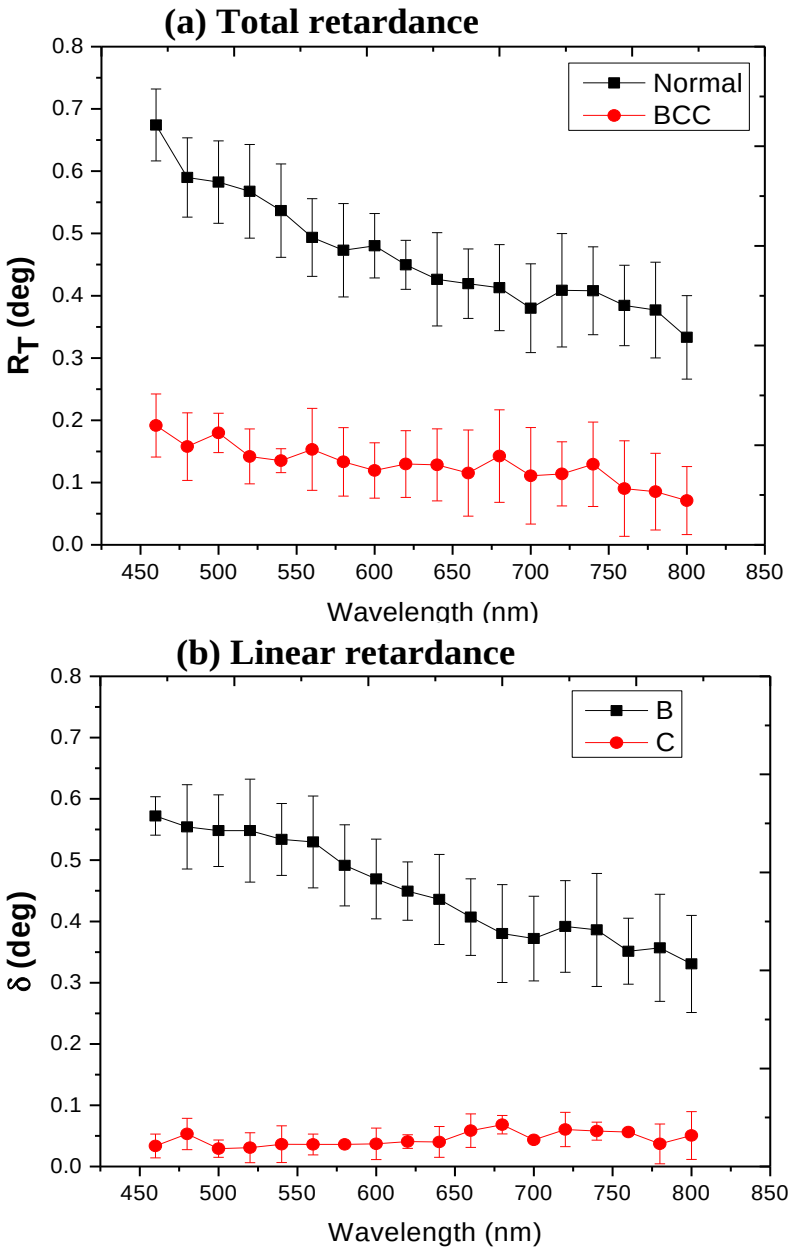

Figure 4-3 (a) total and (b) linear retardance of normal (▪) and BCC (•) skin samples.

noteworthy that the circular retardance for both tissue groups was negligibly small with no considerable differences and therefore not shown.

Figure 4-4 illustrates the measured data of total, linear, and circular -diattenuation for normal and BCC tissue samples as a function of wavelength. It can be appreciated that the differences in circular diattenuation for normal and carcinoma groups are less

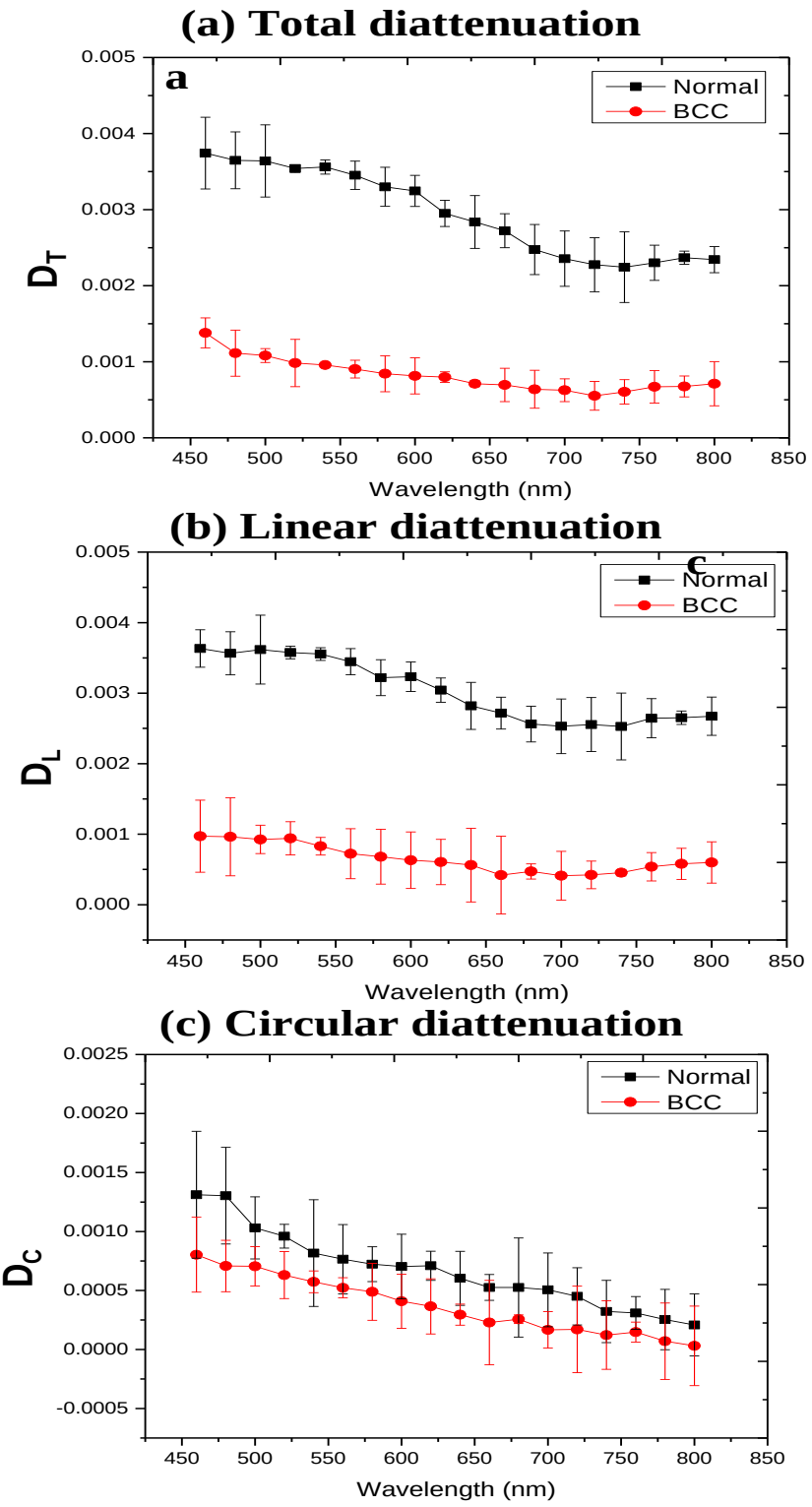

Figure 4-4 (a) total, (b) linear and (c) circular diattenuation of normal (▪) and BCC (•) skin tissues.

prominent unlike the total and linear -diattenuation. Comparing depolarization, retardance and diattenuation, it is clear that depolarization appears as the dominant polarization effect in skin tissue, followed by retardance. Further, it is interesting to note that the variations (represented by error bars) in depolarization are smaller as compared to retardance.

Figure 4-5 illustrates the Wilks lambda values for all polarimetric parameters (Δ_T, Δ_L, Δ_C, R_T, δ, D_T, D_L, D_C) at all investigated wavelengths. It may be noted that Wilks lambda calculated separately for Δ_T, Δ_C, R_T, δ, D_T and D_L have particularly small values suggesting the potential of each of these individual variables to separate the two classes. We therefore expect efficient classification by partial least square (PLS) analysis when these variables are considered all together. Indeed, PLS analysis resulted in 100 % accuracy, specificity and sensitivity for classifying the two tissue groups, as discussed below. The slightly high Wilks lambda values for Δ_L at the longer wavelengths also

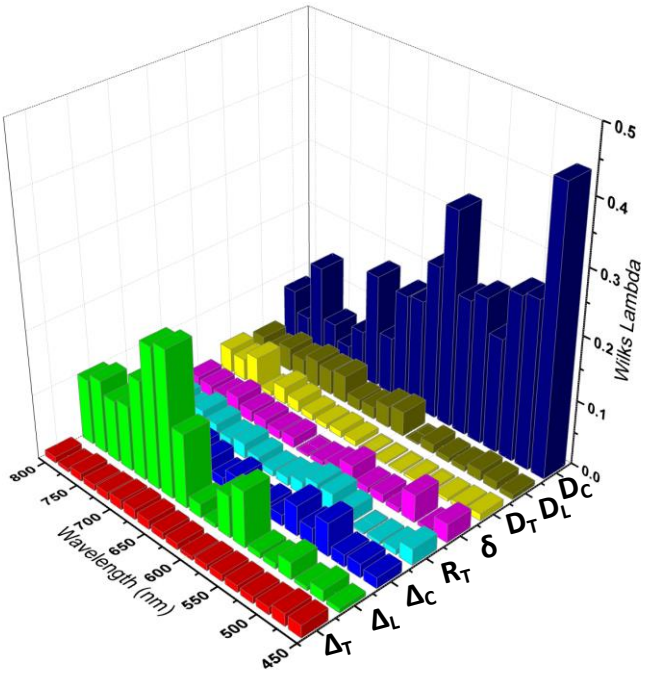

Figure 4-5 Walks' lambda values for all polarimetric properties at all the investigated wavelengths.

resulted in good classification. Further, the relatively large values of Wilks lambda for D_C can be correlated with the small differences observed in circular diattenuation for normal and BCC tissue samples as shown in Figure 4-4c.

Figure 4-6 shows the box and whisker plot for total depolarization of the two groups, as a representative case of all polarimetric properties. Logarithmic transformation was applied to the original depolarization data so that the ranges and distributions of all data points (particularly for BCC tissue samples) become comparable. Significantly large number of outliers was identified in the BCC as compared to normal samples group. This

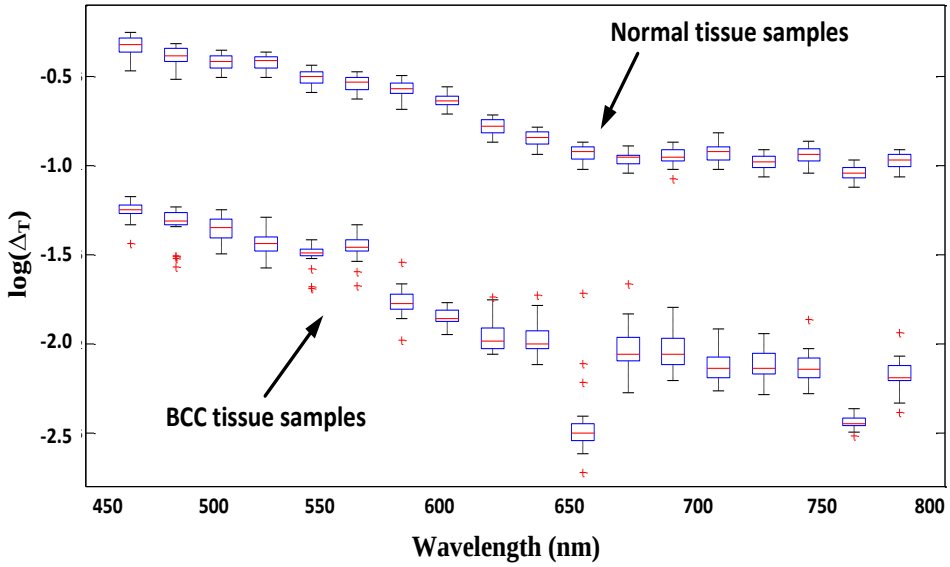

Figure 4-6 Box and whisker plot of log transformed data of total depolarization for normal and BCC tissue samples.

interesting observation could probably be stemmed from the greater heterogeneity in subtype and/or architecture of various BCC tissue samples, as supported by Figure 3-7. However, the beauty of box plot is that the influence of such outliers on statistical analyses of the data is considerably limited.

PLS analysis was used to quantitatively evaluate the classification performance of optical polarimetry based on the observed differences in polarization properties of the two tissue groups. Results from only one representative metric (total depolarization) are

discussed for briefness. All other polarimetric properties except circular diattenuation behave almost similar results for classification.

Table 4.1 Confusion matrix obtained from PLS analysis based on total depolarization

Histopathology class	PLS Predicted Class	
	BCC	Normal
BCC	26	0
Normal	0	26

Table 4.2 Classification parameters obtained from PLS analysis based on total depolarization

	Accuracy	Sensitivity	Specificity
Normal	1	1	1
BCC0	1	1	1

Confusion matrix describes classification parameters in the most fundamental form i.e. true positive (TP); true negative (TN); false positive (FP); false negative (FN). Other useful parameters like accuracy, sensitivity, specificity and ROC curve are derived from confusion matrix. Table 4.1 shows the calculated confusion matrix for normal and BCC tissue samples derived from PLS analysis. Elements 1 and 2 (first row) of confusion matrix represent TP and FN for BCC tissue samples, respectively. Likewise, elements 3 and 4 (second row) represent FP and TN for normal tissue samples, respectively. Accuracy (the fraction of all correctly classified samples), sensitivity (the fraction of correctly classified BCC samples) and specificity (the fraction of correctly classified normal samples) are the basic indexes for quantitative assessment of PLS discriminating power. PLS provided 100 % test accuracy, sensitivity and specificity for total depolarization as depicted in Table 4.2. Further, the combinations of sensitivity and specificity are employed for plotting ROC curve. Area under ROC curve provides more direct measure of classification performance. Figure 4-7 shows the calculated ROC based on total depolarization of normal and BCC tissue samples. Perfect classification is described by highest possible area under ROC curve values (100%).

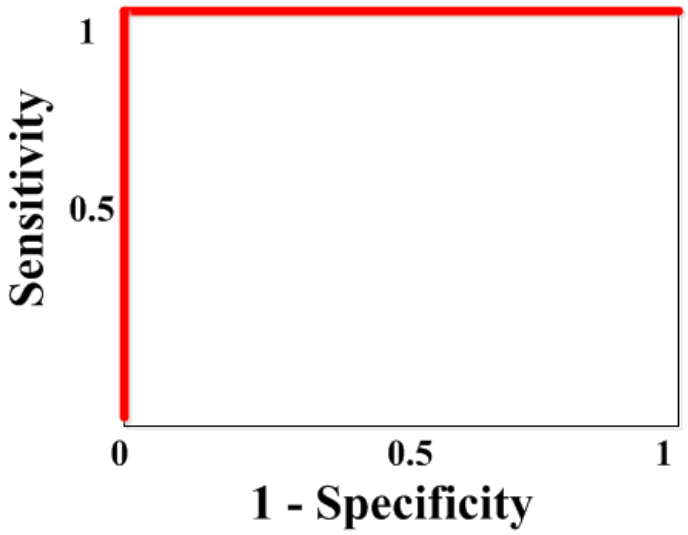

Figure 4-7 PLS based ROC curve for total depolarization.

4.3 Discussion

In this study, we investigated Mueller matrix point polarimetry for the quantitative assessment of *ex vivo* normal and BCC tissue samples. Comparisons of depolarization and retardance measurement from normal and BCC tissue samples demonstrated significant differences, illustrating the ability of optical polarimetry for BCC detection. Partial least square analysis was used for automated classification of the two tissue groups.

Depolarization is the randomization of the electric filed vector of input optical beam and is essentially associated with scattering, diattenuation, and retardance caused by the probed medium. However, the observed diattenuation and retardance are relatively small suggesting that the depolarization is primarily caused by scattering. Further, it was noted that depolarization decreases with wavelength for both normal and BCC tissue samples (Figure 4-1). This is considered as a general trend in biomedical optics as observed in many other studies [12], [27], [97], [119], [120] and has been attributed to the decrease in Rayleigh scattering with wavelength.

Significant difference ($p<0.001$) in depolarization of normal and cancerous skin tissue samples was observed in the conducted experiments. Previously, it has been observed that the scattering coefficient of cancerous skin lesions (BCC) is consistently

lower as compared to normal tissues over a wide wavelength range [119]. Consequently the depolarization power of normal skin tissue dominates over that of BCC samples. Further, the observed differences in depolarization indicate the presence of characteristic morphological changes in BCC tissue samples. Since the scattering of epidermis is significantly higher than the scattering of dermis and subcutaneous fat in the entire visible spectral range [121], we therefore emphasize on the pathological changes that occur at molecular levels in *epidermis* for a possible description of the smaller depolarization of BCC tissue samples.

Microscopic features of BCC include nuclear enlargement, increased nuclear-cytoplasmic ratio, and higher chromatin concentration. These histologic hallmarks of BCC tissues are also revealed by other optical detection techniques such as infrared spectroscopy [122] and light scattering spectroscopy [123]. Further, nuclei become variable in size and shape [123], [25], [27]. We believe that the relatively small depolarization observed for cancerous tissue samples is strongly correlated to these morphology alterations in nuclear size and density, as consistently reported in other studies [124]–[127].

Retardance essentially evolves from the asymmetric nature of the investigated medium. Specifically, the difference of indices of the refraction for various directions within the medium causes the probing beam to travel at different velocities. As a result, the output beam after interaction with the medium is splitted into two orthogonal polarization components, one lagging behind the other. For biological tissues such as skin, the optical asymmetry arises from the presence of certain macromolecules. The intermediate skin layer (i.e. the dermis) is composed of fibrous rich extracellular matrix, where collagen and elastin fibrils are packed in bundles for providing the required mechanical strength and organization [55]. While the size and relative concentration of the individual fibers depend on the particular location in the skin; the typical size of the fibrils is 60–100 nm and the size of the bundles is in the range of 1–8μm [128]. Retardance observed for skin tissue samples inherently stems from these asymmetric fibers and molecules.

Retardance changes for BCC samples as compared to normal samples are more sensitive to scattering by the structures in extracellular matrix. Specifically, the well-organized network of collagen and elastin fibers in dermis is somehow disturbed by BCC as illustrated in Figure 3-7 where the groups of basiloid hyperchromatic cells are intervening the lose fibrous tissue stroma. The fairly reduced collagen content and density in the BCC tissue samples permits for significantly smaller ($p< 0.001$) retardance compared to normal tissue samples.

Alterations in retardance for skin tissues has been successfully measured and correlated to other dermatological conditions. For instance, depth-resolved retardance quantification and imaging with the help of PS-OCT has been used for the assessment of wound healing and repair in skin tissues [55]. Thermal denaturation of collagen results in the loss of tissue retardance. The dynamic changes in retardance during tissue heating have been used to monitor the degree of thermal damage and model the kinetics of the reaction [129], [130]. Further, the orthogonal polarization spectral imaging has evolved as a promising tool for dermatologists as this technique have the potential for *in vivo* transcutaneous assessment of the skin microcirculation avoiding the need for invasive surgical techniques [131].

Relatively larger variations in retardance (Figure 4-3) as compared to depolarization (Figure 4-1) can be attributed to the variations in collagen size and distribution in the investigated BCC tissue samples collected from various anatomical locations of skin. Specifically, the presence of collagen is established at all anatomical locations of skin; however, the size, distribution, and concentration of individual collagen fiber vary according to the anatomic location. For example, the skin of torso and limbs is relatively thick (thick dermal layer) having large bundles of collagen fibers, resulting in significantly higher retardance. On the contrary, the skin covering the face is thinner having finer collagen bundles, resulting in lower birefringence. Since the optically examined BCC tissue samples were collected from a variety of skin anatomic locations, therefore resulting in relatively larger variations in retardance. Further, collagen and subsequent stroma remodeling are known to be the fundamental feature of invasive BCC. The degree of such structural alterations also contributes to the variation in retardance.

Diattenuation is the property of the given medium whereby the preferential attenuation of probing beam depends on the incident polarization state. In spite the relatively weak diattenuation signal measured for the investigated skin tissue samples, we were able to observe differences between the two tissue groups.

The observed differences in polarimetric properties of the two tissue groups were rigorously analyzed statistically with the ultimate goal of translating the knowledge of expert pathologist/physician into a computer program for automated classification. This goal would result in several advantages, in particular the elimination of physician subjectiveness. For optimization purpose, the strength of each polarimetric parameter for classification was assessed with the help of Wilks lambda prior to the application of computer assisted method. For both depolarization and retardance, obtained Wilks lambda values close to zero indicated their potential for classification. Partial least squares analysis method was used for the classification of BCC samples based on the polarimetric data. The evaluation metrics such as sensitivity, specificity and accuracy of PLS analysis demonstrated the method's effectiveness in predicting BCC and normal tissue samples. However, the claimed efficiency of the automated BCC classification should be carefully evaluated since the results are greatly subjected to the lesions features such as anatomic location and stage. In summary, our findings indicate the capability of polarimetric differences coupled with PLS analysis method for automated classification of new data.

It is noteworthy that there are various pathological subtypes of BCC including nodular BCC, infiltrative BCC, morpheaform BCC, superficial BCC, etc. that are classified on the bases of differences in histological features such as tumor size, stroma contents and invasive depth. That said, the polarimetric properties may distinct among different subtypes of BCC and the proposed classification machine may be capable to differentiate these subtypes; however, this aspect will be explored in the future, when we plan to extend this work to much larger sample cohort with all pathological subtypes of BCC. However, as a first step, we have focused our efforts on binary classification of normal vs. BCC tissues only in this preliminary study.

4.4 Summary

In this study, polarimetric properties of *ex vivo* normal and basal cell carcinoma human skin tissues were investigated in the spectral range of 460-800 nm. Tissue samples were fixed on glass slides for both histopathological and polarimetry studies. Mueller calculus and polar decomposition enabled us to extract the individual polarization metrics that completely characterize the probed tissues. The results indicate that all the polarization parameters namely $\boldsymbol{\Delta_T}$, $\boldsymbol{\Delta_L}$, $\boldsymbol{\Delta_C}$, $\mathbf{D_T}$, $\mathbf{D_L}$, $\mathbf{D_C}, \mathbf{R_T}$ and $\boldsymbol{\delta}$ were significantly higher ($p<0.001$) for normal skin tissues as compared to BCC samples. The performance of detection method was further assessed by Wilks lambda, box and whisker plot and PLS classification. Wilks lambda illustrated that all measured polarimetric properties except circular diattenuation are good candidates for the discrimination of normal and BCC skin samples. Moreover, PLS classification analysis provided perfect accuracy, sensitivity and specificity for classification. PLS discrimination seems potentially convincing for tissue classification based on differences in polarimetric properties.

5 Polarization Imaging of Porcine Myocardial Tissue

5.1 Introduction

Abnormal heart rhythms (cardiac arrhythmia) typically develop from coordination problems in the electric signaling system of the heart. Structural remodeling of the cardiac muscle tissue presumably facilitate malfunctions in the cardiac conduction system [58]. Consequently, adequate quantitative appraisal of the arrhythmic node(s) in terms of its benchmarks like spatial extent, position, and degree of severity is essential towards subsequent treatment that account for the impairment in coordination system.

Catheter ablation using radiofrequency (RF) energy is a potential treatment for cardiac arrhythmias [59] where the delivered RF energy specifically destroy the arrhythmogenic foci, primarily by resistive heating of the target tissue. Higher temperature profiles (> 50° C) in close proximity of the RF catheter cause permanent tissue destruction via coagulative necrosis [132]–[134]. Alternatively, remote tissue from the RF catheter is minimally heated and ergo maintains its healthy morphology. Tissue with intermediate temperatures (37° C < T < 50° C) contains both viable and non-viable cells. Consequently, the ablated tissue consists of a lesion core (i.e. coagulative necrotic area) surrounded by a rim of both viable and non-viable cells and healthy tissue afterwards [60], [61]. Better characterization of these three distinct zones in a typical ablation lesion in terms of imaging may help towards improvement in treatment assessment, follow up and outcome of these procedures.

Optical imaging techniques for characterization of different pathologies are attractive due to their many salient advantages [48]–[52]. Previously, RF ablated cardiac tissue has been qualitatively assessed by optical coherence tomography (OCT) [71], [72] and photoacoustic imaging (PI) [73]. However, polarization imaging for characterization

of RF ablated cardiac tissue has been relatively unexplored. Nevertheless, cardiac tissue presents a particularly appropriate model for polarimetric investigations in terms of the highly anisotropic nature of its constituents such as cardiomyocytes, collagen fibers, etc. This anatomical anisotropy contributes towards optical linear retardance, the magnitude and direction of which can be sensitively measured and quantified with optical polarimetry.

In this chapter, we explore the capability of optical polarimetry to visualize a typical myocardial radiofrequency ablated (RFA) lesion including the necrotic core and the rim. In particular, we investigate contrast in depolarization and linear retardance images (both magnitude and orientation) for normal and RF-ablated tissues in *ex-vivo* porcine hearts, using Mueller matrix polarimetry. We hypothesize that necrosis of thermally ablated myocardial tissue leads to a loss of structural anisotropy resulting in lower linear retardance and depolarization. Such polarimetric changes may be correlated to morphological and structural changes that can be validated by histology.

5.2 Results

Images from one representative healthy control porcine myocardial sample are presented in Figure 5-1 to 5-3. The first sample from the septum of the myocardium served as a control (i.e. healthy myocardium with no RF ablation). The septum region analyzed with optical polarimetry is encircled in Figure 5-1a and a corresponding magnified view shown in Figure 5-1b.

Images showing three polarimetry metrics, depolarization, linear retardance magnitude, and linear retardance orientation, are shown in Figure 5-2a, 5-2b and 5-2c, respectively. Fairly uniform depolarization was observed throughout control sample 1(Figure 5-2a). Linear retardance magnitude also appeared uniform, with slightly more variation than seen in the depolarization image (Figure 5-2b). To show the linear retardance orientation, we superimposed dashed lines over an image of the linear retardance magnitude. These lines each represent the mean orientation directions averaged over a region of interest (ROI) region of 35 x 35 pixels (this ROI size was chosen for visual convenience). It is noteworthy to mention that polar decomposition of

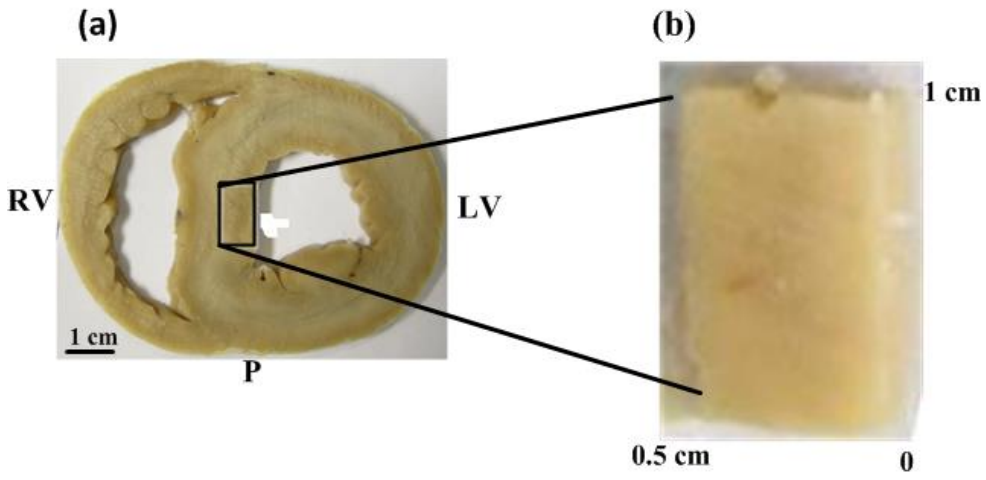

Figure 5-1 (a) White light photograph of gross untreated myocardial tissue sample (control 1) from the septum, (b) magnified view of ROI from the sample.

Mueller matrix uses the fast optical axis as the reference axis for retardance orientation [94]. However, in cardiomyocytes it is the slow axis that is aligned with the fibers [135]. Consequently, measured retardance orientations should be shifted by 90^{o} to match with the 'true' fiber directions. Indeed we found the orientation of linear retardance to be perpendicular to the myocardium fibers as viewed with histology (Figure 5-3). For ease of interpretation, we have plotted the dashed lines in the direction of the slow optical axis, so that they reveal the myocardial fiber orientation.

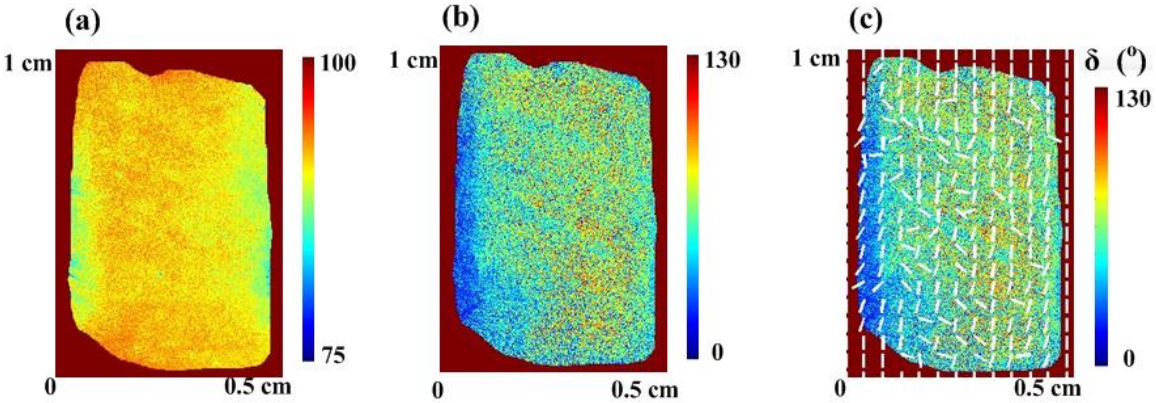

Figure 5-2 (a) Depolarization map, (b) linear retardance magnitude map, and (c) linear retardance orientation is represented by white dashed lines superimposed over the linear retardance magnitude map for the healthy myocardium sample shown in Figure 5-1.

The polarimetry findings were interpreted and qualitatively compared with Masson's trichrome and Hematoxylin and eosin (H&E) histology, shown in Figure 5-3a and 5-3b, respectively. For Masson's trichrome staining, the cytoplasm appears red/pink, nuclei are dark red/purple, and the connective tissue (e.g. collagen) is stained blue. For H&E staining, the cytoplasm appears pink and nuclei are stained violet. As revealed by histology (Figure 5-3), the healthy myocardium is almost entirely composed of aligned arrays of cardiomyocytes (stained red). Occasional intervening long strands of blue stained collagen fibers were also observed in the Masson's trichrome staining (Figure 5-3a).

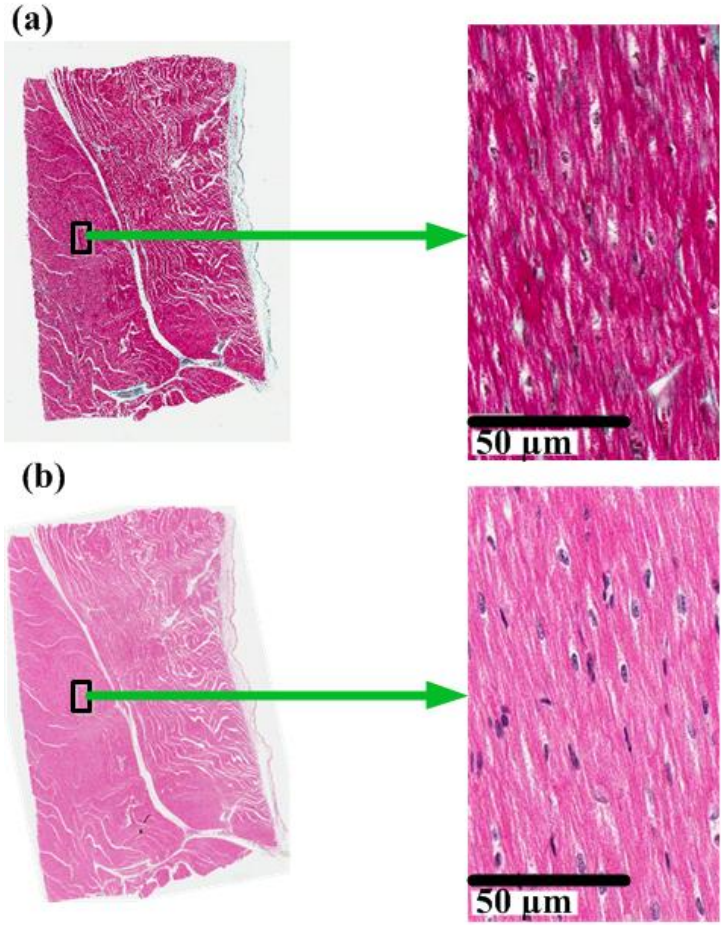

Figure 5-3 Histology with (a) Masson's trichrome and (b) H & E staining and corresponding magnified (20X) histology images of healthy myocytes of the sample shown in Figure 5-1.

Figure 5-4 shows the results from a myocardium sample with an RF lesion. The sample was from the apex of myocardium with single RFA lesion, approximately 1 cm^2 in area. The location where the RF catheter was placed in the tissue is shown by a black circle (Figure 5-4a). A magnified view of the region analyzed with polarimetry is shown in Figure 5-4b. The core of the RFA lesion appears white presumably due to coagulative necrosis, and the perimeter is darker due to hemorrhage (red blood cells in the extravascular space due to collapsed microvessels) [60].

Optical polarimetry measurements such as depolarization, linear retardance magnitude, and linear retardance orientation images of RFA sample 1 are shown in Figure 5-5a, 5-5b, and 5-5c, respectively. It may be noted that reduced depolarization

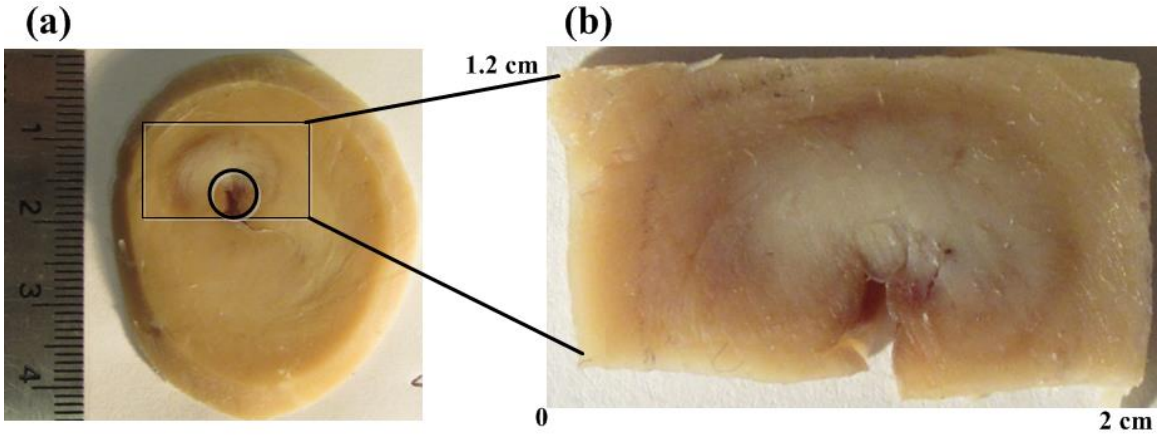

Figure 5-4 (a) White light photograph of gross myocardial tissue with RFA lesion and (b) magnified view of ROI from the sample.

values were observed in the RFA lesion compared to surrounding healthy tissue (Figure 5-5a). Specifically, the decrease in depolarization was more prominent at the center of RFA lesion (i.e. RFA core) and increased gradually towards healthy tissue at the remote periphery of the RFA lesion. The regions of decreased depolarization correlated well qualitatively with the spatial extent of the RFA lesion as visualized under white light and with histology. Depolarization may thus form a useful polarimetric surrogate to delineate RFA lesion extent. Indeed, the contrast in depolarization values has been exploited to segment the depolarization image into RFA core, rim and healthy regions, as discussed in full length in the next chapter.

The map for linear retardance magnitude (Figure 5-5b) demonstrates lower values for the RFA lesion compared to the healthy region. Beginning at the RFA core and progressing radially towards the healthy tissue, we observed a region of diminished linear retardance followed by a zone with moderate values and finally higher linear retardance in the healthy tissue. A corresponding gradual recovery in tissue organization (and consequently linear retardance magnitude) from RFA core towards remote healthy tissue was confirmed with histology. Further, this behavior of linear retardance is also consistent with the depolarization (discussed above) indicating the possibility of a positive correlation between these two important polarimetric parameters; this important point is further emphasized and correlated with other studies in the next section.

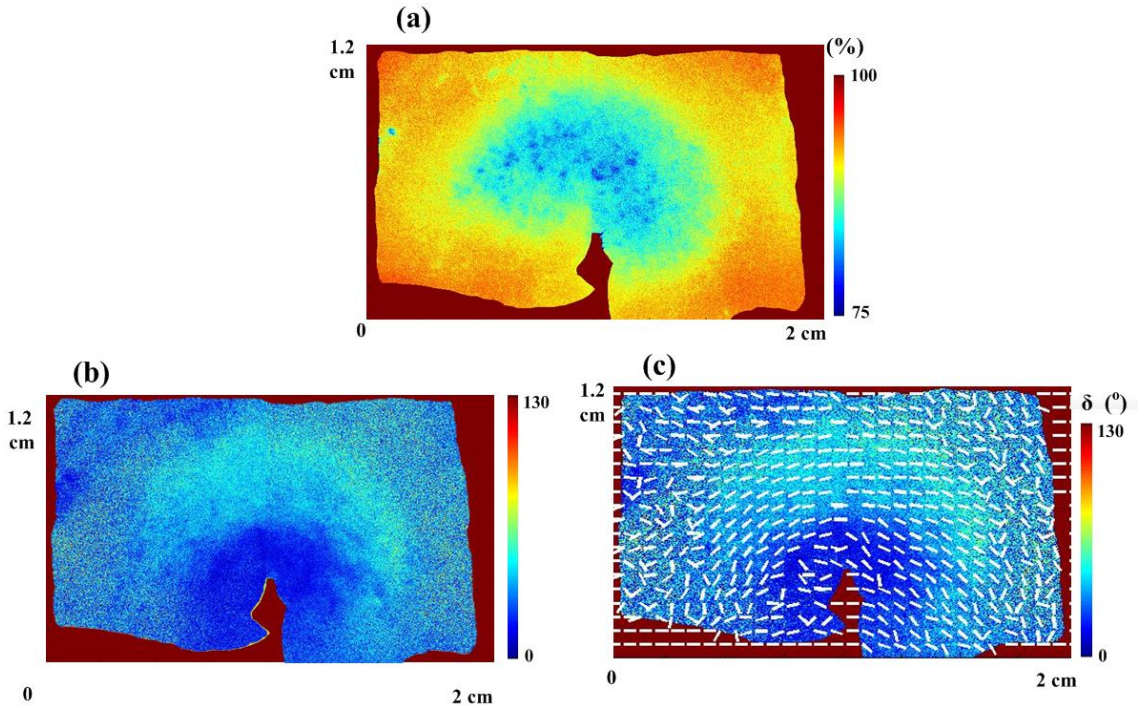

Figure 5-5 (a) Depolarization map, (b) linear retardance magnitude map, and (c) linear retardance orientation is represented by white dashed lines superimposed over the linear retardance magnitude map for the RF ablated myocardium sample shown in Figure 5-4.

In addition to linear retardance magnitude, the linear retardance orientation for RFA sample 1 is presented in Figure 5-5c. The linear retardance orientation is represented by white dashed lines superimposed over the image of linear retardance magnitude. As previously mentioned, we have plotted the orientation of the slow optical

axis, as this corresponds to the myocardial fiber orientation. It was observed that the linear retardance orientation rotates circumferentially. Closer examination of histology also revealed similar circumferential alignment of the cardiomyocytes in this treated region. Interestingly, the orientation of linear retardance is maintained in the RFA core within the ablated region. This behavior is discussed in the next section.

The optical polarimetry observations were correlated and validated with Masson's trichrome and H&E histology, shown in Figure 5-6 and 5-7, respectively. In contrast to control sample 1, cardiomyocytes within the RFA core region (Figure 5-6b) suffered

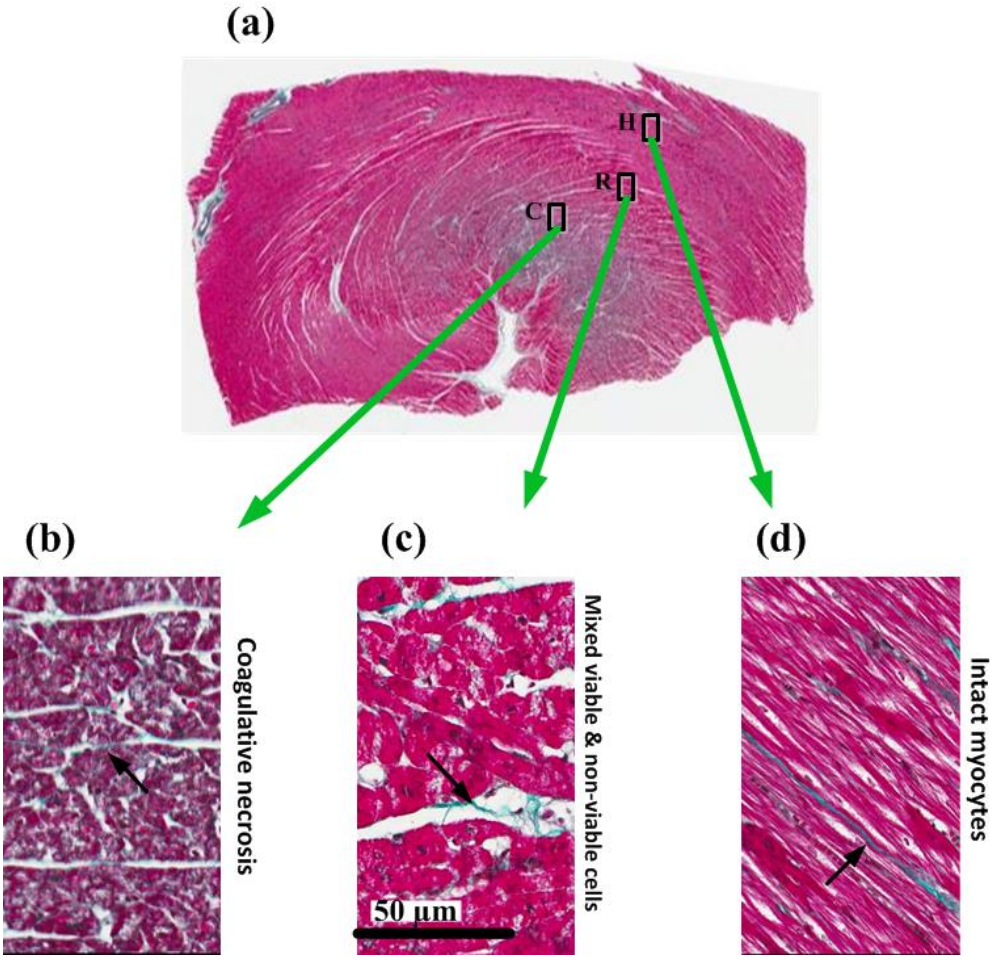

Figure 5-6 Histology with (a) Masson's trichrome staining of the RFA sample 1, and magnified (20 X) images of rectangular ROI boxes from (b) RFA core, (c) rim region, and (d) healthy region. C - core; R - rim; H - healthy regions.

thermal insult with coagulative necrosis, as demonstrated by histology. Cellular

membrane and morphology are structurally altered but maintained some residual architecture. Nuclear integrity appears irreversibly damaged.

Histological staining also showed a dark-reddish hue with black zones (due to myoglobin denaturation), which are markers of extensive thermal damage [5]. Further, close examination of collagen fibers revealed evidence of thermal damage with broken strands and random orientations. Unlike the collagen in healthy region of myocardium, the collagen strands in the RFA lesion appear 'wavy'. The polarimetry changes due to RF ablation make sense in the context of the microstructural changes observed with histology.

Figure 5-7 shows histology of RFA sample1 with H&E staining. In contrast to Figure 5-6, the collagen fibers are not stained. However, the nuclear staining (represented by small violet dots) revealed more detailed morphology as compared to Masson trichrome staining. In general, findings of H&E staining agree with that of Masson trichrome. Specifically, Figure 5-6b (RFA core) indicates loss of cellular integrity and reduction in nuclear size while Figure 5-6d (healthy region) shows well-aligned parallel arrays of cardiomyocytes. The rim region demonstrated intermediate thermal damage with altered cell morphology (Figure 5-6c), as expected.

For subsequent quantitative analysis, the mean depolarization and linear retardance magnitude in a region of interest (50 x 50 pixels) were calculated for all healthy control (Table 5.1) and RF treated (Table 5.2) samples. For RFA samples, these mean polarimetry metrics were calculated in three different regions corresponding to the RFA lesion core, lesion rim, and an undamaged healthy region. The resultant mean values of depolarization and linear retardance magnitude for both tissue groups are plotted in Figure 5-8.

Depolarization was lowest in the RFA core region and highest in the healthy regions with intermediate values in the RFA rim region. Depolarization was significantly different between the RFA healthy, RFA rim and RFA core regions as determined by two-tailed unpaired t-tests ($p<0.05$). Identical trends were

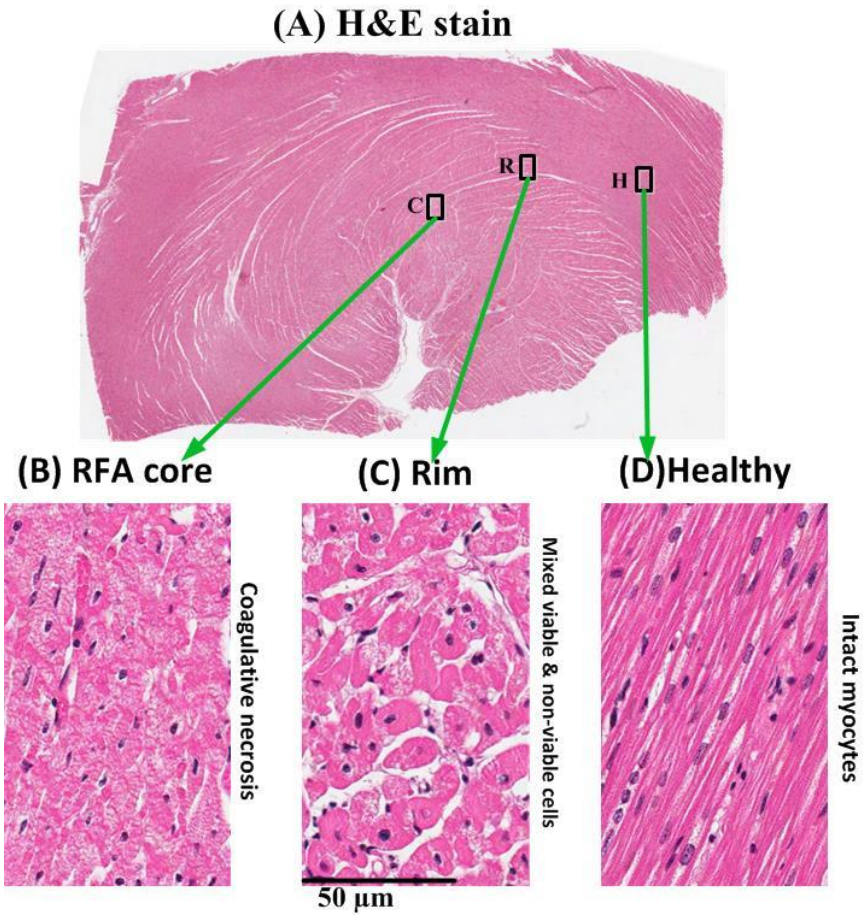

Figure 5-7 Histology with (a) H&E staining of the RFA sample 1, and magnified (20 X) images of rectangular ROI boxes from (b) RFA core, (c) rim region, and (d) healthy region. C - core; R - rim; H - healthy regions.

seen between the control healthy, RFA rim, and RFA core regions ($p<0.05$). There was no significant difference between the control healthy group, and the RFA healthy region, as expected.

Table 5.1 Depolarization and linear retardance magnitude of healthy control samples (ROIs = 50 x 50 pixels).

Control sample	Depolarization Δ_T (%)	Linear retardance magnitude δ (deg.)
1	91.6	62.1
2	93.4	58.1
3	92.7	66.2
4	94.0	55.0
5	93.1	57.0
Mean ± SD[1]	93.0 ±0.8	59.6 ± 4.0

Table 5.2 Depolarization and linear retardance magnitude of samples with RFA lesions (ROIs = 50 x 50 pixels).

RFA sample	Depolarization Δ_T (%)			Linear retardance magnitude δ (deg.)		
	Healthy Region	Rim Region	RFA Core	Healthy Region	Rim Region	RFA Core
1	90.7	87.0	82.9	42.6	43.8	37.7
2 a[2]	90.5	88.5	83.9	66.1	51.2	32.6
2 b[2]	91.8	88.2	84.3	64.8	60.1	42.0
3	90.0	85.3	77.2	52.5	39.2	31.0
4	91.8	89.4	88.0	65.9	32.3	36.7
5	93.9	88.6	85.7	54.6	23.1	15.3
Mean ± SD[1]	91.5 ± 1.3	87.7 ± 1.4	83.3 ± 3.5	57.8 ± 8.7	45.3 ± 9.6	36.0 ± 3.9

[1] Standard deviation [2] Two RFA lesions on the same sample

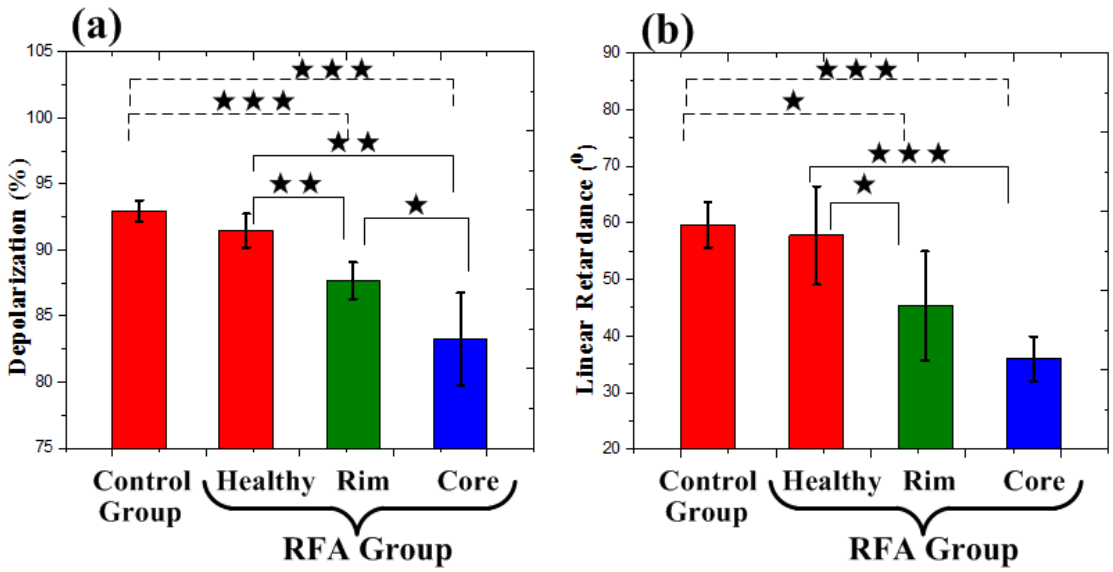

Figure 5-8 (a) Mean depolarization and (b) linear retardance for RFA (healthy, rim and core regions) and control samples. Error bars show standard error. ★= p value < 0.05; ★★ < 0.01; ★★★ < 0.001, calculated with two-tail unpaired t-test.

Similarly, linear retardance magnitude was lowest in the RFA core region and highest in the healthy regions with intermediate values in the RFA rim region. Linear retardance was significantly lower in the RFA core than the RFA healthy regions ($p<0.05$). Identical trends were seen between the RFA core and control healthy regions ($p<0.05$). There was no significant difference between the control healthy group and the RFA healthy region, as expected. Interestingly, although the retardance in the RFA rim

region was lower than in the RFA core, the results were not significant. Based on this, depolarization may a better (more sensitive) metric for determining the extent of RFA lesions.

5.3 Discussion

In this study, we explored Mueller matrix polarimetry for the quantitative assessment of RFA lesions in myocardial tissue. Comparisons of two polarimetric parameters namely depolarization and linear retardance images from healthy tissue and RFA lesions demonstrated significant lesion visibility, illustrating the ability of optical polarimetry to detect and assess the spatial extent of RF-induced thermal damage.

The observed trends in depolarization can be interpreted by considering two factors: multiple scattering and intrinsic tissue anisotropy. Multiple scattering of light is primarily due to the turbid heterogeneous nature of the biological tissue. The amount of scattering is sensitive to tissue parameters like scatterer (cells, nuclei, connective tissue fibers, etc.) size, shape, and density, all causing complex patterns of refractive index variations [13]. Thermal coagulation caused by high local temperatures, RF current and temperature-induced protein denaturation significantly alters normal tissue architecture including cell shape and density [137]. Overall, these alterations in the ablated tissue have been found to increase optical scattering [72], [137]. These effects alone would suggest increased depolarization in RFA lesions, contrary to the observed depolarization reduction.

In addition to scattering, we must consider intrinsic tissue anisotropy which also contributes towards depolarization [17], [136]. It was suggested that intrinsic tissue anisotropy contributes to increased depolarization because linear retardance magnitude and orientation may be spatially inhomogeneous, changing in various tissue micro-domains. Polarized light that passes through these micro-domains of inhomogeneous anisotropy undergoes additional randomization, and consequently depolarization increases [138]. Based on the results of this current study, it appears that the contribution of tissue anisotropy towards depolarization was more dominant than changes in scattering. Indeed, Alali *et al.* determined that myocardium muscle exhibited much higher

depolarization compared to (for example) kidney cortex, despite the tissues having similar transport albedo (combination of both scattering and absorption), and suggested that tissue anisotropy may contribute to depolarization above and beyond the effect of transport albedo [17]. We posit that thermal coagulation caused by RF ablation results in loss of tissue anisotropy (supported by linear retardance findings), and a corresponding homogenization of the tissue morphology. This result in better preservation of incident light polarization, thus reduced depolarization.

Linear retardance arises when the refractive index of tissue is different in different spatial directions. Linear retardance is a depth-integrated measurement of the tissue's birefringent properties, and is indicative of asymmetric (aligned/anisotropic) structures. Healthy heart tissue is composed primarily of well-organized aligned cardiomyocytes, resulting in a directionally varying optical refractive index and hence strong linear retardance. The decreased linear retardance magnitude of the RFA lesions compared to the healthy regions (Figure 5-5b) indicates significant disruption of this ordered striated tissue architecture due to thermal damage of cardiomyocytes, with a corresponding loss of the underlying tissue anisotropy. The gradual increase in linear retardance magnitude from RFA core to healthy regions was likely due to reduced temperature rise in areas further away from the center of the lesion (RF catheter insertion point), resulting in better preservation of structural integrity in these regions, as confirmed by histology.

Interestingly, the orientation of linear retardance appears maintained in the RFA core. Closer examination of histopathology also revealed similar (circumferential) alignment of the damaged cardiomyocytes in the RF core region (Figure 5-6 and 5-7). This observed alignment may be due to a 'residual structural integrity' of myocytes, as supported by lower (but non-zero) retardance values in the RF core (Figure 5-5c). The thermal regime used in this study (RF power and ablation time) resulted in coagulative necrosis but not in complete destruction of structural integrity. Higher power settings and longer heating times would potentially result in relatively large thermal alterations of tissue structure and complete loss of fiber orientation. However, such aggressive thermal regimes are generally avoided in clinical ablation procedures, because they can induce gas formation (popping) and emboli [139].

Although linear retardance *magnitude* is greater throughout the healthy regions of the RFA sample 1 tissue in Figure 5-5, these values show more spatial variation than in the RFA treated region. At the same time, the linear retardance *orientation* throughout the healthy region is also less uniform (arrows in Figure 5-5c appear more random and chaotic). These results would suggest that RF ablation decreases anisotropy of the myocardium (indicated by its decreased linear retardance magnitude), but over a larger scale, the residual organization becomes more consistent. This behavior is somewhat perplexing and requires further investigation. A partial explanation may be that this is an indirect effect of the different scattering characteristics of the healthy vs. RFA tissue. Analogously, residual collagen in the RFA regions may contribute to a greater proportion to the observed linear retardance signal than it does in the healthy region. In other words, in addition to organizational changes, different biological constituents in the untreated and RF-ablated tissues may be causing the observed retardance (and depolarization) results. Finally, changes in fiber orientation with depth (axial heterogeneity) were not specifically investigated in this study. The presented polarimetry measurements are not depth-resolved *per se*, but rather represent cumulative polarization effects over the sampling depth (3-4 mm in most mammalian tissues) [12]. Indeed, we've began to quantify the effects of depth heterogeneity in the context of tissue polarimetry [89].

Mueller matrix polarimetry was able to distinguish between healthy and RF ablated myocardium tissue, similar to other optical techniques such as OCT [70]–[72] and photoacoustic imaging [73]. However, these studies were limited to binary discrimination of RFA lesions from healthy tissue [70]–[73] and the anatomically important 'rim region' with mixed viable and non-viable cells was not delineated and quantified. The current study demonstrated the ability of optical polarimetry to reveal differences between all three anatomically important regions (core, rim and healthy) of RF ablated tissue. Indeed, we will focus on quantitative segmentation of polarimetric images into these three regions in the next chapter. Further, the polarimetric segmentation results are compared and validated by histology.

A limitation of our study was that the myocardium tissue samples were fixed in formalin prior to polarimetric imaging study, as mentioned above. It has been observed

that both linear retardance magnitude and depolarization of the myocardium tissue increases following formalin fixation (~10% and 25% relative change, respectively) presumably from tissue organizational changes such as the crosslinking of proteins [91]. However, this did not limit our ability to see *differences* in the myocardium tissue arising from the thermal damage. Further, for comparison with histopathology slides, fixation is not an issue. That said, future studies should be done on fresh tissue, in preparation for clinical work.

Integration of Mueller matrix polarimetry into current clinical myocardium imaging systems could potentially provide supplementary information. Specifically, our previous studies have shown that the spatial extent of myocardial infarction can be sensitively demarcated non-invasively with optical polarimetry [86], [92]. Evaluation of RFA lesion extent, as demonstrated in this current study, would be another potential avenue for optical polarimetry of the myocardium. To enable such translation, the development of flexible fiber-based *in vivo* optical Mueller matrix probes is underway [140].

5.4 Summary

In this chapter, we demonstrated the potential of Mueller matrix polarimetry for the assessment of cardiac RF ablations. Specifically, changes in depolarization and linear retardance (magnitude and orientation) associated with structural damage due to myocardial RF ablation were successfully measured and quantified. Decreased depolarization and linear retardance magnitudes were observed in the core of the RFA lesion, with partial recovery in the rim region. Linear retardance orientation results were also quantified but were more difficult to interpret. Histology was used to investigate the underlying morphological changes caused by RFA and to help interpret the optical polarimetry signals. The findings suggest that the spatial extent of structural remodeling due to thermal-induced coagulative necrosis can be quantified by optical polarization maps, with potential future applications to evaluate RF lesion spatial extent.

6 Polarization Image Segmentation

6.1 Introduction

Radiofrequency ablation (RFA) is an effective treatment for patient management with focal arrhythmia, where properly titrated radiofrequency (RF) energy via intra-cardiac catheter enables controlled destruction of arrhythmogenic regions in myocardium via resistive tissue heating, creating a permanent lesion [60], [141]. The size and extent of RFA lesion within the targeted boundaries are the primary determinants to eliminate arrhythmogenic conduction and consequently define RFA efficacy [142].

Typically, the ablated tissue encompasses of a lesion core with coagulative necrosis surrounded by a partially ablated rim region that consists of mixed viable and non-viable cells [60], [61]. The rim region is often hard to differentiate with available imaging techniques but is essential to identify as the viable cells in this region might undo the desired “electric isolation” in the targeted area resulting in RFA treatment failure. Specifically, the currently available medical imaging modalities to clinicians (ultrasound, computed tomography, magnetic resonance, etc.) for RFA lesion assessment typically distinguish the RFA lesion core from healthy tissue, with the limitation that the important ‘rim region’ is relatively unexplored [64], [65].

A fast, sensitive and robust imaging system is certainly preferred for proper evaluation of RFA lesion. To this end, various optical imaging techniques have been investigated for the characterization and subsequent segmentation of cardiac RFA lesions. Recently quantitative evaluation of RFA lesion area by photoacoustic imaging resulted in about 69% area-agreement with gross pathology [73]. In addition, optical coherence tomography (OCT) has been explored for qualitative assessment of the RFA lesion spatial extent in RF ablated myocardium of swine model [70]–[72]. However, these emerging optical imaging techniques (like medical imaging mentioned above) are

so far focused to delineate the RFA core from the surrounding healthy tissue while ignoring the "sandwiched" rim region.

In Chapter 5, we have shown that polarized light measurements of total depolarization revealed significant differences ($p < 0.001$) between the RF core, rim and healthy regions of the RF ablation lesion indicating the capability of the technique to segment the RF ablated tissue in three zones; RFA core, rim region and healthy tissue. In this chapter, we extend the work presented in Chapter 5 and focus on quantitative analysis of polarization image segmentation in three zones. Specifically, the observed differences in total depolarization for the aforementioned three regions of RF ablated tissue will be exploited to segment the total depolarization image in three zones followed by quantitative comparison and validation from the corresponding histopathology image (ground truth) segmentation. It is noteworthy that the novelty of this work is twofold; first, the investigation of optical polarimetry for RFA lesion segmentation and second, the segmentation of the RFA lesion in *three* zones (as compared to previously studied binary segmentation [73]). We believe that the novel polarimetric image segmentation presented here would offer better visibility and delineation of the RF ablated tissue in the three zones and would provide prompt insights about the varying degree of thermal damage at various tissue locations.

6.2 Results

Images from a representative porcine myocardial septum sample with RF lesion (called RFA sample 2 hereafter) are presented in Figure. 6-1. It is noteworthy that different set of heating parameters were used for RF lesion generation in RFA sample 1 and sample 2, as mentioned in chapter 3. Specifically, RFA sample 2 received smaller amount of thermal energy as compared to RFA sample 1, resulting in relatively less thermal damage as can be seen in Figure 6-1. A magnified view of the region analyzed with optical polarimetry is shown in Figure. 6-1b. The core of the RFA lesion appears relatively darker (due to coagulative necrosis) as compared to the perimeter (which is due to hemorrhage) [60]. Masson's trichrome histology is shown in Figure. 6-1c, where the cytoplasm appears pink, nuclei are dark red, and collagen is stained blue. Histology revealed that the healthy myocardium is composed of well aligned parallel arrays of cardiomyocytes. Contrarily,

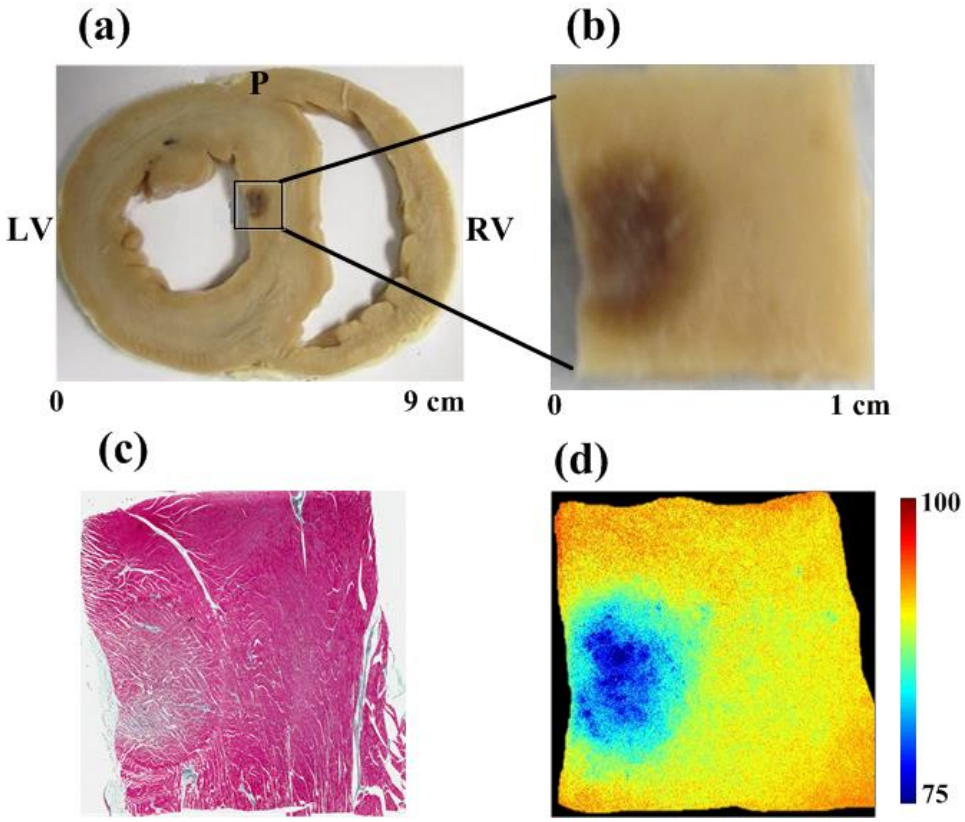

Figure 6-1 (a) White light photograph of gross myocardial tissue sample with RFA lesion, (b) magnified view of ROI from the sample analyzed with optical polarimetry, (c) Masson's trichrome histology, (d) total depolarization map of the region analyzed with optical polarimetry.

cardiomyocytes within the RFA core region suffered thermal insult with coagulative necrosis, as mentioned earlier. Structural alteration in cellular membrane and morphology were also observed. Nevertheless, it is noteworthy that the cardiomyocytes maintained some residual architecture. Total depolarization image of the RFA sample is shown in Figure. 6-1d. Reduced total depolarization values were observed in the RFA lesion compared to surrounding healthy tissue. Specifically, the decrease in total depolarization was prominent at the center of RFA lesion, and increased gradually towards healthy tissue at the remote periphery of the lesion. Although different set of heating parameters such as applied power, time, etc. were used for RFA lesion generation, these polarimetric changes are consistent with the trend observed for the RFA sample 1, presented and discussed in chapter 5.

Results for novel parametric optical maps of RF-ablated myocardium after segmenting the RF ablated tissue sample into RFA core lesion, rim, and healthy regions (from the sample shown in Figure 6-1) are presented in Figure 6-2. In particular, the computer assisted segmentation image of the total depolarization map (Figure 6-1d) using the local fuzzy thresholding algorithm (discussed in chapter 3) has been illustrated in Figure 6-2a. The RFA core, rim and healthy regions are represented by dark blue, cyan and yellow pseudo-colors, respectively. The black color represents the background. The ground truth, also called reference segmentation is obtained from the medical expert's (professor of histopathology) blind demarcation of RFA core and rim regions (indicated by the black contours) on the histology digital image (Figure 6-2b). The results for qualitative comparison between the two segmentation schemes are obtained by overlapping the two resultant images (Figure 6-1a and 6-1b) which demonstrate very good agreement.

For comparison, the segmentation results for the RFA sample 1 (Figure 5-4) has been shown in Figure 6-3. The computer assisted segmentation is shown in Figure 6-3a while the corresponding ground truth delineation results are presented in Figure 6-3b. The two segmentations schemes are compared by the overlapped image shown in Figure 6-3c. It is noteworthy that the reduced total depolarization at the vertical borders of the

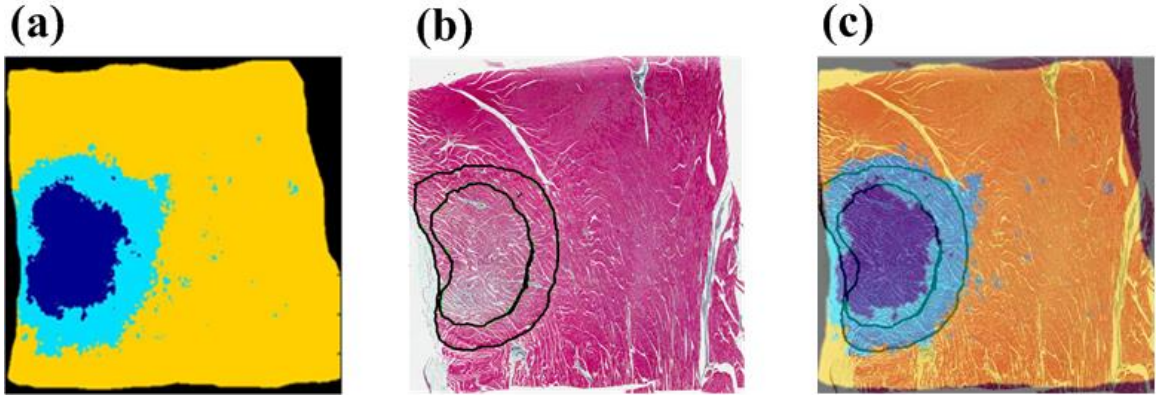

Figure 6-2 (a) Automated segmentation of the total depolarization map of RFA sample 2 using the local fuzzy thresholding algorithm, (b) ground truth segmentation, (c) overlapped images from (a) and (b).

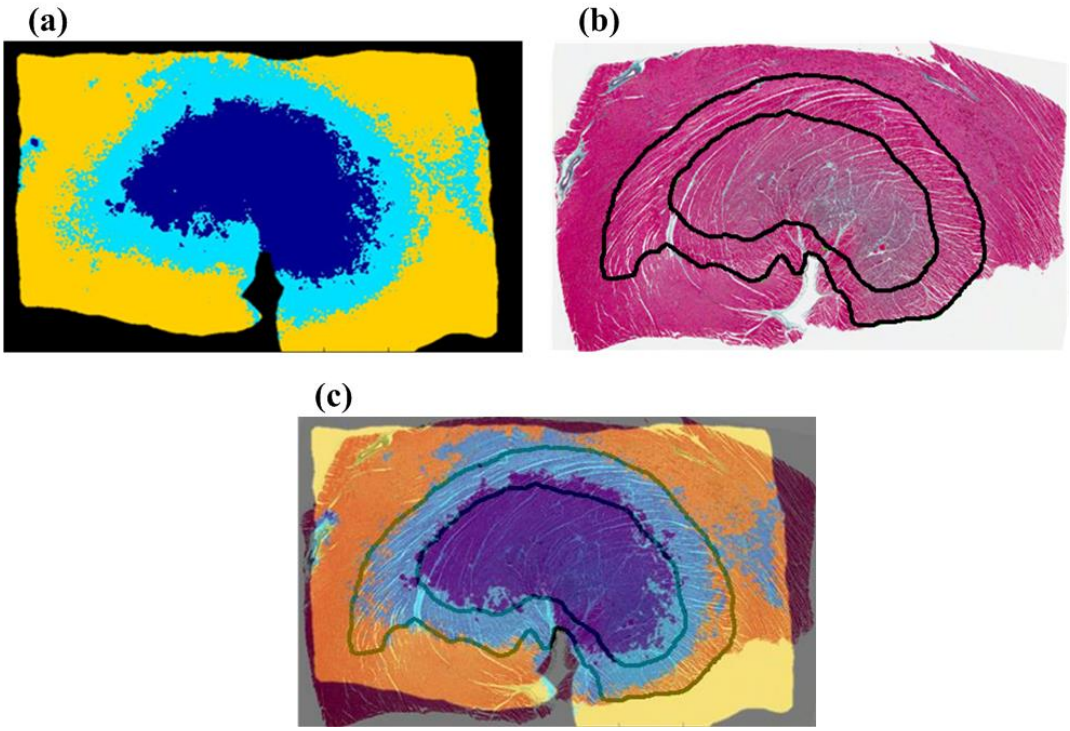

Figure 6-3 (a) Automated segmentation of the total depolarization map of RFA sample 1 using the local fuzzy thresholding algorithm, (b) ground truth segmentation shown as black contours, (c) overlapped images from (a) and (b).

RFA sample 1 (Figure 5-5a) was also *classified* as the 'rim region' by the automated algorithm, as indicated by the cyan color in Figure 6-3a. This is the consequence of somewhat lower than healthy depolarization at this position (Fig 4d), probably due to non-uniform thickness of the tissue caused by cutting procedure, or being compressed more at the edges of the sample holder. Nevertheless, this demonstrates the efficiency of the local fuzzy thresholding methodology for the depolarization image segmentation; Further, the tissue in the histology image has shrunken or may be sliced at an angle (right lower corner, in particular) during the histopathology slide preparation process. Specifically, the apparent damage in the RFA sample 1 may have occurred during tissue paraffin embedding, sectioning, fixing and/or staining.

Comprehensive assessment protocol was applied to evaluate/quantitative compare the expert-outlined (ground truth) segmentation and computer-aided segmentation results. DSC, sensitivity, specificity, and accuracy for both RFA core and rim region segmentations were calculated. These results are presented in Table 6.1 for five RF

ablated samples. The expert-outlined boundaries on the histopathology image were designated as "ground truth" while the computer-generated boundaries (based on observed total depolarization contrast in the three region of the ablated tissue) were called automated segmentation. DSC values, a representative of the spatial overlap between the ground truth and automated segmentation, for RFA core and rim regions for the myocardium apex sample (RFA sample 1; Figure. 5-4) were 0.76 and 0.82, while 0.80 and 0.77 for RFA sample 2, respectively which indicate a good agreement between the two segmentation schemes. Almost similar DSC values were found for other RFA samples analyzed (Table 6.1). These results suggest the consistency/ reproducibility of the segmentation based on the total depolarization. Sensitivity and specificity of the automated segmentation for the RFA core for the RFA sample 1 was 0.98 and 0.83 while 0.96 and 0.64 for the rim region. Further, segmentation accuracy values in the RFA core and rim region for the apex sample were 0.86 and 0.80, respectively.

Table 6.1 Dice similarity coefficient (DSC) for myocardial samples with RFA lesions, calculated from the ground truth histopathology demarcation and automated segmentation of total depolarization image

RFA Sample	RFA core				Rim region			
	DSC	S_n	S_p	*Acc*	*DSC*	S_n	S_p	*Acc*
1	0.76	0.98	0.83	0.86	0.82	0.96	0.64	0.80
2	0.80	0.89	0.96	0.95	0.77	0.95	0.85	0.88
3	0.79	0.72	0.84	0.79	0.81	0.78	0.51	0.68
4	0.77	0.83	0.47	0.70	0.80	0.99	0.99	0.57
5	0.76	0.73	0.72	0.73	0.82	0.86	0.62	0.62
Mean ± SD	0.78 ± 0.02	0.83 ± 0.1	0.79 ± 0.17	0.81 ± 0.09	0.81 ± 0.02	0.91 ± 0.08	0.72 ± 0.17	0.71 ± 0.12

6.3 Discussion

The purpose of this study was to quantitatively assess the efficacy of optical polarimetry for delineation of RF ablated tissue in various 'degrees' of thermal damage. Specifically, the differences in the polarization metric, total depolarization, in the RFA core, rim region and healthy tissue were exploited for segmentation of the total depolarization image in the aforesaid three zones using computer-aided methodology. The results obtained from the automated segmentation were compared and validated by the

corresponding ground truth demarcation on the histopathology images. The resultant computer-assisted segmentation of the total depolarization images of RF ablated tissue helped in visualizing the spatial extent and boundaries of the RF core and rim region and the subsequent quantification.

Unsupervised segmentation is a difficult but important part of medical image analysis. Fortunately, the local fuzzy thresholding algorithm for multi-region image segmentation employed here could be used to automatically segment the total depolarization image of RF ablated tissue in RFA core, rim region and healthy tissue, as indicated by the calculated evaluation parameters such as DSC, sensitivity, specificity, and accuracy. It is noteworthy that the same total depolarization image used here was also segmented in RFA core, rim region and healthy tissue, based on a different algorithm that exploits rigid global thresholds (results not shown). Global thresholding is based on the idea that the given image has multimodal (tri-modal in our case) histogram that can be exploited to separate different objects of the image using a threshold value. To this end, the mean depolarization values of the three regions were used as global thresholds for automated delineation of these zones. However, such segmentation failed to properly delineate the rim region as it substantially penetrates/ extents both into the core and healthy zones. Consequently, these results of global thresholding based algorithm were not acceptable clinically.

The boundary between RFA core and rim region is usually confounding making the perfect identification of RFA core and/or rim region a difficult task for both medical expert and automated segmentation algorithms (Figure 6-1d). Indeed, drawing the contour for the RFA core has been very subjective and subtle. Consequently, we elaborated the microscopic details of cardiomyocytes with the help of digital magnification (X 20) of histology image so that to properly assess the thermal damage and accordingly draw contours around the RFA core. Contradictorily, separating the rim region from the surrounding healthy tissue appeared significantly less challenging (particularly for RFA sample 1, as can be seen from Figure 5-6 and 5-7). Further, the spatial overlap of the segmented RFA core by both segmentation schemes was higher as

compared to the rim region, as indicated by the corresponding DSC values presented in Table 6.1.

On the other hand, an additional expert should counter analyze the demarcation from the medical expert such that the ground truth results are not always favored in comparison with automated segmentation. Indeed studies have shown significant intra- and inter- expert variability in outlining the particular lesion pathology [143]. Further, the intra-expert variability was lowest for the physician who produced the contours spending the most time [143]. Consequently, the performance of the computer-aided segmentation might not always fall below that of the medical expert (ground truth) due to the confounding boundary between the RFA core and rim region. However, this did not limit the ability of the automated segmentation to quantify and compare RFA core and rim regions and the preliminary segmentation results from this study are still promising. Furthermore, the information obtained from the automated segmentation method could potentially help pathologists, particularly those with limited time and experience, to identify the RFA rim region with greater accuracy. That said, future studies should be performed with a histopathologist and cardiologist as experts working together to define RFA core boundary based on their mutual consensus. In addition, future work should include the mean of ground truth demarcation from more than one pathology expert to reduce the intra-expert variations. This would allow subsequent quantitative analyses to more precisely compare the accuracy of automated segmentation methodology with that of ground truth.

Accurate segmentation and quantification of RFA lesion extent is essential for confirming the success of RFA treatment of cardiac focal arrhythmia. To this end, DSC appears to provide a better quantitative measure of the spatial overlap between the ground truth and automated segmentation; however, it is minimally used in such applications. Specifically, DSC quantifies how much the RFA core and rim regions intersect with the gold standard demarcation, which is important for determining the segmentation accuracy. Reasonably good agreement was observed between the two segmentation, especially for the important rim region as suggested by relatively higher mean DSC ~ 0.81. Sensitivity represents the probability that pixels at the RF ablated region are

correctly classified to belong to the ablated zone (i.e., true-positive). The automated segmentation of total depolarization image yielded significantly high mean sensitivity for both RFA core and rim region (0.83 and 0.91, respectively). Other evaluation metrics (specificity and accuracy) also indicated good agreement between the automated and ground truth segmentation. Collectively, these statistics illustrate the capability of total depolarization along with the local fuzzy thresholding methodology for segmenting the RF ablated tissue into RFA core, rim and healthy zones.

Previously, other optical techniques such as photoacoustic imaging [73] and OCT [71], [72] have been used for segmentation of RFA lesions. Although OCT has superior resolution and provides depth-resolved images, the past work focused only on qualitative assessment of RF lesion segmentation. Further, quantitative comparison of photoacoustic image segmentation with RFA lesion delineation on the white light photo of stained (nitro-tetrazolium blue) gross pathology (ground truth) showed 69% area agreement only. The "area agreement" was defined as the area of the segmentations intersection divided by the area of the segmentations union; this area agreement definition differs slightly from that of DSC. Recently, 3D optoacoustic imaging of RFA lesion in freshly excised porcine myocardial tissue has been explored to assess the lesion. Specifically, RFA lesion boundary was marked at locations where the optoacoustic signal exceeds an arbitrary threshold (chosen to be a 30% increase) from the original signal. The study claim "excellent agreement" between histology and optoacoustic images for size and geometry of the lesion without providing any quantitative evaluation metrics [144]. Further, acoustic radiation force impulse (ARFI) ultrasound imaging has been used for quantifying the dimensions of myocardial ablation lesions. Comparison of manual delineation of the lesion based on the visible discoloration of the tissue to automatic segmentations of the ARFI image resulted in maximum lateral and axial mean overlap of 68.7±5.21% and 66.3±8.4%; however, no specific definition/ explanation for the comparison metric "overlap" is provided [145]. The evaluation metrics used in these studies (area agreement, overlap, etc.) indicate that their one to one comparison to DSC (this study) may not be possible; however, it appears that DSC is a relatively better metric for such evaluation [146], [147]. More importantly, all these studies were limited to binary segmentation of RF ablated tissue (RFA core vs. healthy); these techniques could

not delineate the clinically important ‘rim region’. Contrastingly, the current study demonstrates the ability of total depolarization images for automatic quantitative segmentation in all three important regions (core, healthy, *and* rim).

It may be noted that the automated segmentation was performed on depolarization images obtained from measurements on thick (4mm) tissue samples while the ground truth segmentation was implemented on a thin histology slice (100 μm) from the same tissue sample; this might have contributed towards the slight misalignment of the two images as seen in the overlapping image (Figure 6-2c, 6-3c). Further, the histology processing (tissue paraffin embedding, sectioning, fixing, staining, etc.) also causes inevitable shrinking and slight change in shape of the tissue sample; consequently the tissue shapes between histology and polarimetry images do not perfectly agree as indicated by the *marker* structures such as vessels or characteristic gaps. Although, the tissue shrinkage issue has been addressed by equalizing the size of both histology and polarimetry images using a custom Matlab program; this may be considered as a limitation of this study. However, this issue demands a more robust approach in any future work so that the accuracy of overlap may be increased enabling greater agreement between the two segmentation schemes in terms of the quantitative metrics.

The polarimetry metrics reported here are the results of depth-integrated measurements, like almost all other polarimetric studies for biological tissues. Simulation results suggest that the average path length of polarization preserving photons for tissues in the visible spectrum is ~6 mm [148]; experimentally typical sampling depth is ~ 3–4 mm in most mammalian tissues [12]. Tissue depth within this limit can be resolved using a technique called spectral polarization difference imaging that exploits the difference in light penetration of different wavelengths [149].

For clinical translation, the development of a clinical intracardiac probe capable of concurrent RF ablation and polarimetric imaging will not be trivial. Indeed, such an integrated probe with combined RFA-optical coherence reflectometry catheters for real time assessment of RFA lesion has been recently reported [150]. Further, construction of optical polarimetric probes for in vivo studies has been considered by several groups [140]. If successful, such combined RFA-polarimetry probe will allow real time

characterization of RFA lesion resulting in a significant reduction in treatment failures. In summary, although depth resolution is a concern, optical polarimetric imaging shows promise to reliably characterize RFA lesions in clinical application in future.

6.4 Summary

This study demonstrates the potential of optical polarimetry for segmentation of cardiac RF ablation. Specifically, changes in total depolarization were successfully exploited to segment the image into RFA core, rim and healthy regions using local fuzzy thresholding algorithm. The automated segmentation results were validated by the ground truth segmentation obtained from the expert manual demarcation of RFA core and RFA rim regions on the histopathology image. Comparison metrics indicated good agreement between the automated and ground truth segmentations. The findings suggest that the potential of polarimetry images, combined with automatic objective segmentation, for visualization of the spatial extent of RFA core, rim region and healthy RFA myocardial tissue.

7 Conclusions and Future Perspectives

Polarized light have great potential for the assessment of pathological tissues. In this thesis, we have presented characterization of basal cell carcinoma (BCC) and radiofrequency ablated (RFA) tissues using Mueller matrix polarimetry. Computer assisted segmentation of RFA tissues were performed based on the differences in depolarization images. Brief summary of the research work presented in this thesis, the overall achievements and their potential applications are discussed in this chapter. Further, possible directions for the extension of this work are also identified and discussed.

7.1 Polarimetry Based Partial Least Square Classification

In this study, healthy and BCC human skin tissues were characterized with the help of Mueller matrix point measurement system. Tissue samples were collected from various patients through standard biopsy procedure for optical polarimetry measurements and histopathology analysis. The experimental Mueller matrix was decomposed via polar decomposition algorithm to extract the individual polarimetric properties for subsequent analysis.

Significant differences ($p < 0.001$) in the polarization properties of the healthy and BCC tissue groups were observed. The predominant polarization effects of biological tissues were depolarization, retardance, and diattenuation. Depolarization of BCC group was significantly lower as compared to the healthy group indicating towards the underlying morphological changes caused by BCC. Further, it was observed that the linear polarization states were better preserved than circular polarization states in both healthy and BCC tissue groups indicating that the scattering of incident light by the tissues lies in the framework of Rayleigh scattering. In addition to depolarization, significant differences ($p < 0.001$) in retardance and diattenuation were also observed.

Wilks lambda illustrated that all measured polarimetric properties except circular diattenuation are good candidates for the computer-assisted discrimination of normal and BCC skin tissue samples. Indeed, the PLS analysis based on the polarization properties of the healthy and BCC tissues resulted in 100% classification sensitivity, specificity and accuracy. However, we suggest that the depolarization being the most dominant polarization effect in biological tissues and exhibit relatively large differences in the two tissue groups appears potentially capable for efficient computer-aided classification. Overall, we conclude that optical polarimetry coupled with PLS discrimination seems potentially convincing for tissue classification based on their inherent contrast in polarimetric properties [151].

7.2 Polarization Imaging of Porcine Myocardial Tissue

We have demonstrated the potential of Mueller matrix imaging polarimetry for the assessment of cardiac RFA lesions. Ablation lesions were generated in porcine myocardium tissue using intra-cardiac RF catheter. The spatial extent of the RF lesion including the RFA core, rim and healthy regions was analyzed with Mueller matrix imaging system. Significant differences in polarimetric properties of the aforementioned zones were observed. Specifically, the total depolarization was significantly lower at the RFA core ($p < 0.01$) compared to the healthy region with intermediate values at the rim region. Likewise, linear retardance was significantly lower in the core and rim regions compared to healthy regions ($p < 0.05$). It is noteworthy that the linear retardance orientation results were also quantified but were more difficult to interpret. Further, the changes in depolarization and linear retardance (magnitude and orientation) were associated with the structural damage of myocardial tissue due to RF ablation. Cardiomyocytes within the RFA core region suffered thermal insult with coagulative necrosis. Histology with Masson trichrome and H&E staining was used to investigate the underlying morphological changes caused by RFA and to help interpret the optical polarimetry signals. It was observed that the cellular membrane and morphology were structurally altered but maintained some residual architecture. Histological staining also showed a dark-reddish hue with black zones presumably due to myoglobin denaturation. Further, close examination of collagen fibers revealed evidence of thermal damage with

broken strands and random orientations. Unlike collagen in the healthy region of the myocardium, the collagen strands in the RFA lesion appear 'wavy'. All these microscopic alterations appear as markers of extensive thermal damage. Differences in polarimetric parameters at the three zones of the RFA lesion were correlated /validated to these microstructural changes observed with histology. The findings suggest that the spatial extent of structural remodeling due to thermal-induced coagulative necrosis can be quantified by optical polarization maps, with potential future applications to evaluate RF lesion spatial extent [11].

7.3 Polarization Image Segmentation

We have shown that optical polarimetry is capable to characterize the spatial extent of a typical myocardial RFA lesion, with significantly lower ($p< 0.01$) total depolarization at the necrotic core compared to the healthy tissue while intermediate values at the rim region. These measured differences in depolarization were exploited to segment the RF ablated tissue in the aforementioned three zones (i.e. RFA core, rim and healthy). Local fuzzy thresholding algorithm was employed for computer-aided multi-region segmentation of the total depolarization image. The corresponding digital histopathology image was manually delineated into RFA core and rim regions by medical expert to obtain the ground truth (reference) segmentation. The two segmentation schemes were quantitatively compared. Different validation metrics such as dice similarity coefficient (DSC), sensitivity, specificity and accuracy were used to evaluate the performance and efficiency of the computer-assisted segmentation. These evaluation metrics illustrated good agreement between the two segmentation schemes. We believe that the resultant novel polarimetric image segmentation would offer better visual delineation of the RF ablated tissue in the three zones and would provide prompt insight about the varying degree of thermal damage at various tissue locations.

7.4 Future Perspectives

The investigations presented in this dissertation successfully demonstrated polarized light measurement for the characterization of pathological conditions of biological tissue

samples. Mueller matrix analysis of the experimental data provided greater insight for the quantification and explanation of the differences in individual polarization properties of healthy and structurally damaged tissues. The analysis of polarimetric images for automated segmentation into various zones of clinical interest provided novel parametric maps. We believe that these studies will help researchers in providing better understanding of the underlying biophysics involved in explaining polarized light-tissue interactions. Further, the novel computer-aided optical image segmentation has opened new research avenues. Nevertheless, there is still much to be done for implementing the optical polarimetry in clinics. We discuss some ongoing projects, outline emerging improvements, and speculate on its future perspectives in biomedical optics.

For biological tissues, Mueller matrix contains the complete set of polarimetric properties in an intermixed fashion. There are different decomposition methods for separation and quantification of individual polarization properties. The Lu-Chipman polar methodology for decomposing Mueller matrix used in this dissertation is based on the assumption that the polarimetric effects are occurring sequentially, which is not strictly true. In reality, all the polarization effects are occurring simultaneously [152]. The ambiguities in derived polarization properties stemming from this assumption are reflected in the non-commutative nature of the basis matrix multiplication of polar decomposition. Consequently, the Lu-Chipman decomposition has been modified for better description of individual polarization metrics. Specifically, pseudo-polar and extended polar decomposition has been recently coined to overcome the above mentioned shortcoming of polar decomposition [96]. However, these modified decomposition schemes are rather computationally extensive. Further, additional algorithms for decoupling of Mueller matrix such as symmetric and differential decomposition have been introduced recently [93], [95]. Each of these decoupling method have their specific merits and demerits, a comparative study of all these decomposition algorithms towards the more robust scheme would be really interesting for many biomedical applications. Indeed, we have begun working on such comparative study.

Typically, any biological tissue represent a strongly scattering model due to the complex patterns of refractive index variations resulting from tissue parameters like

scatterer (cells, nuclei, connective tissue fibers, etc.) size, shape, and density. Consequently, the collected light signal after interaction with biological tissue is considerably depolarized having significantly low signal-to-noise ratio (SNR) for polarimetric information. To this end, the optical measurement system should be capable to sense small polarization changes. The optical polarization systems used in this dissertation have different measurement sensitivities. Specifically, the polarimetric point measurement system is highly sensitivity but needs time consuming procedures (point-by-point scanning). The polarimetric imaging system is capable to examine large areas of biological tissues with less sensitivity. However, with the advancement of technology and improvement in design, we are witnessing the possibility of more sensitive, robust, fast and accurate polarimetric systems. For instance, ongoing research is focused on advance optical systems capable of generating various polarization states without involvement of any mechanically moving parts. Specifically, the polarization states could be generated electronically by photoelastic modulators (PEMs) [153] or liquid crystals (LCs) [154], and by diffraction using gratings [155], polarizing prisms, or graded index lenses [156]. Such systems are capable of imaging in much smaller time scale (milliseconds) with significantly higher sensitivity and would hopefully lead to the next generation optical polarimetry systems in the near future.

Presently, most polarized light measurement systems are limited to *ex vivo* assessment of biological tissues, as shown in this dissertation. Further, optical polarimetry is also used occasionally for intraoperative characterization of excised tissues. However, the ultimate goal of these studies would be the integration of optical polarimetry into clinical settings. To this end, application of optical polarimetry to various pathologies in dermatology would represent the simplest *in vivo* models. However, not surprisingly the polarized light delivery and pick up from the deep seated body organs would probably appear the primary challenge to enable such translation. To address this issue, the development of flexible fiber-based *in vivo* optical polarimetry probes is underway by many groups [140].

The presumably challenging part of the proposed probe for polarized light delivery/collection is the distortion of the polarization states of light during transit that

can potentially introduce radical artifacts in low SNR light signals. One proposed solution to this problem is the adaptation of so-called distal polarization components (polarizers only) that enables accurate generation and collection of the polarized light [157]. Recently, another interesting solution has been proposed to the above mentioned problem; the utilization of polarization maintaining fibers for both the delivery and collection of polarized light [158]. With these novel advances in optical polarimetric systems, it appears that this technique would be available for clinical application (in vivo measurements) in near future.

Non-linear microscopy (NLM) is an ideal tool for understanding cardiac tissue and its related pathologies. The two main nonlinear signals from the given tissue sample are second harmonic generation (SHG) and two-photon excited auto-fluorescence (TPEF) [159]. When excited by a suitable ultra-short pulse laser source, cardiomyocytes generate TPFE signal while SHG signal arises from the intervening collagen fibers enabling both qualitative and quantitative evaluation of the underlying cardiac tissue. The relatively high depth penetration of NLM signal (few hundred micrometers) provides the added benefit for three-dimensional cardiac tissue assessment. We therefore suggest NLM microscopy for characterization of RF ablated cardiac tissues. Specifically, co-registered visualization, through TPEF and SHG of both cardiomyocytes and collagen in healthy and RFA myocardium would provide insight to ablation lesion in terms of tissue organization. Further, such study would also help better understanding of the polarimetric findings presented in this dissertation.

We have shown that optical polarimetry have the potential to map cardiac fiber organization. Specifically, the direction of linear retardance was exploited to image cardiac fiber orientation in both healthy and RF ablated myocardial tissues. Further, these results were validated with the help of Masson trichrome histology. In addition, diffusion tensor MR imaging (dtMRI) has been frequently used for measuring tissue anisotropy (both magnitude and direction) based on water diffusivity in tissue. Consequently, the optical polarimetric and dtMRI results could be directly compared in biological model of interest such as myocardium [92]. We therefore suggest future studies for comparing the two techniques and highlighting the possible technique-specific differences. Further, such

combined study of structurally damaged (like RF ablated) tissue would possibly shed more light on the correlation of ablation lesion and myocardial fiber orientation under different conditions. This work will have great clinical importance for assessment of electrical conduction in RFA lesions, particularly at the rim region.

8 References

[1] R. C. JONES, “A New Calculus for the Treatment of Optical Systems,” *J. Opt. Soc. Am.*, vol. 31, no. 7, p. 488, Jul. 1941.

[2] G. G. Stokes, “On the composition and resolution of streams of polarized light from different sources,” *Trans. Cambridge Philos. Soc.*, vol. 9, p. 399, 1851.

[3] M. Josef and E. W. Thulstrup, *Spectroscopy with Polarized Light*. New York: VCH, 1995.

[4] D. S. Kliger and J. W. Lewis, *Polarized Light in Optics and Spectroscopy*. New York: Academic Press–Harcourt Brace Jovanovich, 1990.

[5] R. A. Hegstorm and D. K. Kondepudi, “The handedness of the universe,” *Sci. Am.*, vol. 262, pp. 108–115, 1990.

[6] C. A. Browne and F. W. Zarban, *Physical and chemical methods of sugar analysis*. New York: Wiley, 1941.

[7] B. Jirgensons, *Optical rotatory dispersion of proteins and other macromolecules*. New York, 1969.

[8] C. Brosseau, *Fundamentals of polarized light : A statistical optics approach*. New York: Wiley, 1998.

[9] M. GADSDEN, P. ROTHWELL, and M. J. TAYLOR, “Detection of circularly polarised light from noctilucent clouds,” *Nature*, vol. 278, no. 5705, pp. 628–629, Apr. 1979.

[10] A. Chrysostomou, P. W. Lucas, and J. H. Hough, “Circular polarimetry reveals helical magnetic fields in the young stellar object HH 135-136,” *Nature*, vol. 450, no. 7166, pp. 71–73, Nov. 2007.

[11] I. Ahmad, A. Gribble, M. Ikram, M. Pop, and A. Vitkin, “Polarimetric assessment of healthy and radiofrequency ablated porcine myocardial tissue,” *J. Biophotonics*, vol. 10, pp. 1–10, 2015.

[12] N. Ghosh and I. A. Vitkin, “Tissue polarimetry: concepts, challenges, applications, and outlook,” *J Biomed Opt.*, vol. 16, no. 11, p. 110801, Nov. 2011.

[13] I. Ahmad, M. Ahmad, K. Khan, S. Ashraf, S. Ahmad, and M. Ikram, “Ex vivo characterization of normal and adenocarcinoma colon samples by Mueller matrix polarimetry,” *J. Biomed. Opt.*, vol. 20, no. 5, p. 56012, May 2015.

[14] S. Manhas, M. K. Swami, P. Buddhiwant, N. Ghosh, P. K. Gupta, and J. Singh, “Mueller matrix approach for determination of optical rotation in chiral turbid media in backscattering geometry,” *Opt. Express*, vol. 14, no. 1, pp. 190–202, Jan. 2006.

[15] M. F. G. Wood, X. Guo, and I. A. Vitkin, “Polarized light propagation in multiply scattering media exhibiting both linear birefringence and optical activity : Monte Carlo model and experimental methodology,” *J. Biomed. Opt.*, vol. 12, no. 1, pp. 1–10, 2013.

[16] X. Guo, M. F. G. Wood, N. Ghosh, and I. A. Vitkin, “Depolarization of light in turbid media : a scattering event resolved Monte Carlo study,” *Appl. Opt.*, vol. 49, no. 2, pp. 153–162, 2010.

[17] S. Alali, M. Ahmad, A. Kim, N. Vurgun, M. F. Wood, and I. A. Vitkin, “Quantitative correlation between light depolarization and transport albedo of various porcine tissues,” *J Biomed Opt.*, vol. 17, no. 4, p. 045004, Apr. 2012.

[18] D. Bicout, C. Brosseau, A. S. Martinez, and J. M. Schmitt, "Depolarization of multiply scattered waves by spherical diffusers: Influence of the size parameter," *Phys. Rev. E*, vol. 49, no. 2, pp. 1767–1770, 1994.

[19] J. Schmitt, A. Gandjbakhche, and R. Bonner, "Use of polarized light to discriminate short-path photons in a multiply scattering medium," *Appl. Opt.*, vol. 31, no. 30, pp. 6535–46, 1992.

[20] A. D. Kim and M. Moscoso, "Influence of the relative refractive index on the depolarization of multiply scattered waves," *Phys. Rev. E*, vol. 64, no. 2, p. 026612, 2001.

[21] V. Sankaran, J. T. Walsh, and D. J. Maitland, "Polarized light propagation through tissue phantoms containing densely packed scatterers," *Opt. Lett.*, vol. 25, no. 4, pp. 239–241, 2000.

[22] V. Sankaran, M. J. Everett, D. J. Maitland, and J. T. Walsh, "Comparison of polarized-light propagation in biological tissue and phantoms," *Opt. Lett.*, vol. 24, no. 15, pp. 1044–1046, 1999.

[23] N. Ghosh, H. S. Patel, and P. K. Gupta, "Depolarization of light in tissue phantoms - effect of a distribution in the size of scatterers," *Opt. Express*, vol. 11, no. 18, pp. 2198–205, 2003.

[24] V. Sankaran, J. T. Walsh, and D. J. Maitland, "Comparative study of polarized light propagation in biologic tissues," *J. Biomed. Opt.*, vol. 7, no. 3, pp. 300–6, Jul. 2002.

[25] A. Pierangelo, A. Benali, M.-R. Antonelli, T. Novikova, P. Validire, B. Gayet, and A. De Martino, "Ex-vivo characterization of human colon cancer by Mueller polarimetric imaging," *Opt. Express*, vol. 19, no. 2, pp. 1582–93, Jan. 2011.

[26] A. Pierangelo, A. Nazac, A. Benali, P. Validire, H. Cohen, T. Novikova, B. H. Ibrahim, S. Manhas, C. Fallet, R. Antonelli, and A. Martino, "Polarimetric imaging of uterine cervix : a case study," *Opt Express*, vol. 21, no. 12, pp. 281–289, 2013.

[27] W. Wang, L. G. Lim, S. Srivastava, J. S. B. Yan, A. Shabbir, and Q. Liu, "Roles of linear and circular polarization properties and effect of wavelength choice on differentiation between ex vivo normal and cancerous gastric samples," *J. Biomed. Opt.*, vol. 19, no. 4, p. 046020, Apr. 2014.

[28] P. Shukla, A. Awasthi, P. K. Pandey, and A. Pradhan, "Discrimination of normal and dysplasia in cervix tissue by Mueller matrix analysis," in *SPIE Conference*, 2008, vol. 6864, pp. 1–8.

[29] T. M. Johnson, S. Carpenter, A. Guerra, T. Aida, and J. P. Freyer, "Polarized angular dependent spectroscopy of epithelial cells and epithelial cell nuclei to determine the size scale of scattering structures," *J. Biomed. Opt.*, vol. 7, no. 3, pp. 378–387, 2002.

[30] S. L. Jacques, J. R. Roman, and K. Lee, "Imaging superficial tissues with polarized light," *Lasers Surg. Med.*, vol. 26, no. 2, pp. 119–29, Jan. 2000.

[31] Y. Liu, Y. L. Kim, X. Li, and V. Backman, "Investigation of depth selectivity of polarization gating for tissue characterization," *Opt. Express*, vol. 13, no. 2, pp. 601–611, 2005.

[32] S. G. Demos and R. R. Alfano, "Temporal gating in highly scattering media by the degree of optical polarization," *Appl. Opt.*, vol. 21, no. 2, pp. 161–163, 1996.

[33] M. Gu, "Image reconstruction through turbid media under a transmission-mode microscope," *J. Biomed. Opt.*, vol. 7, no. 3, pp. 372–377, 2002.

[34] S. Jacques, J. C. Ramella-Roman, and K. Lee, "Imaging skin pathology with polarized light," *J. Biomed. Opt.*, vol. 7, no. 3, pp. 329–40, Jul. 2002.

[35] S. L. Jacques, R. Samatham, S. Isenhath, and K. Lee, “Polarized light camera to guide surgical excision of skin cancers,” in *SPIE Conference*, 2008, vol. 6842, pp. 684201–07.

[36] Y. Liu, Y. L. Kim, and V. Backman, “Development of a bioengineered tissue model and its application in the investigation of the depth selectivity of polarization gating,” *Appl. Opt.*, vol. 44, no. 12, pp. 2288–99, 2005.

[37] M. F. Wood, N. Ghosh, M. A. Wallenburg, S. H. Li, R. D. Weisel, B. C. Wilson, R. K. Li, and I. A. Vitkin, “Polarization birefringence measurements for characterizing the myocardium, including healthy, infarcted, and stem-cell-regenerated tissues,” *J Biomed. Opt.*, vol. 15, no. 4, p. 047009, 2010.

[38] S. Alali, K. J. Aitken, A. Schröder, A. Gribble, D. J. Bagli, and I. A. Vitkin, “Assessment of local structural disorders of the bladder wall in partial bladder outlet obstruction using polarized light imaging,” *Biomed. Opt. Express*, vol. 5, no. 2, pp. 621–629, 2014.

[39] H. Chung, T. Dai, S. K. Sharma, Y.-Y. Huang, J. D. Carroll, and M. R. Hamblin, “The nuts and bolts of low-level laser (light) therapy,” *Ann. Biomed. Eng.*, vol. 40, no. 2, pp. 516–533, 2013.

[40] D. de F. T. da Silva, B. de C. Vidal, D. M. Zezell, T. M. T. Zorn, and S. C. M. S. R. Núñez, “Collagen birefringence in skin repair in response to red polarized-laser therapy,” *J. Biomed. Opt.*, vol. 11, no. 2, p. 024002, 2006.

[41] P. Whittaker, S. Zheng, M. J. Patterson, R. A. Kloner, K. E. Daly, and R. A. Hartman, “Histologic signatures of thermal injury : applications in transmyocardial laser revascularization and radiofrequency ablation,” *Lasers Surg. Med.*, vol. 27, pp. 305–318, 2000.

[42] J. F. De Boer, S. M. Srinivas, A. Malekafzali, Z. Chen, and J. S. Nelson, "Imaging thermally damaged tissue by polarization sensitive optical coherence tomography," *Opt. Express*, vol. 3, no. 6, pp. 212–218, 1998.

[43] S. Zotter, M. Pircher, G. Erich, T. Torzicky, H. Yoshida, F. Hirose, S. Holzer, J. Kroisamer, C. Vass, U. Schmidt-erfurth, and C. K. Hitzenberger, "Measuring retinal nerve fiber layer birefringence, retardation, and thickness using wide-field, high-speed polarization sensitive spectral domain OCT," *Invest. Ophthalmol. Vis. Sci.*, vol. 54, no. 1, pp. 72–84, 2013.

[44] V. Backman, R. Gurjar, K. Badizadegan, I. Itzkan, R. R. Dasari, L. T. Perelman, and M. S. Feld, "Polarized light scattering spectroscopy for quantitative measurement of epithelial cellular structures in situ," *IEEE J. Sel. Top. Quantum Electron.*, vol. 5, no. 4, pp. 1019–1026, 1999.

[45] M. Bartlett, G. Huang, L. Larcom, and H. Jiang, "Measurement of particle size distribution in mammalian cells in vitro by use of polarized light spectroscopy," *Appl. Opt.*, vol. 43, no. 6, pp. 1296–307, 2004.

[46] J. R. Mourant, T. M. Johnson, and J. P. Freyer, "Characterizing mammalian cells and cell phantoms by polarized backscattering fiber-optic measurements," *Appl. Opt.*, vol. 40, no. 28, pp. 5114–23, 2001.

[47] A. Kyrgidis, T. G. Tzellos, K. Vahtsevanos, and S. Triaridis, "New concepts for basal cell carcinoma. Demographic, clinical, histological risk factors, and biomarkers. A systematic review of evidence regarding risk for tumor development, susceptibility for second primary and recurrence," *J. Surg. Res.*, vol. 159, no. 1, pp. 545–556, 2010.

[48] A. Garcia-Uribe, N. Kehtarnavaz, G. Marquez, V. Prieto, M. Duvic, and L. V Wang, "Skin cancer detection by spectroscopic oblique-incidence reflectometry: classification and physiological origins," *Appl. Opt.*, vol. 43, no. 13, pp. 2643–50, May 2004.

[49] L. M. McIntosh, R. Summers, M. Jackson, H. H. Mantsch, J. R. Mansfield, M. Howlett, a N. Crowson, and J. W. Toole, “Towards non-invasive screening of skin lesions by near-infrared spectroscopy,” *J. Invest. Dermatol.*, vol. 116, no. 1, pp. 175–81, Jan. 2001.

[50] S. Sigurdsson, P. A. Philipsen, L. K. Hansen, J. Larsen, M. Gniadecka, and H. C. Wulf, “Detection of skin cancer by classification of Raman spectra,” *IEEE Trans. Biomed. Eng.*, vol. 51, no. 10, pp. 1784–93, Oct. 2004.

[51] M. Gniadecka, P. A. Philipsen, S. Sigurdsson, Ã. S. Wessel, O. F. Nielsen, D. H. Christensen, J. Hercogova, K. Rossen, K. Thomsen, L. K. Hansen, and H. C. Wulf, “Melanoma Ddiagnosis by Raman spectroscopy and neural networks : structure alterations in proteins and lipids in intact cancer tissue,” *J. Invest. Dermatol.*, pp. 443–449, 2004.

[52] Y. Zhao, L. Zhang, and Q. Pan, “Spectropolarimetric imaging for pathological analysis of skin,” *Appl. Opt.*, vol. 48, no. 10, pp. D236–46, Apr. 2009.

[53] S. L. Jacques, “Spectral imaging and analysis to yield tissue optical properties,” *J. Innov. Opt. Health Sci.*, vol. 2, no. 2, pp. 123–129, 2009.

[54] A. Rehman, I. Ahmad, K. Rehman, S. Anwar, S. Firdous, and M. Nawaz, “Optical properties measurement of highly diffusive tissue phantoms for biomedical applications,” *Laser Phys.*, vol. 25, no. 2, p. 025605, Feb. 2015.

[55] M. C. Pierce, J. Strasswimmer, B. H. Park, B. Cense, and J. F. De Boer, “Birefringence measurements in human skin using polarization-sensitive optical coherence tomography,” *J. Biomed. Opt.*, vol. 9, no. 2, pp. 287–291, 2004.

[56] “World Health Organization,” *Cardiovascular diseases*. [Online]. Available: http://www.who.int/mediacentre/factsheets/fs317/en/. [Accessed: 02-Apr-2015].

[57] A. Kléber and Y. Rudy, “Basic mechanisms of cardiac impulse propagation and associated arrhythmias,” *Physiol. Rev.*, vol. 84, no. 2, pp. 431–488, 2004.

[58] T. A. Quinn, “The importance of non-uniformities in mechano-electric coupling for ventricular arrhythmias,” *J. Interv. Card. Electrophysiol.*, vol. 39, no. 1, pp. 25–35, 2014.

[59] O. J. Eick, “Temperature controlled radiofrequency ablation,” *Indian Pacing Electrophysiol. J.*, vol. 2, no. 3, pp. 66–73, 2002.

[60] S. Thomsen, “Mapping of thermal injury in biologic tissues using quantitative pathologic techniques,” in *SPIE Conference*, 1999, vol. 3594, pp. 82–95.

[61] A. C. Lardo, E. R. McVeigh, P. Jumrussirikul, R. D. Berger, H. Calkins, J. Lima, and H. Halperin, “Visualization and temporal / spatial characterization of cardiac radiofrequency ablation lesions using magnetic resonance imaging,” *Circulation*, vol. 102, no. 6, pp. 698–705, 2000.

[62] E. E. Girard, A. Al-Ahmad, J. Rosenberg, R. Luong, T. Moore, G. Lauritsch, J. Boese, and R. Fahrig, “Contrast-enhanced cardiac C-arm CT evaluation of radiofrequency ablation lesions in the left ventricle,” *JACC Cardiovasc Imaging*, vol. 4, no. 3, pp. 259–268, 2011.

[63] J. M. Kalman, A. P. Fitzpatrick, J. E. Olgin, M. C. Chin, R. J. Lee, M. M. Scheinman, and M. D. Lesh, “Biophysical characteristics of radiofrequency lesion formation in vivo: dynamics of catheter tip-tissue contact evaluated by intracardiac echocardiography,” *Am. Heart J.*, vol. 133, no. 1, pp. 8–18, Jan. 1997.

[64] J. M. Kalman, J. Jue, K. Sudhir, P. Fitzgerald, P. Yock, and M. D. Lesh, “In vitro quantification of radiofrequency ablation lesion size using intracardiac echocardiography in dogs,” *Am J Cardiol.*, vol. 77, no. 2, pp. 217–219, Jan. 1996.

[65] H. L. Fred, “Drawbacks and limitations of computed tomography,” *Tex Hear. Inst J.*, vol. 31, no. 4, pp. 345–348, 2004.

[66] A. Stys and T. Stys, “Current clinical applications of heart rate variability,” *Clin. Cardiol.*, vol. 21, no. 10, pp. 719–724, 1998.

[67] M. Pop, M. Sermesant, J. Peyratt, E. Crystal, A. Dick, and G. Wright, "Anatomic reentry : insights from a parametric study on a simple 3D anisotropic wedge wodel," *Int. J. Bioelectromagn.*, vol. 12, no. 3, pp. 133–151, 2010.

[68] F. H. M. Wittkampf, D. Ph, H. Nakagawa, and D. Ph, "RF catheter ablation : lessons on lesions," *Pacing Clin. Electrophysiol.*, vol. 29, no. 11, pp. 1285–1297, 2006.

[69] S. Willems, X. Chen, H. Kottkamp, G. Hindricks, W. Haverkamp, B. Rotman, M. Shenasa, G. Breithardt, and M. Borggrefe, "Temperature-controlled radiofrequency catheter ablation of manifest accessory pathways," *Eur. Heart J.*, vol. 17, no. 3, pp. 445–452, 1996.

[70] J. F. De Boer, S. Srinivas, A. Malekafzali, Z. Chen, and J. Nelson, "Imaging thermally damaged tissue by polarization sensitive optical coherence tomography," *Opt Express*, vol. 3, no. 6, pp. 212–218, 1998.

[71] C. P. Fleming, H. Wang, K. J. Quan, and A. M. Rollins, "Real-time monitoring of cardiac radio-frequency ablation lesion formation using an optical coherence tomography forward-imaging catheter," *J Biomed Opt.*, vol. 15, no. 3, p. 030516, 2010.

[72] C. P. Fleming, K. J. Quan, H. Wang, G. Amit, and A. M. Rollins, "In vitro characterization of cardiac radiofrequency ablation lesions using optical coherence tomography," *Opt Express*, vol. 18, no. 3, pp. 3079–3092, 2010.

[73] N. Dana, L. Di Biase, A. Natale, S. Emelianov, and R. Bouchard, "In vitro photoacoustic visualization of myocardial ablation lesions," *Hear. Rhythm.*, vol. 11, no. 1, pp. 150–157, 2014.

[74] C. P. Fleming, K. J. Quan, and A. M. Rollins, "Toward guidance of epicardial cardiac radiofrequency ablation therapy using optical coherence tomography," *J. Biomed. Opt.*, vol. 15, no. 4, p. 041510, 2010.

[75] J. F. De Boer and T. E. Milner, “Review of polarization sensitive optical coherence tomography and Stokes vector determination,” *J. Biomed. Opt.*, vol. 7, no. 3, pp. 359–371, 2002.

[76] K. Schoenenberger, B. W. Colston, D. J. Maitland, L. B. Da Silva, and M. J. Everett, “Mapping of birefringence and thermal damage in tissue by use of polarization-sensitive optical coherence tomography,” *Appl. Opt.*, vol. 37, no. 25, pp. 6026–6036, 1998.

[77] M. A. Wallenburg, J. Wu, R. K. Li, and I. A. Vitkin, “Two-photon microscopy of healthy, infarcted and stem-cell treated regenerating heart,” *J Biophotonics.*, vol. 4, no. 5, pp. 297–304, May 2011.

[78] M. F. G. Wood and I. A. Vitkin, “Mueller matrix decomposition for extraction of individual polarization parameters from complex turbid media exhibiting multiple scattering , optical activity , and linear birefringence,” *J. Biomed. Opt.*, vol. 13, no. 4, p. 044036, 2008.

[79] N. Ghosh, M. F. G. Wood, and I. A. Vitkin, “Polarimetry in turbid, birefringent, optically active media: A Monte Carlo study of Mueller matrix decomposition in the backscattering geometry,” *J. Appl. Phys.*, vol. 105, no. 10, p. 102023, 2009.

[80] R. C. JONES, “New Calculus for the Treatment of Optical Systems VIII Electromagnetic Theory,” *J. Opt. Soc. Am.*, vol. 46, no. 2, p. 126, Feb. 1956.

[81] R. C. JONES, “A New Calculus for the Treatment of Optical Systems VII Properties of the N-Matrices,” *J. Opt. Soc. Am.*, vol. 38, no. 8, p. 671, Aug. 1948.

[82] R. C. JONES, “A New Calculus for the Treatment of Optical Systems IV,” *J. Opt. Soc. Am.*, vol. 32, no. 8, p. 486, Aug. 1942.

[83] R. C. Jones, “A new calculus for the treatment of optical systems V A more general formulation, and description of another calculus,” *J. Opt. Soc. Am.*, vol. 37, no. 2, p. 107, Feb. 1947.

[84] E. Wolf, “Coherence properties of partially polarized electromagnetic radiation,” *Nuovo Cim.*, vol. 13, no. 6, pp. 1165–1181, Sep. 1959.

[85] D. H. Goldstein, *Polarized Light*, 2nd Edi. CRC Press, 2011.

[86] M. A. Wallenburg, M. F. G. Wood, N. Ghosh, and I. A. Vitkin, “Polarimetry-based method to extract metrics of tissue anisotropy,” *Opt. Lett.*, vol. 35, no. 15, pp. 2570–2572, 2010.

[87] M. F. Wood, N. Ghosh, M. a Wallenburg, S.-H. Li, R. D. Weisel, B. C. Wilson, R.-K. Li, and I. A. Vitkin, “Polarization birefringence measurements for characterizing the myocardium, including healthy, infarcted, and stem-cell-regenerated tissues.,” *J. Biomed. Opt.*, vol. 15, no. 4, p. 047009, 2010.

[88] Y. Wang, K. Zhang, N. Wasala, X. Yao, D. Duan, and G. Yao, “Histology validation of mapping depth-resolved cardiac fiber orientation in fresh mouse heart using optical polarization tractography,” *Biomed. Opt. Express*, vol. 5, no. 8, pp. 2843–55, Aug. 2014.

[89] S. Alali, Y. Wang, and I. A. Vitkin, “Detecting axial heterogeneity of birefringence in layered turbid media using polarized light imaging,” *Biomed Opt Express.*, vol. 3, no. 12, pp. 3250–3263, 2012.

[90] S. Alali, K. J. Aitken, A. Schröder, A. Shröder, D. J. Bagli, and I. Alex Vitkin, “Optical assessment of tissue anisotropy in ex vivo distended rat bladders,” *J. Biomed. Opt.*, vol. 17, no. 8, p. 086010, Aug. 2012.

[91] M. F. Wood, N. Vurgun, M. A. Wallenburg, and I. A. Vitkin, “Effects of formalin fixation on tissue optical polarization properties,” *Phys Med Biol.*, vol. 56, no. 8, pp. N115–N122, Apr. 2011.

[92] M. A. Wallenburg, M. Pop, M. F. Wood, N. Ghosh, G. A. Wright, and I. A. Vitkin, “Comparison of optical polarimetry and diffusion tensor MR imaging for assessing

myocardial anisotropy," *J. Innov. Opt. Health Sci.*, vol. 03, no. 02, pp. 109–121, Apr. 2010.

[93] R. Ossikovski, "Analysis of depolarizing Mueller matrices through a symmetric decomposition," *J. Opt. Soc. Am. A*, vol. 26, no. 5, 2009.

[94] S. Y. Lu and R. A. Chipman, "Interpretation of Mueller matrices based on polar decomposition," *J. Opt. Soc. Am. A*, vol. 13, no. 5, pp. 1106–1113, May 1996.

[95] N. Ortega-Quijano and J. L. Arce-Diego, "Mueller matrix differential decomposition," *Opt. Lett.*, vol. 36, no. 10, pp. 1942–4, May 2011.

[96] O. Arteaga and A. Canillas, "Pseudopolar decomposition of the Jones and Mueller-Jones exponential polarization matrices," *J. Opt. Soc. Am. A*, vol. 26, no. 4, p. 783, Mar. 2009.

[97] M. Ahmad, S. Ali, M. S. Mehmood, H. Ali, A. Khurshid, S. Firdous, S. Muhammad, and M. Ikram, "Ex vivo assessment of carbon tetrachloride (CCl(4))-induced chronic injury using polarized light spectroscopy," *Appl. Spectrosc.*, vol. 67, no. 12, pp. 1382–9, Dec. 2013.

[98] C. Brosseau, *Fundamentals of polarized light: A statistical optics approach*. John Wiley & sons, Inc, 1998.

[99] F. Gori, M. Santarsiero, S. Vicalvi, R. Borghi, and G. Guattari, "Beam coherence – polarization matrix," vol. 7, pp. 941–951, 1998.

[100] J. J. Gil, "Interpretation of the coherency matrix for three-dimensional polarization states," pp. 1–24.

[101] S. Kumar, H. Purwar, R. Ossikovski, I. A. Vitkin, and N. Ghosh, "Comparative study of differential matrix and extended polar decomposition formalisms for polarimetric characterization of complex tissue-like turbid media," *J Biomed Opt.*, vol. 17, no. 10, p. 105006, Oct. 2012.

[102] D. L. Pham, C. Xu, and J. L. Prince, “Current methods in medical image segmentation,” *Annu. Rev. Biomed. Eng.*, vol. 02, pp. 315–337, 2000.

[103] S. D. Olabarriaga and A. W. M. Smeulders, “Interaction in the segmentation of medical images : A survey,” *Med. Image Anal.*, vol. 5, pp. 127–142, 2001.

[104] A. Ahirwar, “Study of techniques used for medical image segmentation and computation of statistical test for region classification of brain MRI,” *I.J. Inf. Technol. Comput. Sci.*, vol. 05, pp. 44–53, 2013.

[105] H.-S. Wu, J. Barba, and J. Gil, “Iterative thresholding for segmentation of cells from noisy images,” *J. Microsc.*, vol. 197, pp. 296–304, 2000.

[106] C. K. Leung and F. K. Lam, “Maximum a posteriori spatial probability segmentation,” in *IEE Proc.-Vis. Image Signal Process*, 1997, vol. 144, no. 3, pp. 161–167.

[107] M. Sezgin and B. Sankur, “Survey over image thresholding techniques and quantitative performance evaluation,” *J. Electron. Imaging*, vol. 13, no. 1, pp. 146–165, 2004.

[108] S. Aja-fernández, A. H. Curiale, and G. Vegas-sánchez-ferrero, “A local fuzzy thresholding methodology for multiregion image segmentation,” *Knowledge-Based Syst.*, vol. 83, pp. 1–12, 2015.

[109] L. R. Dice, “Measures of the amount of ecologic association between species,” *Ecology*, vol. 26, no. 3, pp. 297–302, 1945.

[110] K. H. Zou, S. K. Warfield, A. Bharatha, C. M. C. Tempany, M. R. Kaus, S. J. Haker, W. M. W. Iii, F. A. Jolesz, and R. Kikinis, “Statistical validation of image segmentation quality based on a spatial overlap index,” *Acad. Radiol.*, vol. 11, no. 02, pp. 178–189, 2004.

[111] K. A. Byrd, J. Zeng, and M. Chouikha, “A validation model for segmentation algorithms of digital mammography images,” *J. Appl. Sci. Eng. Technol.*, vol. 1, pp. 41–50, 2007.

[112] D. Ballabio and V. Consonni, “Classification tools in chemistry. Part 1: linear models. PLS-DA,” *Anal. Methods*, vol. 5, no. 16, p. 3790, 2013.

[113] P. J. Govaerts, T. Somers, and F. E. Offeciers, “Box and whisker plots for graphic presentation of audiometric results of conductive hearing loss treatment,” *Otolaryngol Head Neck Surg.*, vol. 118, no. 6, pp. 892–5, 2000.

[114] C. Zhang, Y. Tang, L. Luo, and W. Xu, “Outlier identification and visualization for Pb concentrations in urban soils and its implications for identification of potential contaminated land,” *Environ. Pollut.*, vol. 157, no. 11, pp. 3083–90, Nov. 2009.

[115] V. P. Chinem and H. A. Miot, “Epidemiology of basal cell carcinoma,” *An. Bras. Dermatol.*, vol. 86, no. 2, pp. 292–305, 2011.

[116] J. P. Lacour, “Carcinogenesis of basal cell carcinomas: genetics and molecular mechanisms.,” *Br. J. Dermatol.*, vol. 146 Suppl, no. 61, pp. 17–9, Apr. 2002.

[117] M. Takata and T. Saida, “Early cancers of the skin: clinical, histopathological, and molecular characteristics,” *Int. J. Clin. Oncol.*, vol. 10, no. 6, pp. 391–7, Dec. 2005.

[118] A. Garcia-Uribe, J. Zou, M. Duvic, J. H. Cho-Vega, V. G. Prieto, and L. V Wang, “In vivo diagnosis of melanoma and nonmelanoma skin cancer using oblique incidence diffuse reflectance spectrometry,” *Cancer Res.*, vol. 72, no. 11, pp. 2738–45, Jun. 2012.

[119] E. Salomatina, B. Jiang, J. Novak, and A. N. Yaroslavsky, “Optical properties of normal and cancerous human skin in the visible and near-infrared spectral range,” *J. Biomed. Opt.*, vol. 11, no. December, pp. 1–9, 2006.

[120] A. N. Bashkatov, E. A. Genina, and V. V Tuchin, “Optical properties of skin, subcutaneous, and muscle tissues : a review,” *J. Innov. Opt. Health Sci.*, vol. 4, no. 1, pp. 9–38, 2011.

[121] H. Search, C. Journals, A. Contact, M. Iopscience, and I. P. Address, “Optical properties of human skin , subcutaneous and mucous tissues in the wavelength range from 400 to 2000 nm,” *J. Phys. D. Appl. Phys.*, vol. 2543, 2005.

[122] L. M. Mcintosh, M. Jackson, H. H. Mantsch, M. F. Stranc, D. Pilavdzic, and A. N. Crowson, “Infrared spectra of basal cell carcinomas are distinct from non-tumor-bearing skin components,” pp. 951–956, 1999.

[123] R. S. Gurjar, V. Backman, L. T. Perelman, I. Georgakoudi, K. Badizadegan, I. Itzkan, R. R. Dasari, and M. S. Feld, “Imaging human epithelial properties with polarized light-scattering spectroscopy,” *Nat. Med.*, vol. 7, no. 11, pp. 1245–8, Nov. 2001.

[124] D. Arifler, I. Pavlova, A. Gillenwater, and R. Richards-Kortum, “Light scattering from collagen fiber networks: micro-optical properties of normal and neoplastic stroma,” *Biophys. J.*, vol. 92, no. 9, pp. 3260–74, May 2007.

[125] R. Cicchi, N. Vogler, D. Kapsokalyvas, B. Dietzek, J. Popp, and F. S. Pavone, “From molecular structure to tissue architecture: collagen organization probed by SHG microscopy,” *J. Biophotonics*, vol. 6, no. 2, pp. 129–42, Feb. 2013.

[126] K. Sokolov, R. Drezek, K. Gossage, and R. Richards-Kortum, “Reflectance spectroscopy with polarized light: is it sensitive to cellular and nuclear morphology,” *Opt. Express*, vol. 5, no. 13, p. 302, Dec. 1999.

[127] C.-C. Yu, C. Lau, J. W. Tunnell, M. Hunter, M. Kalashnikov, C. Fang-Yen, S. F. Fulghum, K. Badizadegan, R. R. Dasari, and M. S. Feld, “Assessing epithelial cell nuclear morphology by using azimuthal light scattering spectroscopy,” *Opt. Lett.*, vol. 31, no. 21, p. 3119, 2006.

[128] I. S. Saidi, S. L. Jacques, and F. K. Tittel, “Mie and Rayleigh modeling of visible-light scattering in neonatal skin,” *Appl. Opt.*, vol. 34, no. 31, pp. 7410–8, Nov. 1995.

[129] D. J. Maitland and J. J. Walsh, “Quantitative measurements of linear birefringence during heating of native collagen,” *Lasers Surg. Med.*, vol. 20, no. 3, pp. 310–318, 1997.

[130] V. Sankaran and J. T. Walsh, “Birefringence measurement of rapid structural changes during collagen denaturation,” *Photochem. Photobiol.*, vol. 68, no. 6, pp. 846–851, 1998.

[131] O. Lupi, I. Semenovitch, C. Treu, and E. Bouskela, “Orthogonal polarization technique in the assessment of human skin microcirculation,” *Int. J. Dermatol.*, vol. 47, pp. 425–431, 2008.

[132] D. Haemmerich, J. G. Webster, and D. M. Mahvi, “Thermal dose versus isotherm as lesion boundary estimator for cardiac and hepatic radiofrequency ablation,” in *The 25’t Annual International Conference of the IEEE EMBS*, 2003, pp. 134–137.

[133] D. Keane, J. Ruskin, N. Norris, P.-A. Chapelon, and D. B´erub´e, “In vitro and in vivo evaluation of the thermal patterns and lesions of catheter ablation with a microwave monopole antenna,” *J. Interv. Card. Electrophysiol.*, vol. 10, pp. 111–119, 2004.

[134] M. W. Dewhirst, B. L. Viglianti, M. Hanson, and P. J. Hoopes, “Basic principles of thermal dosimetry and thermal thresholds for tissue damage from hyperthermia,” *Int. J. Hyperth.*, vol. 19, no. 3, pp. 267–294, 2003.

[135] C. Fan and G. Yao, “Imaging myocardial fiber orientation using polarization sensitive optical coherence tomography,” *Biomed Opt Express.*, vol. 4, no. 3, pp. 460–465, 2013.

[136] M. Oeff, J. J. Langberg, J. O. Franklin, M. C. Chin, H. Sharkey, W. Finkbeiner, J. M. Herre, and M. M. Scheinman, "Effects of multipolar electrode radiofrequency energy delivery on ventricular endocardium," *Am Hear. J*, vol. 119, no. 3, pp. 599–607, 1990.

[137] J. Swartling, S. Pålsson, P. Platonov, S. B. Olsson, and A. E. Andersson, "Changes in tissue optical properties due to radiofrequency ablation of myocardium," *Med Biol Eng Comput*, vol. 41, no. 4, pp. 403–409, 2003.

[138] T. Vo-Dinh, "Biomedical Photonics Handbook," in *CRC Press, Boca Raton, FL, USA*, 2003, p. Ch 12.

[139] J. Seiler, K. C. Roberts-Thomson, J.-M. Raymond, J. Vest, E. Delacretaz, and W. G. Stevenson, "Steam pops during irrigated radiofrequency ablation: feasibility of impedance monitoring for prevention," *Hear. Rhythm.*, vol. 5, no. 10, pp. 1411–1416, Oct. 2008.

[140] S. Manhas, J. Vizet, S. Deby, J.-C. Vanel, P. Boito, M. Verdier, A. De Martino, and D. Pagnoux, "Demonstration of full 4×4 Mueller polarimetry through an optical fiber for endoscopic applications," *Opt Express*, vol. 23, no. 3, p. 3047, 2015.

[141] G. Lee, P. Sanders, and J. M. Kalman, "Catheter ablation of atrial arrhythmias: state of the art," *Lancet*, vol. 380, pp. 1509–1519, Oct. 2012.

[142] W. G. Stevenson and E. Delacretaz, "Radiofrequency catheter ablation of ventricular tachycardia," *Heart*, vol. 84, no. 5, pp. 553–559, 2000.

[143] G. P. Mazzara, R. P. Velthuizen, L. J. Pearlman, H. M. Greenberg, and H. Wagner, "Brain tumor target volume determination for radiation treatment planning through automated MRI segmentation," *Int. J. Radiat. Oncol. Biol. Phys.*, vol. 59, no. 1, pp. 300–312, 2004.

[144] G. A. Pang, E. Bay, X. L. Deán-Ben, and D. Razansky, “Three-dimensional optoacoustic monitoring of lesion formation in real time during radiofrequency catheter ablation,” *J. Cardiovasc. Electrophysiol.*, vol. 26, no. 3, pp. 339–345, 2015.

[145] S. A. Eyerly, S. J. Hsu, S. H. Agashe, G. E. Trahey, Y. Li, and P. D. Wolf, “An in vitro assessment of acoustic radiation force impulse imaging for visualizing cardiac radiofrequency ablation lesions,” *J. Cardiovasc. Electrophysiol.*, vol. 21, no. 5, pp. 557–563, 2010.

[146] A. Norouzi, M. S. M. Rahim, A. Altameem, T. Saba, A. E. Rad, A. Rehman, and M. Uddin, “Medical image segmentation methods, algorithms, and applications,” *IETE Tech. Rev.*, vol. 31, no. 3, pp. 199–213, 2014.

[147] A. Popovic, M. de la Fuente, M. Engelhardt, and K. Radermacher, “Statistical validation metric for accuracy assessment in medical image segmentation,” *Int. J. Comput. Assist. Radiol. Surg.*, vol. 2, no. 3–4, pp. 169–181, 2007.

[148] X. Guo, M. F. G. Wood, and A. Vitkin, “A Monte Carlo study of penetration depth and sampling volume of polarized light in turbid media,” *Opt. Commun.*, vol. 281, no. 3, pp. 380–387, 2008.

[149] S. Demos, H. Radousky, and R. Alfano, “Deep subsurface imaging in tissues using spectral and polarization filtering,” *Opt. Express*, vol. 7, no. 1, pp. 23–28, 2000.

[150] D. Herranz, J. Lloret, S. Jim, and E. Margallo-balb, “Novel catheter enabling simultaneous radiofrequency ablation and optical coherence reflectometry,” *Biomed Opt Express.*, vol. 6, no. 9, pp. 257–259, 2015.

[151] I. Ahmad, M. Ahmad, K. Khan, and M. Ikram, “Polarimetry based partial least square classification of ex vivo healthy and basal cell carcinoma human skin tissues,” *Photodiagnosis Photodyn. Ther.*, vol. 14, pp. 134–141, 2016.

[152] R. Ossikovski, M. Anastasiadou, S. Ben Hatit, E. Garcia-Caurel, and A. De Martino, “Depolarizing Mueller matrices: how to decompose them ?,” *Phys. Status Solidi*, vol. 205, no. 4, pp. 720–727, 2008.

[153] S. Alali, T. Yang, and I. A. Vitkin, “Rapid time-gated polarimetric Stokes imaging using photoelastic modulators,” *Opt. Lett.*, vol. 38, no. 16, pp. 2997–3000, 2013.

[154] P. A. Letnes, I. S. Nerbø, L. Martin, S. Aas, G. Ellingsen, and M. Kildemo, “Fast and optimal broad-band Stokes / Mueller polarimeter design by the use of a genetic algorithm,” *Opt. Express*, vol. 18, no. 22, pp. 23095–23103, 2010.

[155] M. W. Kudenov, M. J. Escuti, N. Hagen, E. L. Dereniak, and K. Oka, “Snapshot imaging Mueller matrix polarimeter using polarization gratings,” *Opt. Lett.*, vol. 37, no. 8, pp. 1367–1369, 2012.

[156] J. Chang, N. Zeng, H. He, Y. He, and H. Ma, “Single-shot spatially modulated Stokes polarimeter based on a GRIN lens,” *Opt. Lett.*, vol. 39, no. 9, pp. 2656–2659, 2014.

[157] V. M. Turzhitsky, A. J. Gomes, Y. L. Kim, Y. Liu, A. Kromine, J. D. Rogers, M. Jameel, H. K. Roy, and V. Backman, “Measuring mucosal blood supply in vivo with a polarization-gating probe,” *Appl. Opt.*, vol. 47, no. 32, pp. 6046–6057, 2008.

[158] J. Vizet, S. Manhas, S. Deby, J. Vanel, A. De Martino, and D. Pagnoux, “Demonstration of Mueller polarimetry through an optical fiber for endoscopic applications,” in *CLEO: QELS_ Fundamental Science Poster Session 2*, 2014, pp. 2–3.

[159] G. Thomas, J. Van Voskuilen, H. C. Gerritsen, and H. J. C. M. Sterenborg, “Advances and challenges in label-free nonlinear optical imaging using two-photon excitation fluorescence and second harmonic generation for cancer research,” *J. Photochem. Photobiol. B Biol.*, vol. 141, pp. 128–138, 2014.